Summer 2007

Mobile array designs with ANSERLIN antennas and efficient, wide-band PEEC models for interconnect and power distribution network analysis

Michael A. Cracraft

Department: Electrical and Computer Engineering

MOBILE ARRAY DESIGNS WITH ANSERLIN ANTENNAS AND EFFICIENT, WIDE-BAND PEEC MODELS FOR INTERCONNECT AND POWER DISTRIBUTION NETWORK ANALYSIS

by

MICHAEL ANDREW CRACRAFT

A DISSERTATION

Presented to the Faculty of the Graduate School of the

UNIVERSITY OF MISSOURI–ROLLA

in Partial Fulfillment of the Requirements for the Degree

DOCTOR OF PHILOSOPHY

in

ELECTRICAL ENGINEERING

2007

Dr. James L. Drewniak, Advisor	Dr. David J. Pommerenke
Dr. Richard DuBroff	Dr. Mariesa Crow

Dr. Matt O'Keefe

ABSTRACT

A mobile, wide-band antenna system has been developed around the ANSER-LIN antenna element and a 3-dB splitter design. The size of the antenna elements was reduced over previous versions by introducing dielectric substrates. Additionally, new variations of the antenna were designed to influence radiation characteristics. To further reduce the number of components in the array, a very low profile splitter was designed and mounted below one of the antenna elements, doubling as the return plane for the antenna.

The partial-element equivalent circuit (PEEC) method has been used for 3D interconnect analysis and numerous other applications. Being based on the same ideas as the method of moments, the PEEC method generates dense matrices for its cell interactions. This thesis contains research focused on efficiently using a limited number of cells for accurate results. This has been approached with a hybrid method and also with grid refinements. Additionally, the accuracy of PEEC coupling over electrically long distances has been addressed using wide-band accurate partial parameter calculations.

ACKNOWLEDGMENT

Over the course of my Ph.D. work, I have received help and support from many people. Seldom are problems simple in the pursuit a Ph.D. If the problem is simple, then someone has already solved it. So, I must thank my advisor Jim Drewniak for helping me break down problems to their basic physics. Also, I would like to thank the rest of my committee for their advice on this dissertation. I want to thank my friends and fellow graduate students for assistance when research problems converged. Namely, I want to thank Giuseppe Selli, Mauro Lai, Xiaohe Chen, and Feng Gang. I owe Sarah and John Seguin a special thanks for listening to my rants about my research in order to clear my head. Only my wife, Amy, has endured more unintelligible rambling as I work out ideas in half speech. So, I must doubly thank her for supporting me during my time as a graduate student.

TABLE OF CONTENTS

LIST OF ILLUSTRATIONS

LIST OF TABLES

1. SIZE REDUCTION WITH DIELECTRIC SUBSTRATES AND BEAM STABILIZING FOR ANSERLIN ANTENNA GEOMETRIES

The ANSERLIN class of antennas are meant to provide wide-band, circularly polarized (CP) radiation. The original ANSERLIN antennas were built in air with low permittivity spacers supporting the radiating line [5]. These antennas achieved better than -10 dB return losses over 8:1 bands in some cases and radiation efficiencies of 60% at the $m' = 1$ frequency.

The two-port, traveling-wave characteristics of the ANSERLIN antenna allow it to be used in a series-fed array [6]. Rotating one antenna in the array relative to the others is equivalent to a phase shift but without the need for delay lines. More recently, a four-element series fed array was used in conjunction with conducting loading rings in order to suppress the sidelobes of the array [23].

At the $m' = 1$ frequency the farfield radiation of ANSERLIN antennas is a maximum at broadside. As the operating frequency increases beyond the $m' = 1$ frequency, more radiating modes contribute to the overall pattern. As a result the primary radiating lobe tilts off-axis as frequency increases and eventually separates into two lobes of approximately equal magnitude. Steering the main lobe of a four element array of ANSERLIN was shown to be possible by exciting both ports of the antenna with inputs of a certain phase difference.

For some of the antennas described in this report, dielectrics of $\varepsilon_r > 1$ have been used to reduce the size of the antenna. Using a higher permittivity decreases the antenna radius required for the same electric length. Dielectrics with $\varepsilon_r = 9.7$ have been used to reduce the 50-Ω width-to-height ratio from approximately 3:1 to 1:1. Although the dielectrics decrease the antenna size, this size reduction results in some loss of radiation efficiency in the lower end of the radiation band.

The frequency range of the ANSERLIN antenna is limited below the $m' = 1$ frequency as it is an inefficient radiator. The upper frequency range may be determined by the return loss as the mismatch of the annular sector, the transitioning fin, or the feed geometry becomes significant. Alternatively, if the beam shape is critical, the upper frequency is determined by nulls at broadside as higher order modes are excited. Beam steering was previously shown by feeding the two ports with phased inputs [22]. This report will demonstrate that the radiation pattern can also be preserved at higher frequencies using different ground shapes.

1.1. SYNTHESIS OF ANSERLIN ELEMENTS WITH DIELECTRIC SUBSTRATES

The ANSERLIN antennas are radiating-line antennas, which radiate effieciently when the circumference of the antenna is one wavelength or higher. As with other antenna designs, as the desired operating frequency decreases, the size of the antenna increases. Due to the requirement of maintaining width-to-height ratios, the antenna size will also increase as the height of radiating element is increased. The size of the antennas for a particular operating frequency can be decreased substantially by using dielectrics with $\varepsilon_r > 1$. The dimensions for several antennas are shown in Table 1.1, and a rendering of Antenna #1 is shown in Figure 1.1. Antenna #1 is a round version of the ANSERLIN design. Two other variations of the ANSERLIN design are also described in this report. The cupped-ground described as cupped-ground antennas are described in Section 1.3, and the flat-feed variation is described in Section 1.4.

Table 1.1 Antenna construction parameters

#	$f(m'=1)$ (GHz)	h (cm)	a (cm)	b (cm)	Fin w/h	Annular Sector w/h	Description
1	1.8	1	0.68	1.4	0.975	0.72	Round (ε_r = 9.7, 2.7-in ground diameter)
2	1.8	1	0.68	1.4	0.975	0.72	Round (ε_r = 9.7, 2.7-in ground diameter, larger port separation)
3	1.8	1	0.7	1.4	$\tilde{1}.6$	0.7	Round (ε_r = 9.7, 2.7-in ground diameter)
4	1.8	1	0.7	1.4	$\tilde{1}.6$	0.7	Round (ε_r = 9.7, 2.1-in ground diameter)
5	1.65	1.5	0.3	1.4	0.98	0.73	Cupped-Ground ($\varepsilon_r = 9.7$)
6	1.3	1.5	1	1.8	1.33	0.53	Cupped-Ground ($\varepsilon_r = 9.7$)
7	1.65	1.45	1	4.5	N/A	2.4	Flat-Feed (FR4 and Foam)

The antenna behavior is dependent on the design feed port, the fin shape, the transition from the fin to the annular sector, and the annular sector itself. The diameter of the ground plane relative to the outer diameter of the annular sector is also important. The basic structure of these antennas can be determined using a few simple equations for microstrip transmission lines and effective permittivity calculations. However, if more precise tuning is required, time-domain reflectometry (TDR)

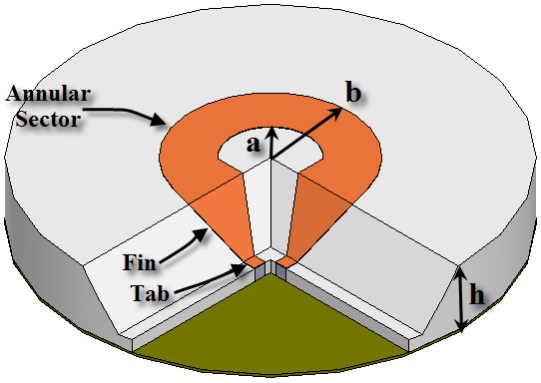

Figure 1.1 Perspective view of a round ANSERLIN (Antenna #1)

measurements can be used while adjusting the antenna element. TDR measurements of the antennas in this report is covered in Section 1.2.1.

1.1.1. Feed Ports and Fins. The dielectric version of the ANERLIN antenna can be fed by coaxial cables connected through the return plane. However, an alternative feed configuration is presented in Section 1.4. The center conductor connects to a flat tab through a thin section of the dielectric. The width of these tabs is commonly made the same as a 50-Ω microstrip, assuming that the antenna is made for a 50-Ω system. The length of the tab can be adjusted to balance the inductance of the feed conductor.

The feed tab connects to the fin structure. To minimize reflections along the line, the fin maintains the same width-to-height ratio as that of the tab. Microstrip equations for the characteristic impedance like those [21] are adequate for determining the width-to-height ratio of the fin.

1.1.2. Annular Sector. The annular sector is joined to the top of the fin by a transition section constructed of straight segments. This length of the transition section is dependent on a, the inner radius of the annular sector, the width-to-height ratio of the fin, and the fin position. Although the fin sections can be designed from microstrip equations for characteristic impedance, the annular sector due to its curvature does not conform to these equations. The characteristic impedance for a curved microstrip was discussed in [34] with more detail found in [9] and also in [29].

The extent to which these calculations may be useful depends on the transition section and the length of the annular sector. The annular sector in Antennas #3 and #4 from Table 1.1 comprises only a little more than 90° of the radiating line. The radiating lines of these two antennas were designed using parametric sweeps in a

frequency-domain solver with Antenna #2 as a reference. The long transition section and shorted annular sector leave little distance for higher-order fields to attenuate. Reasons for the distorted shape of these two radiating lines are explained by TDR measurements in Section 1.2.1.

1.1.3. Determining the Radiation Band. The first radiating mode of the ANSERLIN design occurs when the phase progresses at one degree per one degree of the arc length. The modes of the antenna are dependent on the mean radius of the annular sector and the effective permittivity seen by the radiating line. A fair approximation of the effective permittivity may be obtained using microstrip expressions like the following:

$$E_a = \begin{cases} \frac{\varepsilon_r+1}{2} + \frac{\varepsilon_r-1}{2}\left[\frac{1}{\sqrt{1+\frac{12h}{W}}} + 0.04\left(1-\frac{W}{h}\right)^2\right] & , \quad W/h < 1 \\ \frac{\varepsilon_r+1}{2} + \frac{\varepsilon_r-1}{2\sqrt{1+\frac{12h}{W}}} & , \quad W/h \geq 1 \end{cases} \tag{1.1a}$$

$$\varepsilon_{reff} = \left[E_a - \frac{(\varepsilon_r - 1)\left(\frac{t}{h}\right)}{4.6\sqrt{\frac{W}{h}}}\right] . \tag{1.1b}$$

However, it is important to mention that this expression pertains to a straight microstrip line. The accuracy will be much less for antennas with long transitions from fin to annular sector and antennas with small radius of curvatures, for example.

The estimate for m' is calculated as

$$m'(< r >, \varepsilon_{reff}, f) = \frac{2\pi f < r > \sqrt{\varepsilon_{reff}}}{c_0} \tag{1.2}$$

or the mean radius for a particular frequency can be calculated by

$$< r >= \frac{c_0}{2\pi f \sqrt{\varepsilon_{reff}}} \tag{1.3}$$

assuming $m' = 1$. The inner and outer radii, a and b, respectively, can be calculating from $< r >$ and the width-to-height ratio for the annular sector. The result can be verified with field measurements referenced to the phase at the input port. For $m' = 1$, there should be one degree of phase shift per degree rotation about the antenna.

1.2. TDR ANALYSIS AND TUNING

Time-domain reflectometry (TDR) is extremely useful in ensuring minimal reflections on current paths through the antenna. Frequency-domain S-parameter measurements are also useful but do not normally yield information about the location of the feature responsible for the measurement. TDR measurements using pulses with fast rise times can fairly accurately point out discontinuities and the degree to which they may affect the overall behavior of the antenna. Section 1.2.1 discusses the TDR measurements on the antennas of Table 1.1 and common behaviors of the ANSERLIN class of antennas. Section 1.2.2 looks specifically at Antennas #5 and #6, and the changes to the radiating line structure that led from #5 to #6.

1.2.1. TDR Analysis of the ANSERLIN Structures. ANSERLIN antennas are generally fed by coax to microstrip transitions. The microstrips in turn transition to the wider, elevated radiating-line element. These common features translate to the TDR measurements also. Figure 1.2 shows TDR measurements for the seven antennas.

The common TDR response among the ANSERLIN antennas in this report is an area of high impedance located around the top of the fins and a very low impedance over the annular sector. The better matched responses in Figure 1.2 compensate for the high and low impedance regions by slightly wider areas at the top of the fin and very narrow annular sectors. Care must be taken with these adjustments, as they may improve the match of the antenna, they may also adversely affect either the radiated power, the radiation pattern, or both.

1.2.2. Reducing Reflections using TDR Measurements. Because the ANSERLIN antennas radiate by traveling waves, any reflected waves are detrimental to the radiation efficiency. The guidelines for synthesizing ANSERLIN structures on dielectrics given in Section 1.1 can be improved on using TDR measurements as a guide. Antennas #5 and #6 from Table 1.1 have the same return plane, dielectric shape, and feed locations. However, the annular sector of Antenna #6 has been reshaped to reduce reflections.

As a rule material in the path is removed to increase the inductance per unit length, and thus, increase the characteristic impedance. Then, adding material increases the capacitance per unit length, lowering the characteristic impedance. Figure 1.3 shows the outlines of the radiating line shapes in the steps that it was tuned. Figure 1.4 shows the TDR measurements at each step.

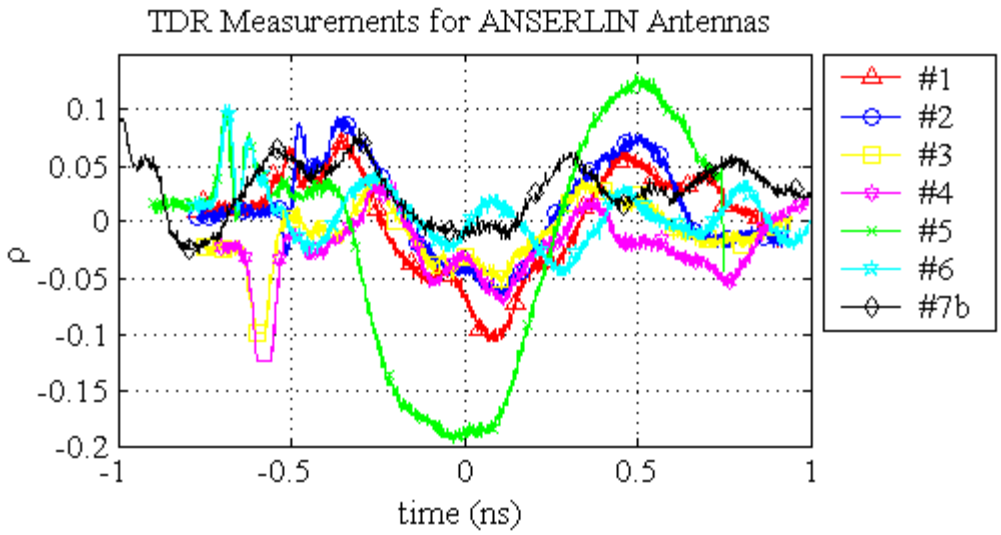

Figure 1.2 Collected TDR measurement plots for all seven antennas

The first step shown in Figure 1.3(b) is the increase in the outer radius of the annular sector. This change causes more reflections than the original because of the added capacitance to an already low characteristic impedance. The reason for the change was to set the antenna up for the further alterations. Next, the inner radius was increased while maintaining the fin positions. This increased the characteristic impedance of the annular sector close to 50-Ω. After these changes, the impedance of the transition section between the annular sector and the fin was too low. In addition, the impedance at the top of the fin was slightly high. Circular cuts were made at the inner edge of the transition section. This has the added bonus of increasing the length of the annular sector. The fin width was also increased slightly to reduce the impedance there.

1.3. CUPPED GROUND STRUCTURE

The radiation pattern of the ANSERLIN antenna has nulls at broadside for all modes besides the $m' = 1$ mode. This change in the radiation pattern as frequency increases can limit its usefulness when that radiation pattern is critical, i.e., when a directional antenna is required. It has been found that modifying the geometry of the ground surface can reduce the effect of the higher order modes on the radiation patter, or in some cases it may accentuate the higher order modes. Radiation patterns are

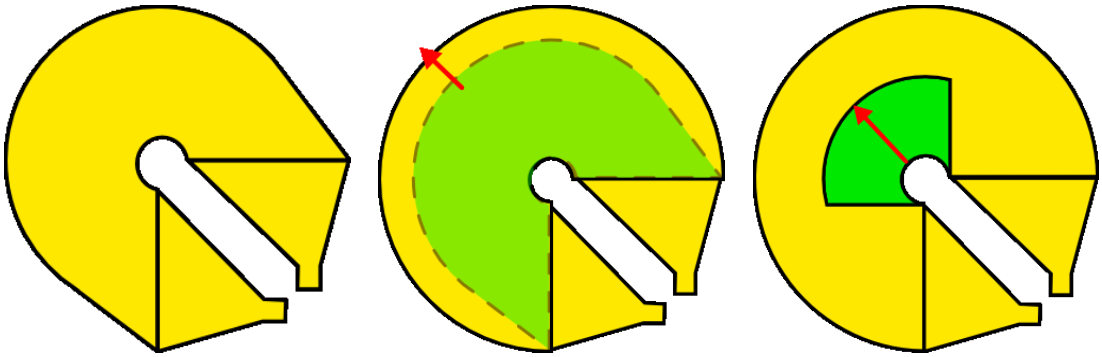

(a) The original version identical to Antenna #5

(b) The outer radius inceased to the outer edge of the fins

(c) The inner radius increased progressively to get a good match with the characteristic impedance of the annular sector

Figure 1.3 Outlines of the tuning steps to Antenna #6

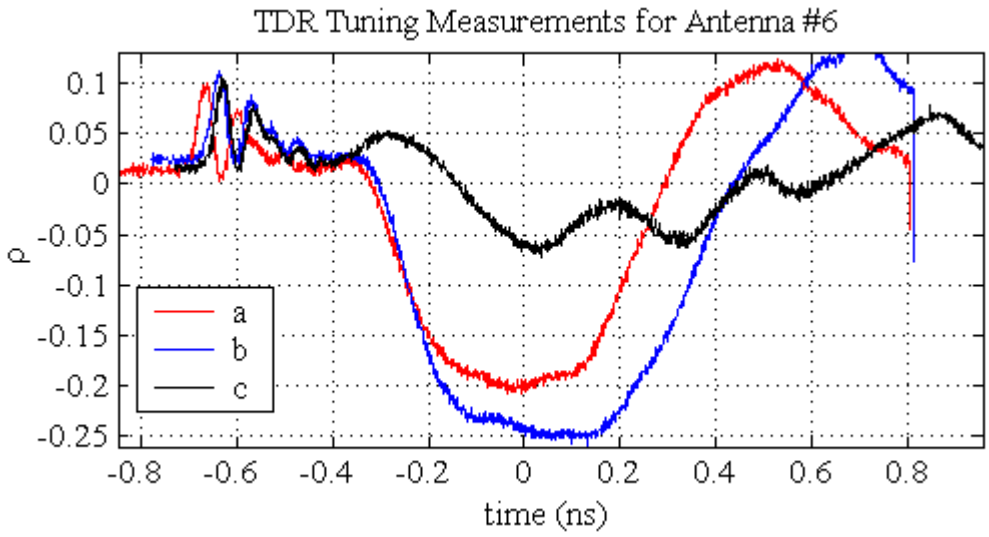

Figure 1.4 TDR measurements from tuning Antenna #6 matching the illustrations in Figure 1.3

compared from cupped-ground and round dielectric antennas. Additionally, radiation from ANSERLIN with very large ground planes is shown.

The cupped-ground antenna design uses a cup shaped return plane, which when applied properly maintains the broadside beam direction better than larger flat planes.

The radiating line geometry is the same as in previous round antennas, although the cupped-ground version may require significantly more tuning to account for the added capacitance from the elevated edges of the return plane. The slope of the return plane is defined by the angle θ_{cup} defined as

$$\tan\left(\theta_{\text{cup}}\right) = \frac{h}{\text{GND}_{rad,h} - \text{GND}_{rad}} \tag{1.4}$$

and shown in Figure 1.5. The slope of the return plane is approximately 45° for Antennas #5 and #6. This angle is not required, but seems a good compromise between vertical side walls and the regular round ANSERLIN designs.

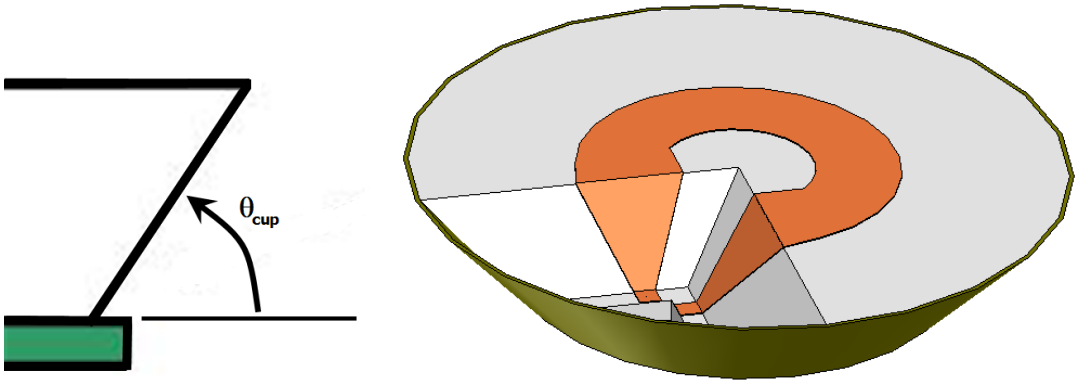

(a) Side view (b) Perspective view of a cupped-ground antenna

Figure 1.5 The cupped return plane makes the angle θ_{cup} with the flat return plane

Realized gain measurements on Antennas #1 and #5 were conducted. The far fields are considered in two vertical planes; the orientations for these planes are shown in Figure 1.6. The ANSERLIN antennas are symmetric about a line drawn between the feed points through the middle of the antenna. The first plane is drawn orthogonal to this symmetry line; it cuts across the annular sector and is labeled as the cross cut. Figure 1.6(a) shows the positive orientation of θ, the elevation, with respect to the annular sector for the cross cut; $\theta = 0$ denotes the broadside radiation direction. The second plane is parallel with the symmetry line, cutting through the notch between the feed points. Figure 1.6(b) shows orientation of θ for this plane.

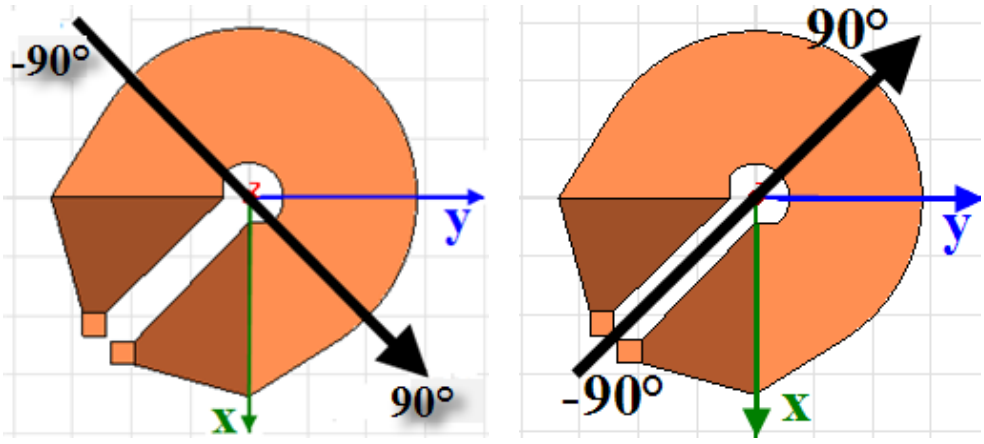

(a) Cross cut orientation (b) Notch cut orientation

Figure 1.6 Orientations of the vertical planes for gain measurements

The realized gain is defined as

$$\text{Realized Gain} = \frac{4\pi U(\theta,\phi)}{P_{\text{inc}}}\ , \tag{1.5}$$

where $U(\theta,\phi)$ is the radiation intensity with units of watts per unit area, and P_{inc} is the incident power at the input port. The radiation intensity is defined as in [3],

$$U(\theta,\phi) = \frac{r^2|\vec{E}(r,\theta,\phi)|^2}{2\eta} \approx \frac{|E_f(\vec{\theta},\phi)|^2}{2\eta}\ , \tag{1.6}$$

where $\vec{E_f}$ is the electric far-field, and η is the intrinsic impedance of the medium. Gain differs from realized gain in that the expression contains the accepted power instead of the incident power. Thus, the gain is higher than the realized gain. When $S_{11} \approx 0$, gain and realized gain are nearly identical.

Figures 1.7 through 1.12 show the realized gain measured and simulated from Antenna #5, the cupped-ground antenna, with Antenna #1 as the round comparison. For the frequencies below 2 GHz, the cupped-ground antenna has higher realized gain than the round antenna despite the smaller mean radius, and thus, higher $m' = 1$ frequency, of the cupped-ground antenna. Above 2 GHz, the round antenna has better realized gain.

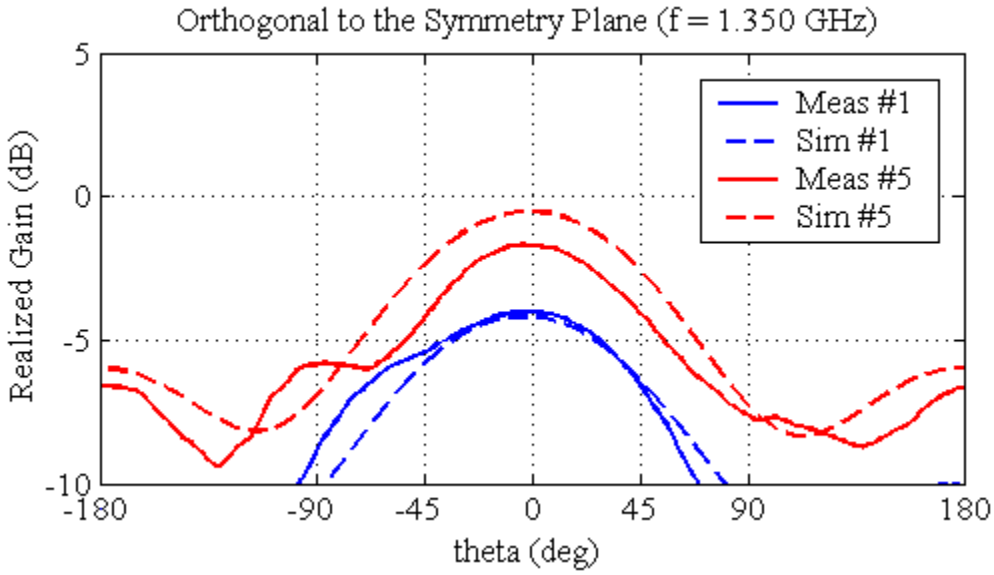

(a) Cross cut

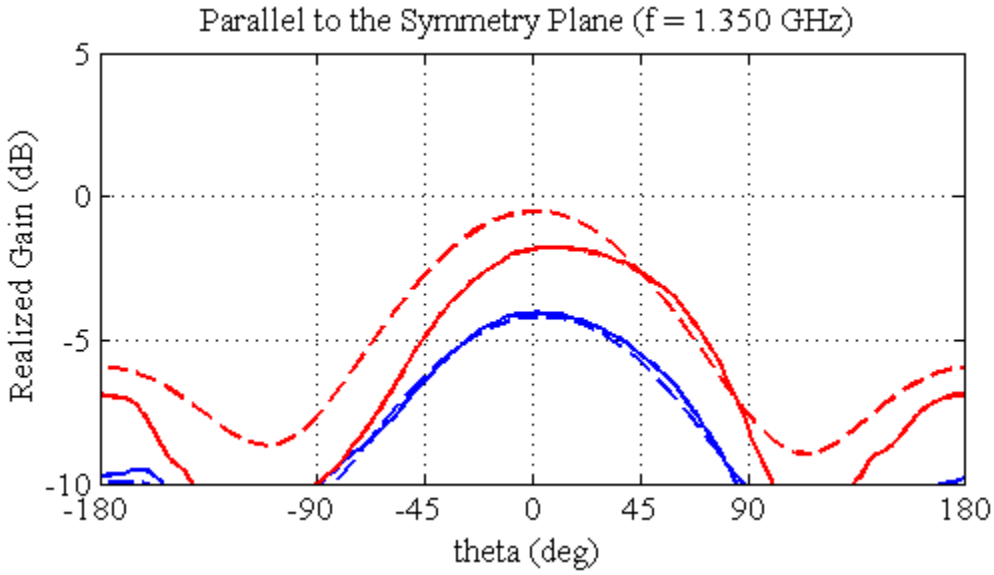

(b) Notch cut

Figure 1.7 Realized gain of Antennas #1 and #5 measured and simulated at 1.35 GHz

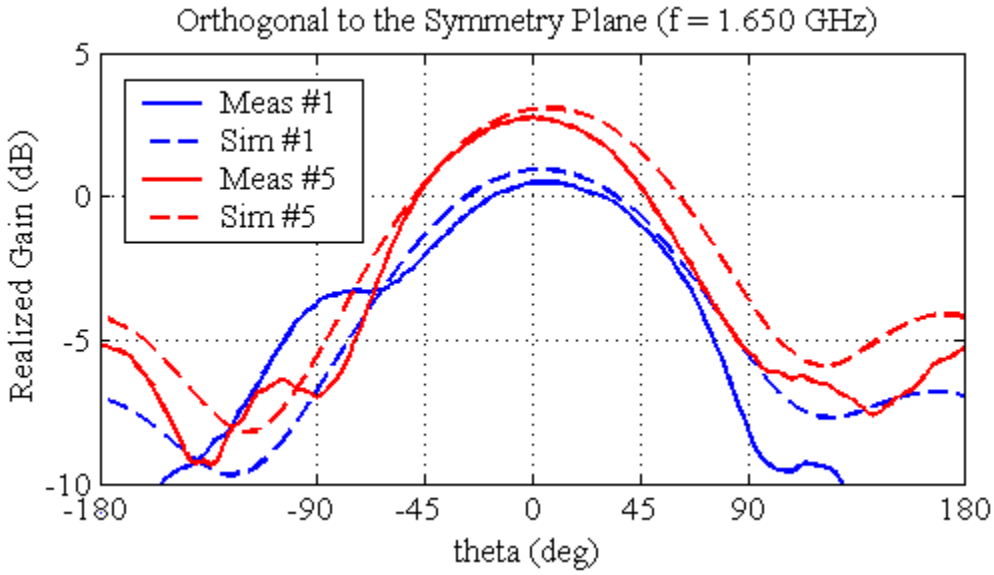

(a) Cross cut

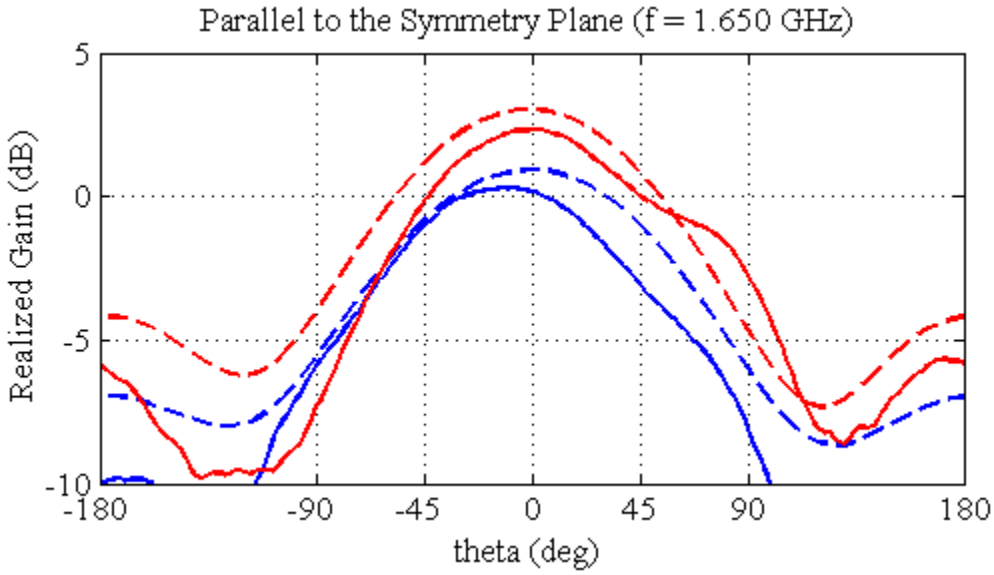

(b) Notch cut

Figure 1.8 Realized gain of Antennas #1 and #5 measured and simulated at 1.65 GHz

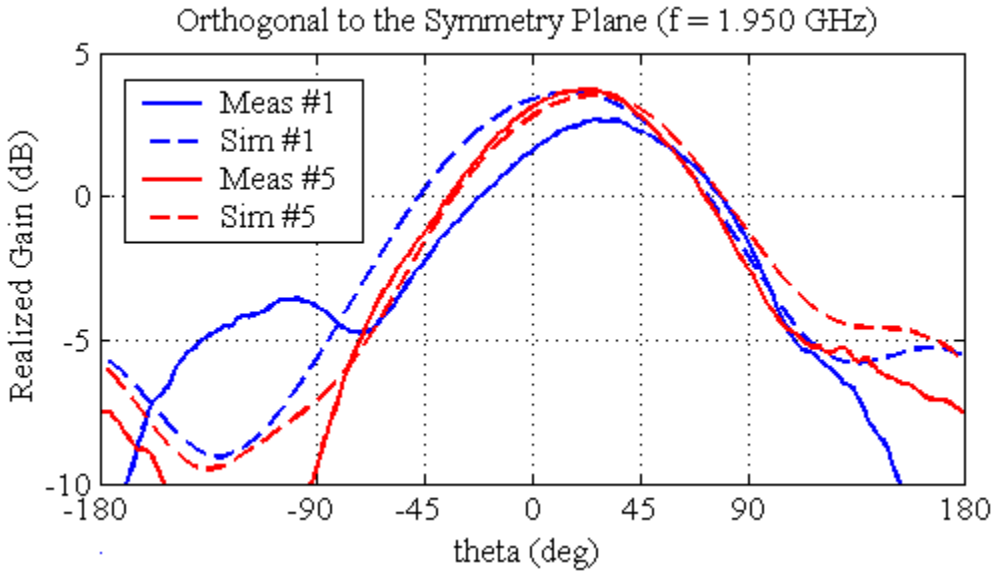

(a) Cross cut

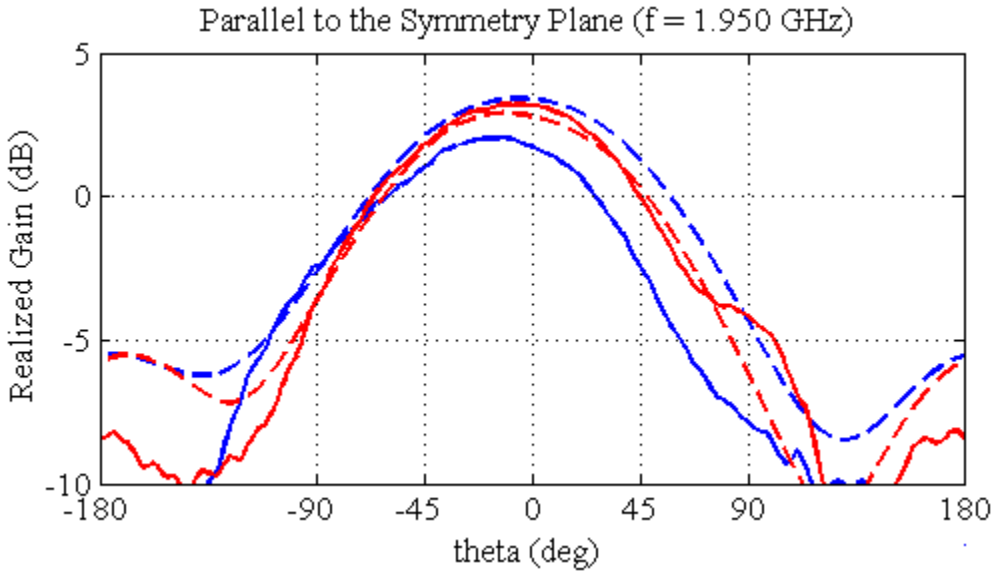

(b) Notch cut

Figure 1.9 Realized gain of Antennas #1 and #5 measured and simulated at 1.95 GHz

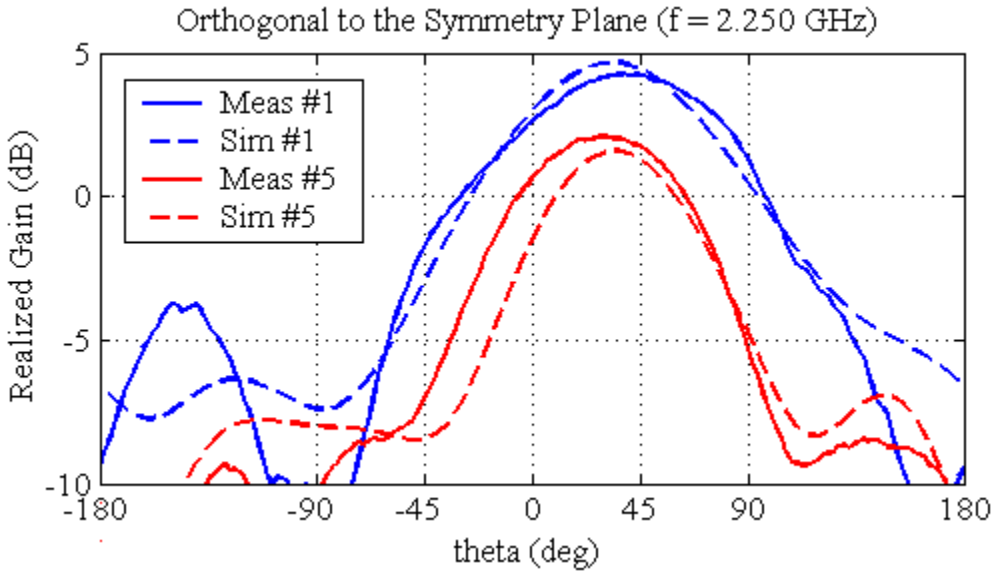

(a) Cross cut

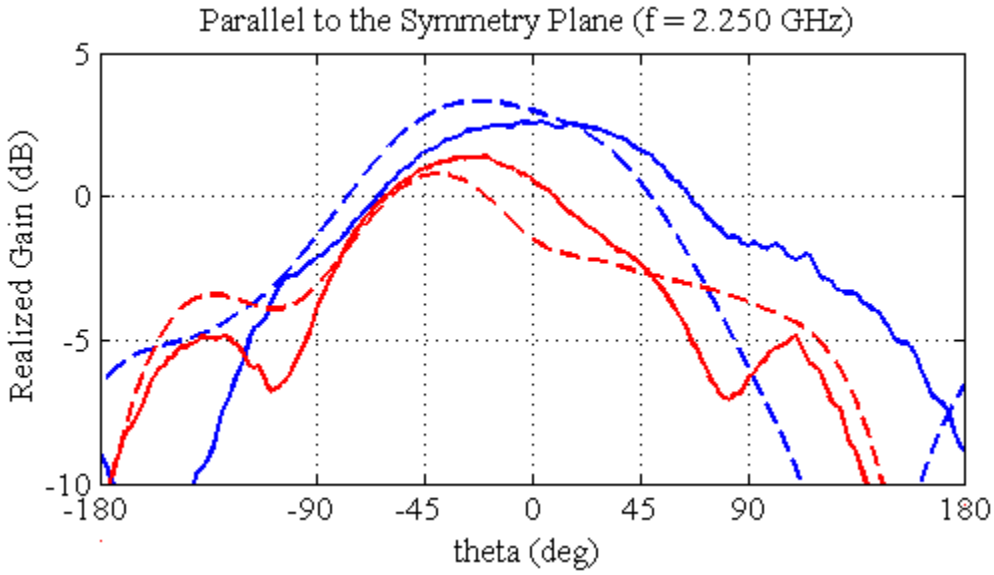

(b) Notch cut

Figure 1.10 Realized gain of Antennas #1 and #5 measured and simulated at 2.25 GHz

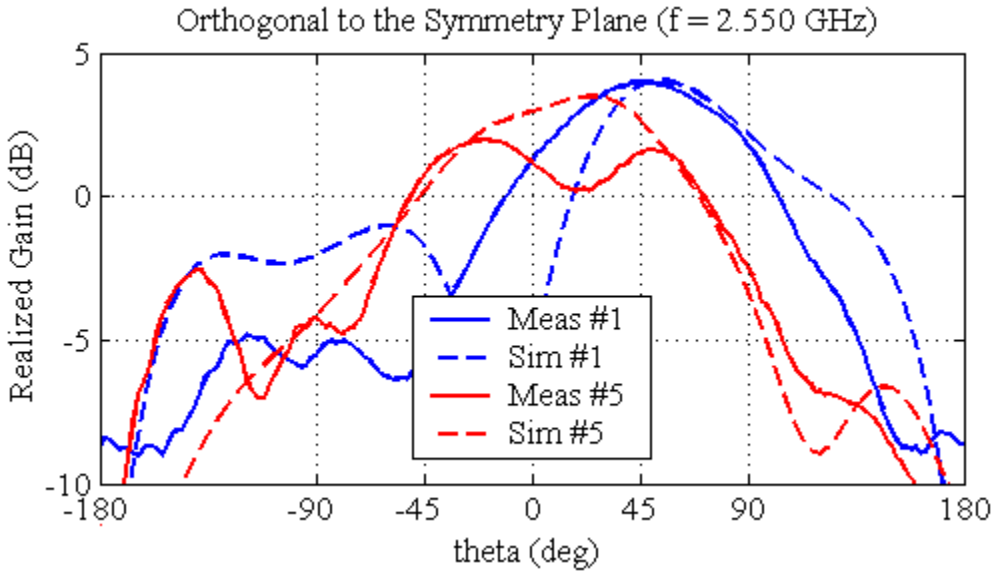

(a) Cross cut

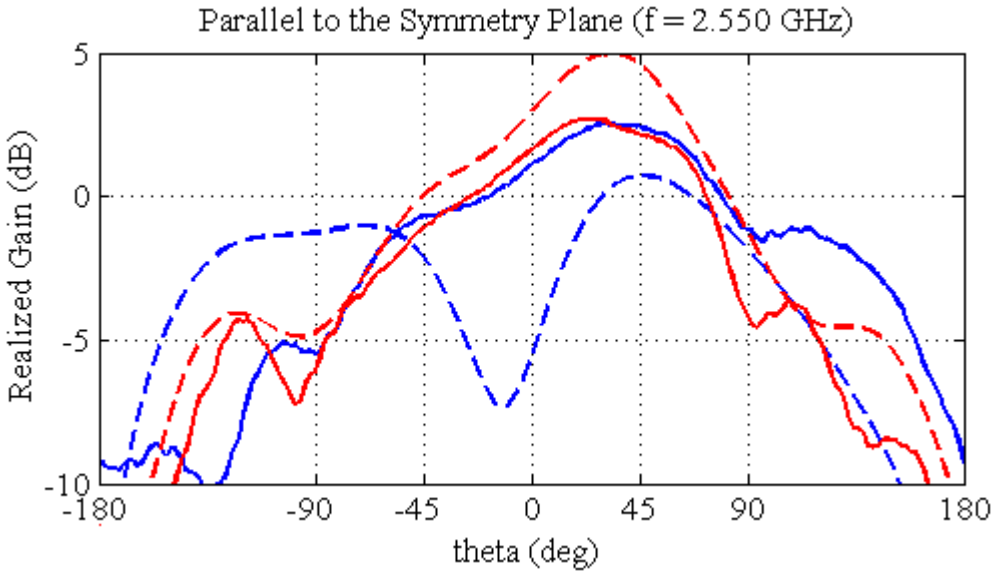

(b) Notch cut

Figure 1.11 Realized gain of Antennas #1 and #5 measured and simulated at 2.55 GHz

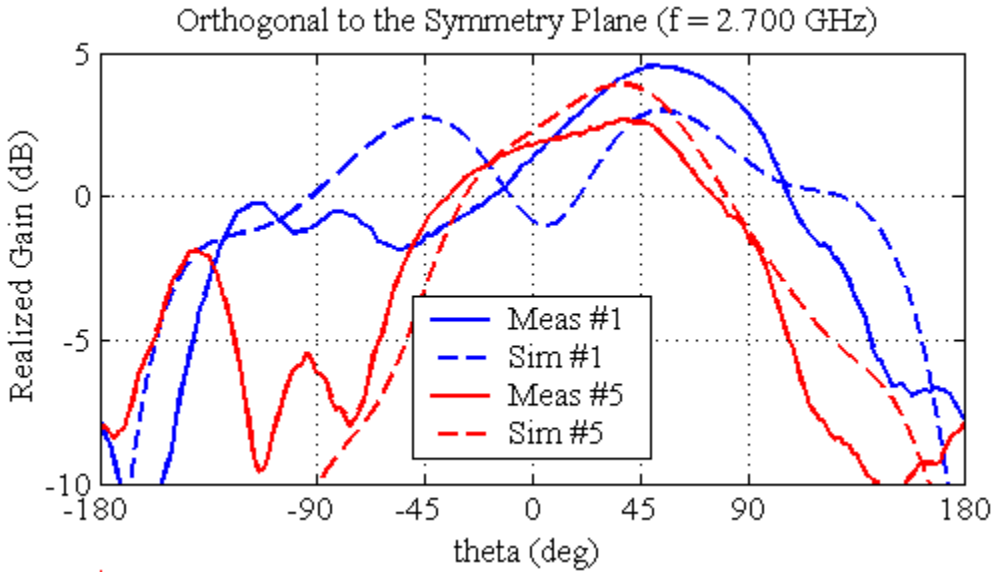

(a) Cross cut

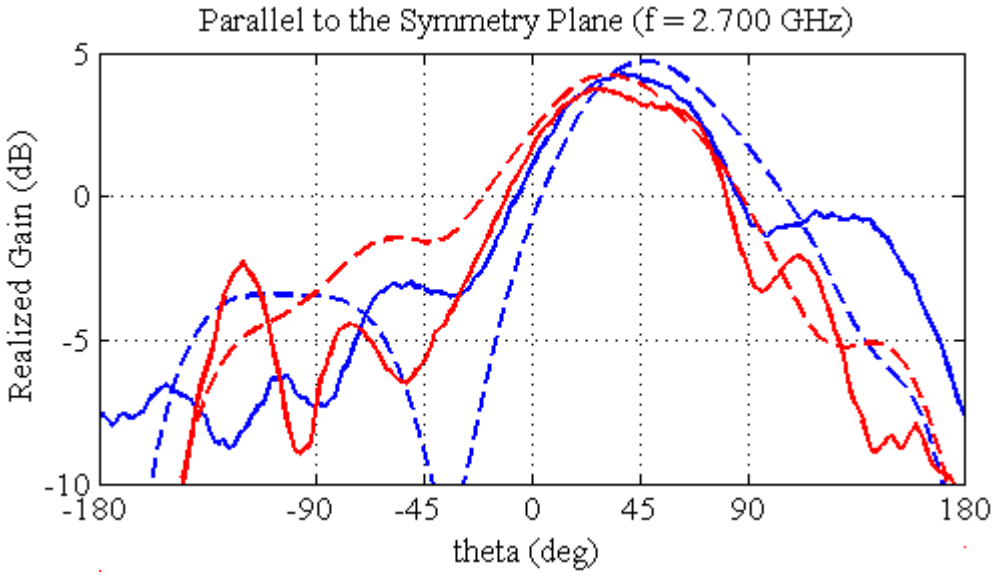

(b) Notch cut

Figure 1.12 Realized gain of Antennas #1 and #5 measured and simulated at 2.7 GHz

The original goal for creating the cupped-ground version of the ANSERLIN antenna was to provide a ground shape for focusing the radiated power broadside. For the cupped ground to have an effect on the radiation pattern, the flat portion of the ground must have a radius approximately equal to the outer radius of the annular sector, b. Then, if $\theta_{\text{cup}} = \pi/4$, the distance from outer edge of the annular sector to the top of the cupped ground is approximately the same as the height of the annular sector above the flat part of the ground. In particular in Figure 1.11(a) and Figure 1.12(a), the pattern is better centered broadside for the cupped-ground antenna. For most of the other frequencies, the two antennas have a comparable patterns, but overall, the cupped-ground antenna has fewer deep nulls than the round antenna.

In Figure 1.11(a) the simulated realized gain for Antenna #1 has a deep null near broadside that is largely absent in the measured data. Suspecting that the gain may be sensitive to the ground diameter, a modified version of Antenna #1 with a larger ground plane was simulated. The realized gain for this antenna is shown in Figure 1.13. These simulated results have more distinct nulls than the simulated results for the original Antenna #1.

Since Antennas #1 and #5 have different radiating lines and even heights, a cupped-ground variation of Antenna #1 was also simulated to make a more direct comparison between the round and cupped-ground versions. The results for the cupped-ground version of Antenna #1 are shown in Figure 1.14. In this case, the realized gain of the cupped-ground antenna is approximately 8 dB below that of the round antenna. However, the pattern shape has no distinct nulls at broadside and very little tilt to the beam.

It has been found that the size and shape of the ground plane have a significant effect on the radiation patterns produced by ANSERLIN antennas. Smaller ground planes and cupped ground planes tend to produce better gain patterns with fewer nulls to broadside. There are applications, however, where nulls are beneficial. If properly positioned, a null in the radiation pattern can be used to avoid interference from unwanted sources. With a large ground plane it may be possible to achieve nulls that can be used to avoid interference. Arrays of ANSERLIN antennas can be used to produce even more significant nulls.

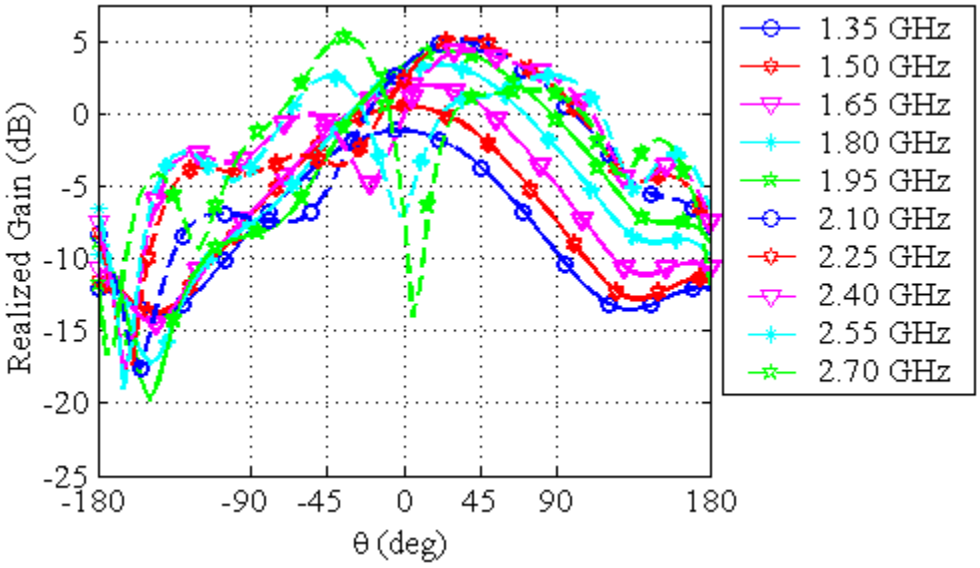

(a) Cross cut

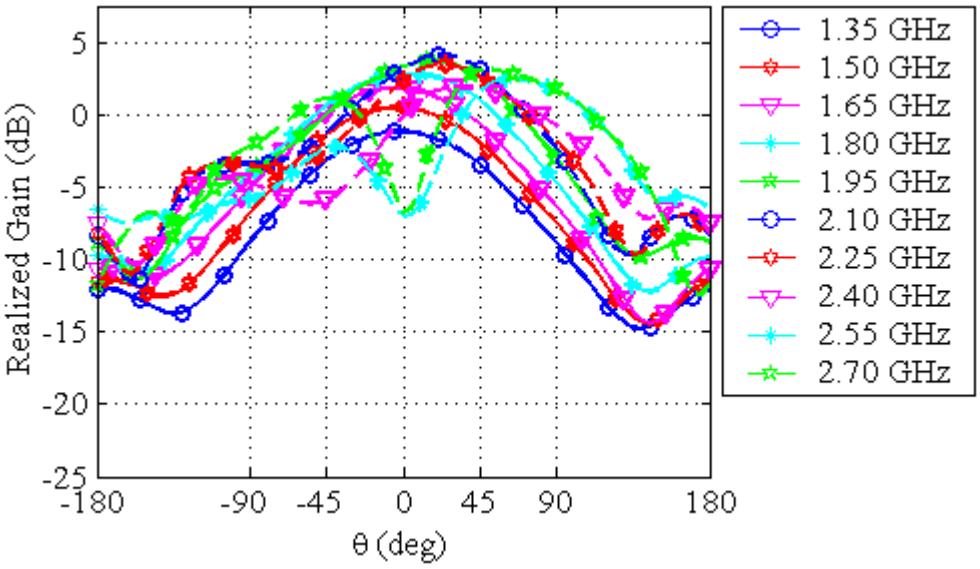

(b) Notch cut

Figure 1.13 Simulated realized gain for antenna based on #1 with a 4.7-in diameter ground plane

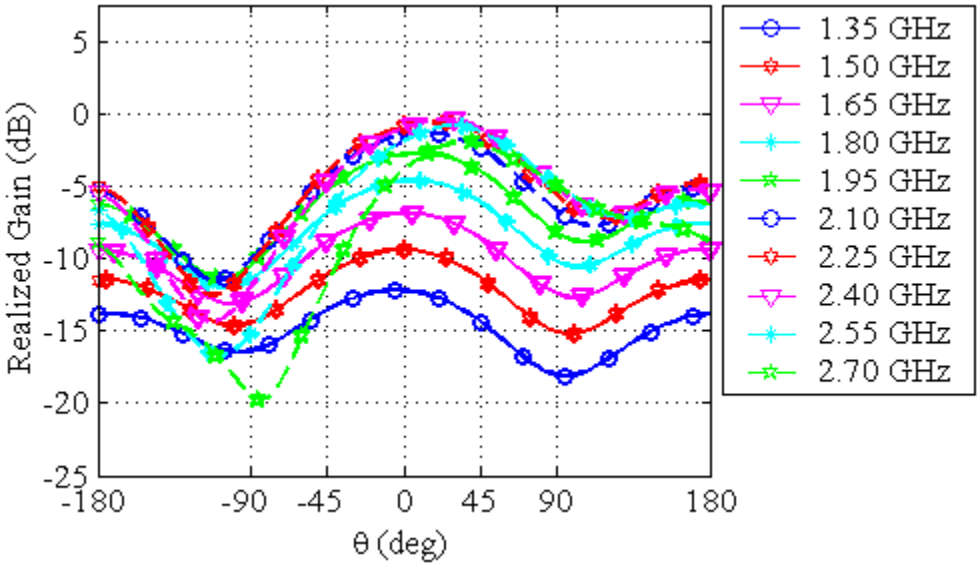

(a) Cross cut

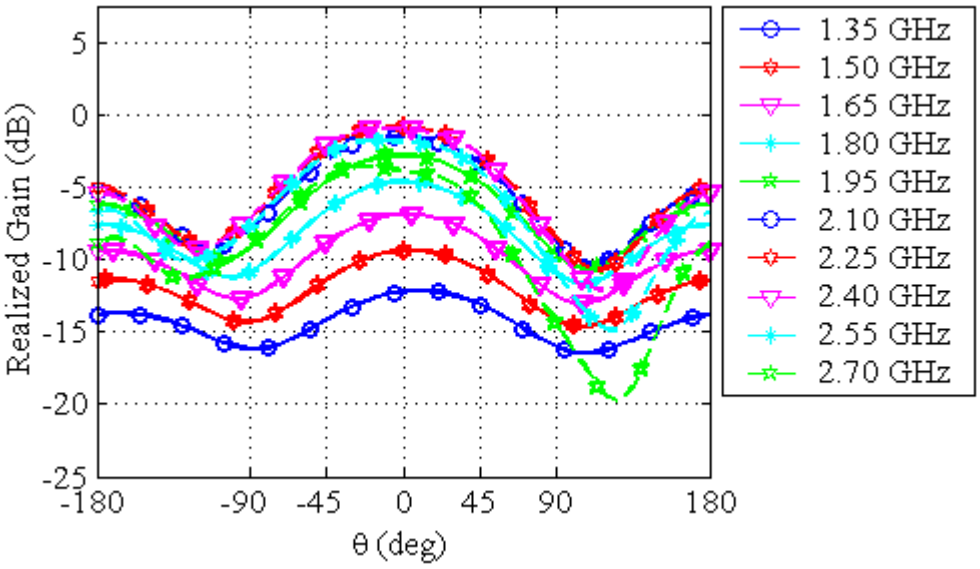

(b) Notch cut

Figure 1.14 Simulated realized gain for a cupped-ground antenna based on Antenna #1

1.4. MODIFIED FEED DESIGN FOR THE CUPPED GROUND ANTENNA

The feeds for the ANSERLIN design have typically been positioned below the ground with a center conductor or via connecting to the fin section. On dielectrics the fin is often much wider than the annular sector, requiring the transition section. All of these modifications affect the radiation pattern to some degree. In some cases the antenna becomes more linearly polarized.

The flat-feed antenna replaces the fin structure of previous ANSERLIN antennas by a tapered line that retains an approximately constant width-to-height ratio as the cupped reference plane drops away from beneath it. Figure 1.15 shows two examples of the flat-feed antenna. The annular sector and end-launch connectors were laid out on a 60-mil FR4 board. A foam block was cut with 45° edges and glued to the bottom of the board. The entire bottom of the antenna was covered in copper to provide the ground structure. This design is similar to the cupped ground antenna in Section 1.3. The flat-feed radiating line can be cut from a single piece of copper. In contrast the fins of the other ANSERLIN antennas are often too long to be cut out of a single piece of copper. When flat, the fins overlap. So, the radiating line is made in two pieces and soldered together. An array created from flat-feed ANSERLIN may be printed on a substrate with whatever other circuits needed. Then, the cupped cavities can be attached below the substrate.

Antenna #7 was first built with a radiating line shown in Figure 1.15(a). TDR measurements, shown in Figure 1.16, were used to find where the radiating line could be adjusted for a better match. The transition from microstrip to the annular sector had too high a characteristic impedance. An round addition of copper was laid over the existing fin to lower the characteristic impedance, as shown in Figure 1.15(b). The addition greatly improved the match without altering the main portion of the annular sector.

Both versions of this antenna extend the annular sector from 270° to nearly a complete circle. In [5] it was predicted that an antenna using more than 270° could radiate a larger percentage of its power. The S-parameters of this antenna indicate that it should radiate slightly more than 80% of the power incident on the antenna at its $m' = 1$ frequency around 1.65 GHz. The total radiation with respect to frequency is further discussed in Section 1.5.

The realized gain was simulated for both versions of the flat-feed antenna, Antennas #7a and #7b. Like the previous cupped-ground antennas, Antenna #7a is

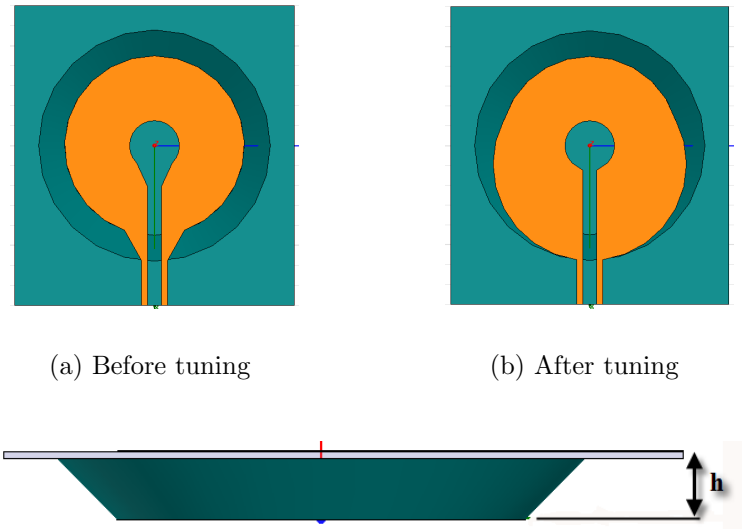

(a) Before tuning

(b) After tuning

(c) Side view of the flat-feed ANSERLIN

Figure 1.15 Two examples of flat-feed ANSERLIN antennas

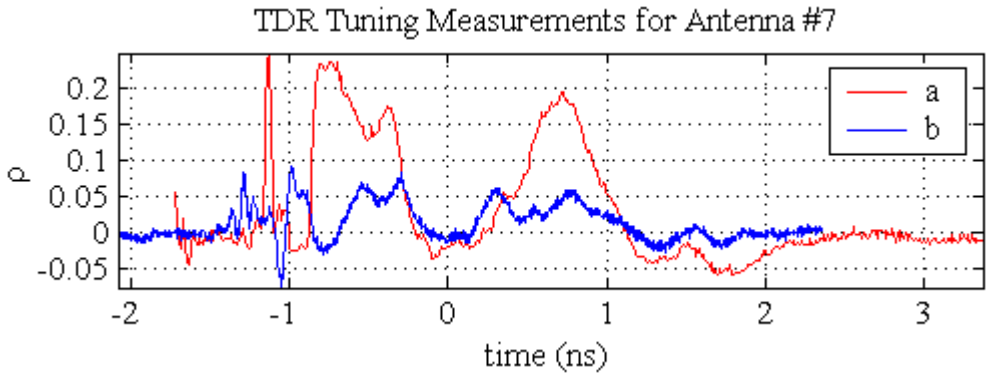

Figure 1.16 TDR measurements of the flat-feed antenna before and after tuning

shown in Figure 1.17 to have no distinct nulls at broadside. On the contrary, the tuned version of the flat-feed, Antenna #7b, has a substantially more distinct null at broadside in Figure 1.18. This is one example of how tuning for return loss may have adverse effects on the radiation pattern.

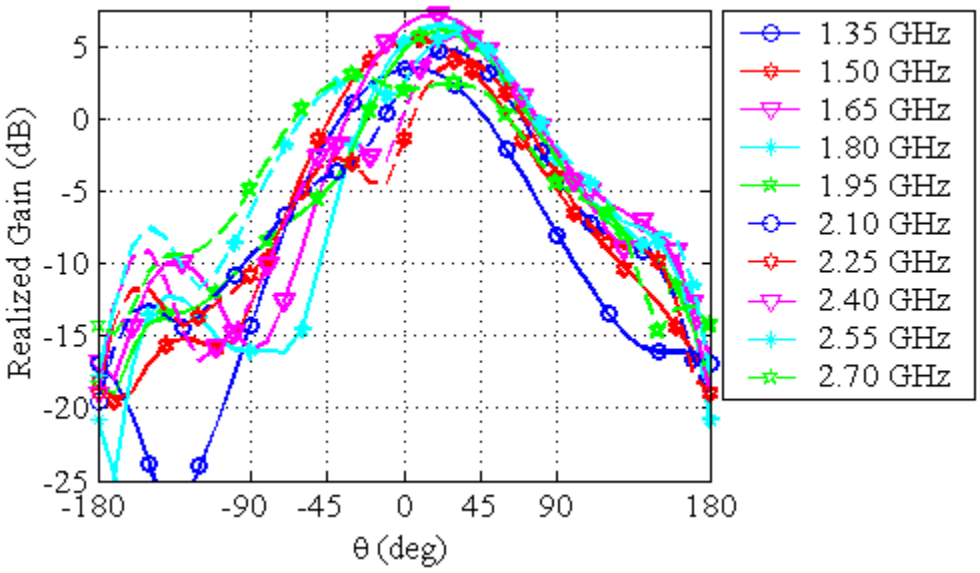

(a) Cross cut

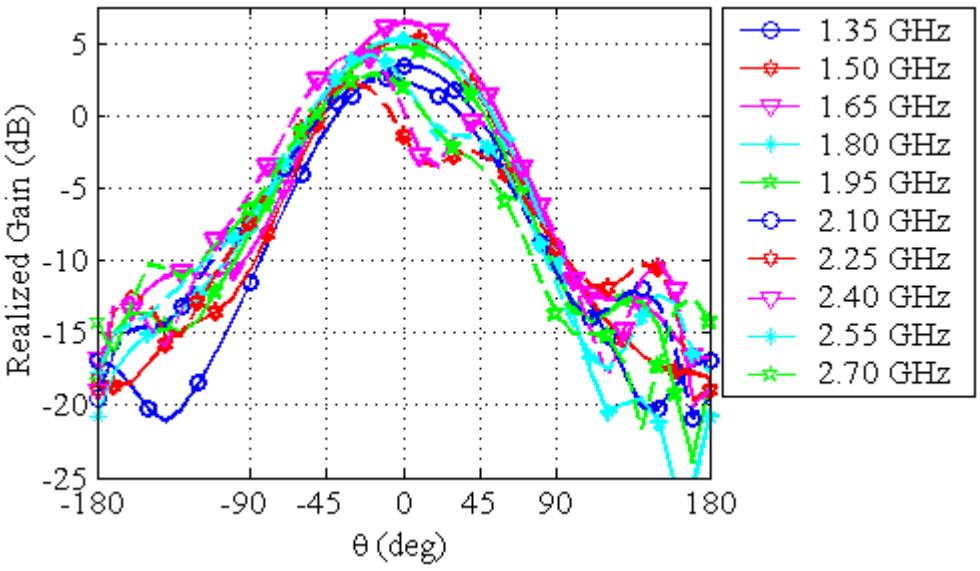

(b) Notch cut

Figure 1.17 Realized gain of the untuned flat-feed antenna

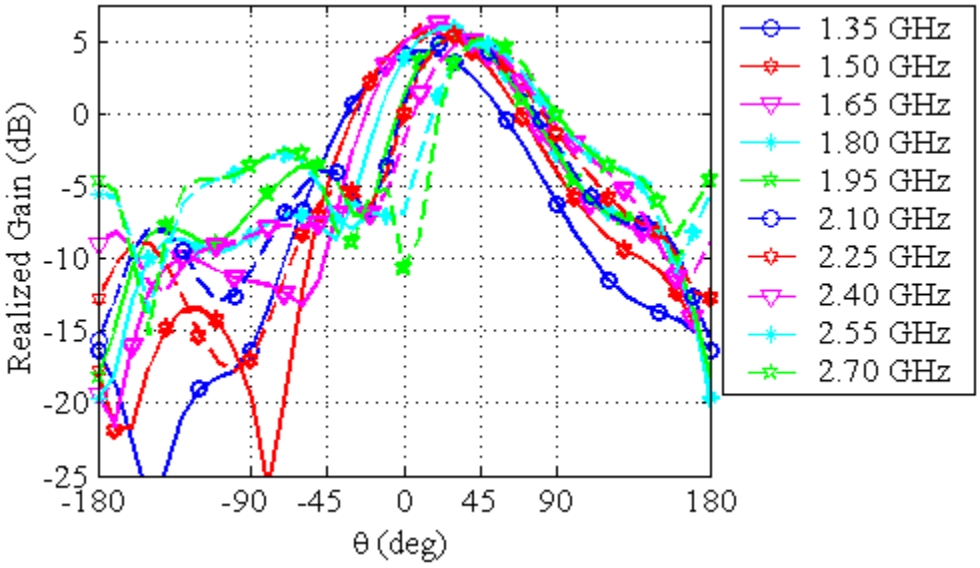

(a) Cross cut

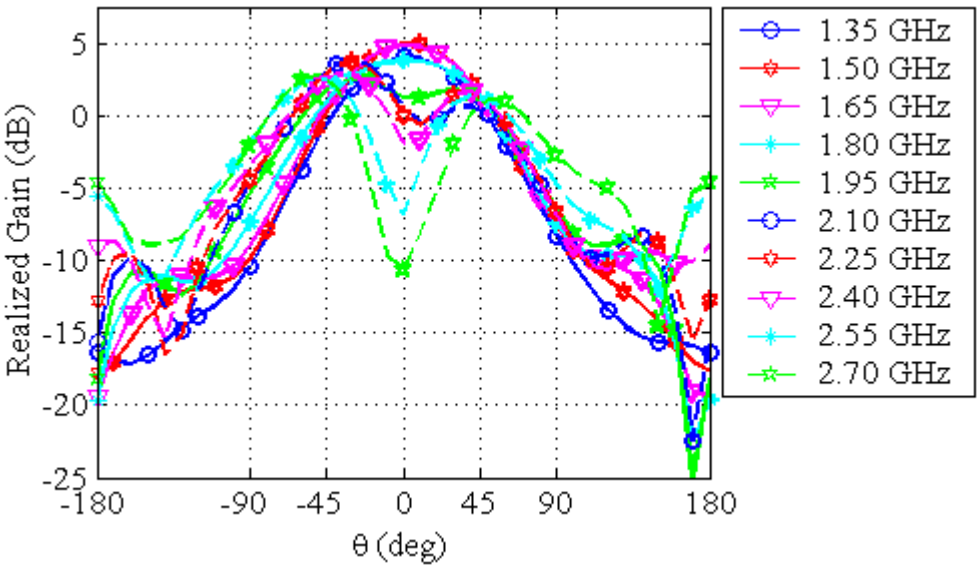

(b) Notch cut

Figure 1.18 Realized gain of the tuned flat-feed antenna

1.5. RETURN LOSS AND FRACTION RADIATED POWER OF THE RADIATING LINE WITH DIELECTRICS

Using dielectric materials for substrates for the ANSERLIN antennas allows smaller antennas to be made for the same frequency range. Microstrip equations can be used to calculate conductor widths approximately, but as discussed in Section 1.2.1, further tuning is commonly required to match the annular sector. Although some of these antennas were tuned using S-parameter or TDR measurements, the availability and speed of full-wave solvers has allowed many of the antennas to be designed using parametric sweeps of critical variables.

This capability was of special importance in designing the cupped-ground antennas and the flat-feed antennas, which do not conform necessarily to microstrip equations for straight or curved geometries. As pointed out in Section 1.2.1, the annular sectors typically have a lower characteristic impedance than the rest of the radiating line. Parametric sweeps can be used to tune the annular sector width regardless of the ground shape.

The S-parameters were measured for several of the antennas list in Table 1.1. Full-wave models of the same antennas were also generated. The results for $|S_{11}|$ are compared in Figure 1.19 through Figure 1.23 for Antennas #1, #2, #5, #7a, and #7b, respectively. Antennas #1, #2, and #5 use a dielectric with $\varepsilon_r = 9.7$; #7a and #7b are built on a 60-mil layer of FR4 above 1.3 cm of foam.

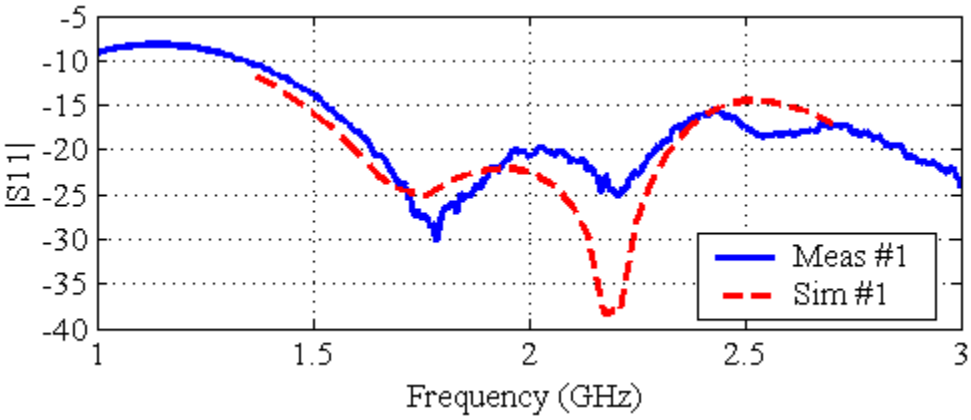

Figure 1.19 Return loss simulated and measured for Antenna #1

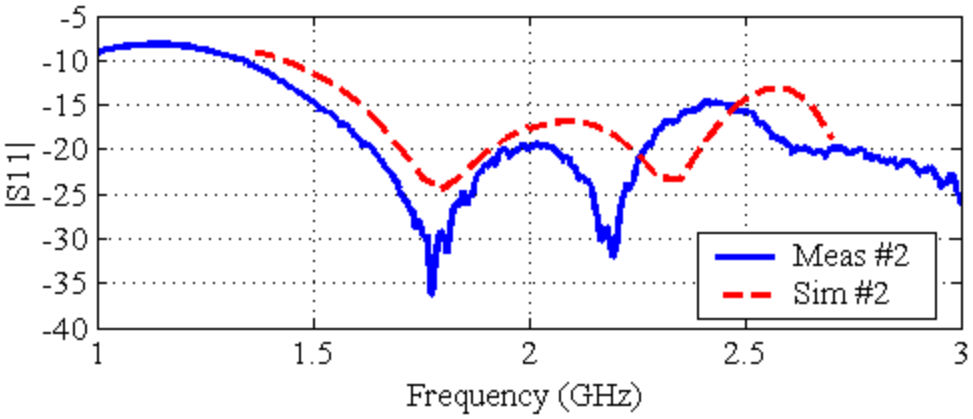

Figure 1.20 Return loss simulated and measured for Antenna #2

In addition to the return loss, the fraction radiated power is calculated as

$$FP_{rad} = 1 - |S_{11}|^2 - |S_{21}|^2 \, . \tag{1.7}$$

Several of the antennas discussed have their second port terminated by a 50-Ω resistor rather than a coaxial probe. Therefore, the simulated results for S_{11} and S_{21} are used to calculate the radiated power. The results are shown in Figure 1.24. Antennas #5 and #7a have distinct peaks in Figure 1.24. The round antennas have a nearly monotonic behavior in their radiated power. However, the radiated power for Antenna #7b is very flat compared with that of the other antennas. Tuning on Antenna #7b had some adverse effects on its radiation pattern, but the flatness of the total radiated power may be very useful in applications where directionality is not an issue.

In Section 1.3 the effect of large and small ground planes on round ANSERLIN antennas was discussed. Simulations on a version of Antenna #1 with a larger ground indicated that the radiation pattern for such an antenna had more distinct nulls at broadside. However, there is evidence in Figure 1.24 that indicates that reducing the size of the ground plane may also reduce the radiated power. Antennas #3 and #4 are identical except for their ground diameters. The radiated power of Antenna #4 is as much as 25% lower than that of Antenna #3 in the simulated results.

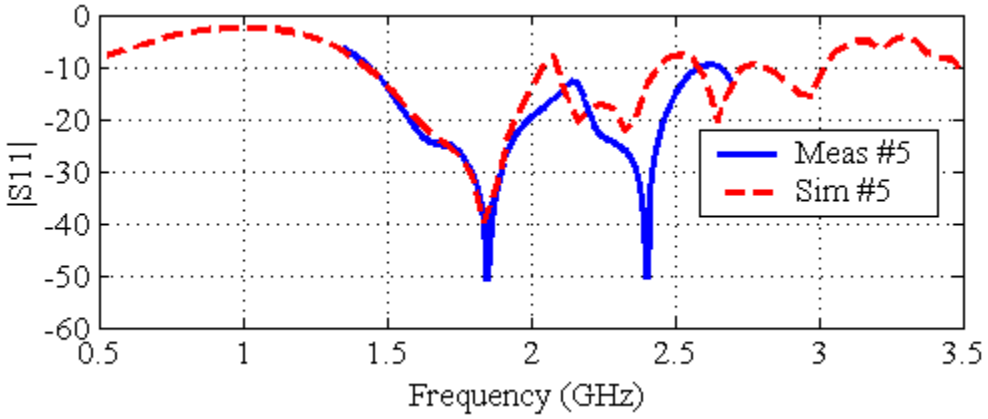

Figure 1.21 Return loss simulated and measured for Antenna #5

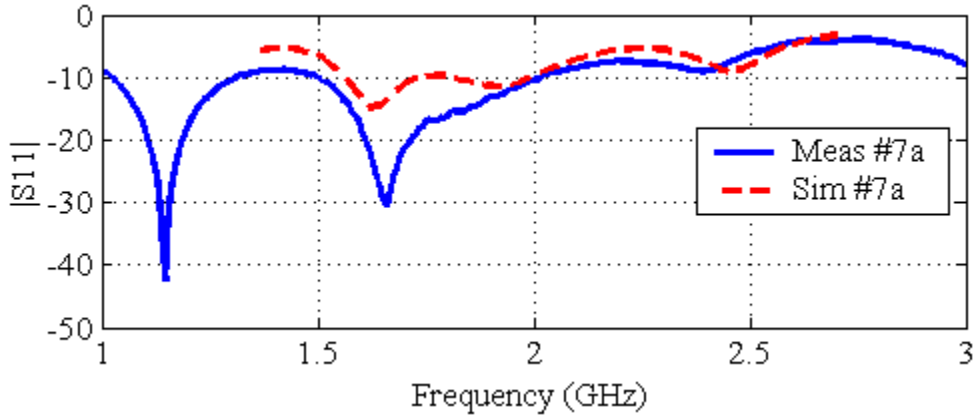

Figure 1.22 Return loss simulated and measured for Antenna #7a

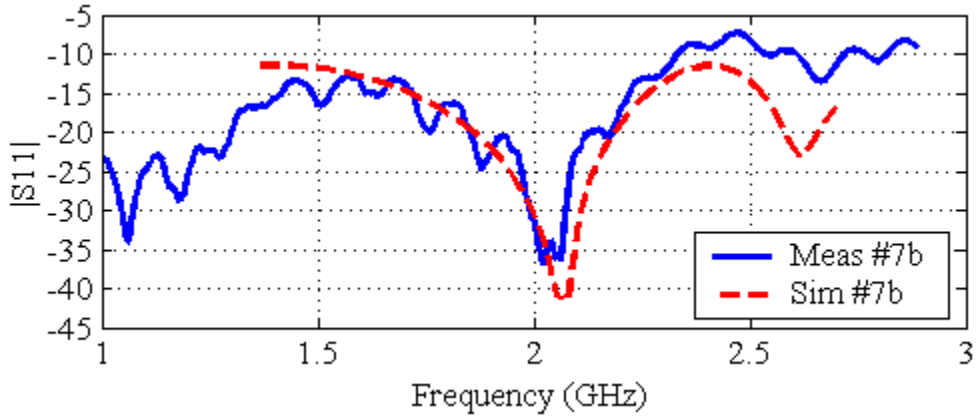

Figure 1.23 Return loss simulated and measured for Antenna #7b

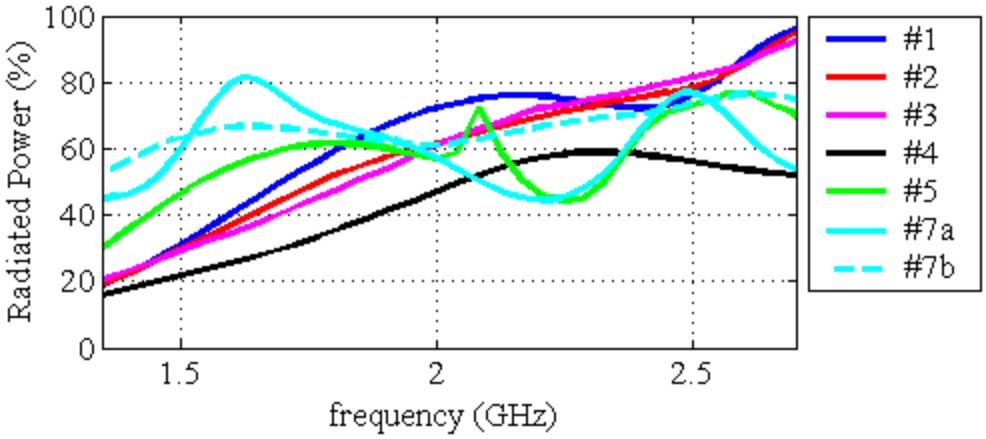

Figure 1.24 Fraction radiated power from simulated S-parameters for antennas in Table 1.1

1.6. SUMMARY

Previous studies of ANSERLIN elements have shown the antenna to have excellent wideband behavior with CP radiation. Dielectric substrate materials have been introduced in order to reduce the size of the element, and the annular sectors of the antennas have been tuned to achieve good return losses despite the added complexity of designing in the mixed media environment.

Additional work has been done on the return structures of the antennas. By cupping the ground structure near the ANSERLIN element, higher order modes are suppressed while maintaining reasonable levels of gain. Larger diameter ground structures have an inverse effect, accentuating these higher order modes to the extent that the $m' = 1$ mode is not observed at all. The result is a very distinct null at broadside for higher frequencies.

Considering the capabilities of the cupped-ground antennas, another new ANSERLIN configuration was designed that does not require the rising fin structures of previous antennas. This flat-feed ANSERLIN antenna uses the slope of the cupped ground antenna to make a matched transition to from microstrip to the annular sector. The flat-feed antenna can be printed completely on a substrate unlike other ANSERLIN antennas. The cupped-grounds may be fabricated separately an attached to the substrate. Several flat-feed antennas can be fabricated on the same substrate to form series or parallel connected arrays.

2. MODELING AND DESIGN OF A ANSERLIN MOBILE ANTENNA SYSTEM

The wide bandwidth and low-profile characteristics of the ANSERLIN antenna has led to its use for a mobile two-antenna array. The 3-dB power splitter for the system is incorporated into the base of one of the antennas. Several design factors come into play, requiring a full link-path model of the system. The system is electrically larger than what is easily handled by full-wave simulation. The output ports have different geometries, which make the output unbalanced. The unbalanced output results in a ripple in the S_{21} and S_{31}. The splitter itself requires matching and optimizing to ensure maximum power coupling and radiating from each antenna element. A previous version of the splitter is analyzed to find the cause for its poor performace. Then, the splitter is redesigned using the findings from the analysis.

The mobile antenna system is required to be both light-weight and compact. ANSERLIN antenna elements are used because they are a circularly polarized, radiating line antenna that can be matched across a large frequency range [5, 6]. These antennas can be reduced in size using dielectrics to the extent that they are two inches across and only a centimeter thick while retaining good radiation characteristics.

While the system could be constructed using two antennas and a commercial RF splitter, this leads to the added complexity of having three units to the design. A balun suiting this purpose was considered in [19]. Since ANSERLIN antennas are built over a finite ground plane, a custom splitter was designed using stripline geometries and built beneath the first antenna of the two-antenna system. Thus, the first antenna and the splitter share a reference.

The splitter board consists of two signal layers within two reference planes. The upper plane additionally acts as the return plane for the antenna. The planes are shorted at points for low impedance current returns and for basic splitter functioning. The stackup is given in Figure 2.1.

Unlike stand-alone board designs, the power splitter described in this report is designed for a specific antenna load. In addition, the splitter is integrated into the base of one of the two antennas of the system. The system is referenced to 50-Ω impedance. However, as needed, the splitter outputs can be modified to match the antenna input impedance. The layout of each splitter is specific to the antenna it is designed for since the antenna feed ports are relocated to match the feeds of the antenna design.

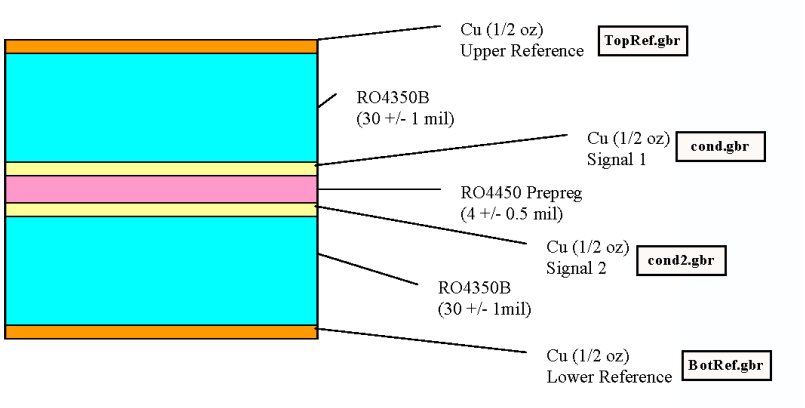

Figure 2.1 Stackup for the splitter board design

The design of the 3-dB splitter is complicated by the asymmetry of its output geometries. On a stand-alone board, the simplest design would entail laying out the input and two output lines with absolute symmetry, including identical connector geometries on the outputs. Because this power splitter is built into the base of one of the antennas, there are design constraints that eliminate the possibility of perfect symmetry.

A Marchand splitter design was originally considered for this design, and it is the configuration for the splitter analyzed in Section 2.1. The Marchand balun ideally provides a balanced, 180° output [35]. However, the output phase difference is irrelevant. The second antenna of the system requires a cable that will be a different length depending on the application. Thus, a simpler, less sensitive configuration, also using broadside-coupled lines, was considered for the redesign.

The port geometries are rebuilt in full-wave simulation in Section 2.1.1. These models themselves require care to ensure the circuit equivalents, derived from the model results, mimic the field structure when replaced in the system model. Equivalent circuits matching the simulation data are derived in Section 2.1.2. In addition to the port models, other parasitic quantities are introduced into the system model and manually tuned to achieve a close match to measured results in Section 2.1.3. Further discrepancies were corrected using several partial full-wave models. The splitter, minus the connecting striplines, was simulated in a full-wave solver in a fashion so that the results could be linked back to the port models.

The information gleaned from the analysis in Section 2.1 is utilized in Section 2.2 to design a new splitter with less output imbalance and better return loss.

In Section 2.2.1 a different termination scheme for the coupled lines is considered analytically. This new configuration is incorporated in the steps to build a splitter matched to the characteristics of the ports in Section 2.2.2. Lastly, the characteristics of the new splitter are compared with that of previous versions.

2.1. SYSTEM-LEVEL ANALYSIS OF THE PREVIOUS SPLITTER DESIGN

The previous splitter was measured and found to have substantially different S-parameters than previous simulations of the splitter geometry. The difference could not be explained by either full-wave or SPICE simulations of the splitter element alone. This reasoning placed the focus of the analysis on the port geometries, which had not been analyzed with the level of detail that the splitter element had.

Full-wave analysis and circuit extraction are used to further understand the behavior of the port geometries. First, the port geometries are simulated with full-wave modeling techniques. Then, equivalent circuits are designed that relate directly back to the geometry. Additionally, a transmission line model of the splitter element is constructed, and the port models are included to get the full-system model.

2.1.1. Full-Wave Models of the Port Geometries. The complete splitter board is too large and complex to easily model in a single full-wave model. It is not impossible, but impractical in most cases. For example, the number of tetrahedron for a finite element solve required for a satisfactory model can exceed one hundred thousand. This number of tetrahedron is large, but not impossible to run on a computer with 2 GB or more RAM. In this paper the system is considered separately first and then pieced together to get a full system response. The port geometries are first considered. Figure 2.2 shows the port geometry models referenced to their position in the layout.

Two of the three port geometries are nearly identical. The input port, Port 1, and the second output, Port 3, are both fed by a coaxial cable soldered horizontally to the upper plane of the splitter. The difference in the two models comes from the output traces being on the lower signal layer while the input trace is on the upper signal layer. The first output, Port 2, is connected to a vertically mounted coaxial cable. In the assembled system, this port feeds the antenna element mounted above the splitter. When assembled, a wire is fed through the splitter board to the antenna element above, but for the characterization measurements a semi-rigid coax is used. This difference in testing and final implementation further complicates the design

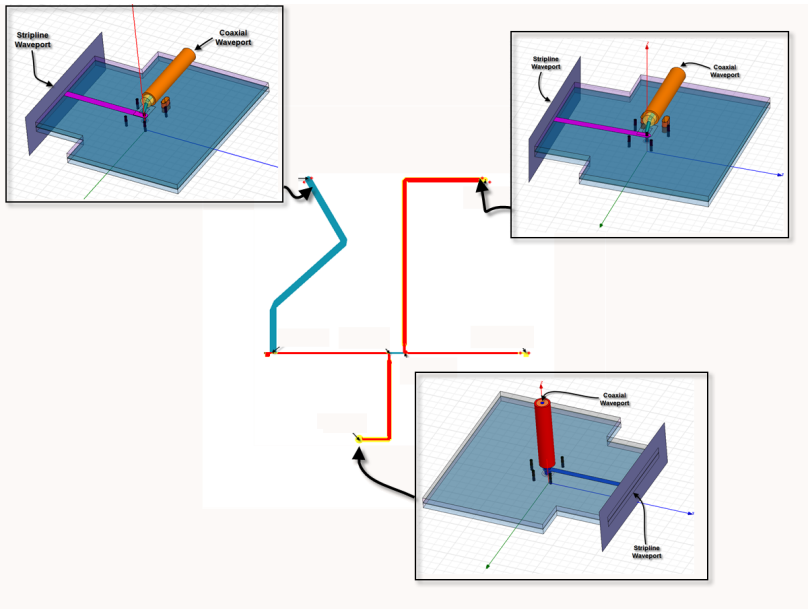

Figure 2.2 Port geometries associated with their respective positions in the splitter layout

process, as the test measurements may differ significantly from the behavior of the assembled system.

Constructing a full-wave model that accurately represents the physical device is often difficult. Regardless of the full-wave method employed, two important elements can render the model completely inaccurate: excitation and boundary conditions. If applied in a way that does not represent the proper physics, the modeled results will not match the physical device. Proper excitation and stripline modeling are critical in the port models, because the geometry cannot be measured separate from the rest of the board. However, in the models, the port geometries can be cut away from the rest of the board geometry provided the boundary conditions are matched such that the models fit seamlessly back into the system model.

In the port models considered in this section the most important elements in each model include the stripline termination and excitation. The SPICE model of the splitter uses transmission line elements that assume a stripline field distribution. The full-wave models or their equivalent circuits are constructed to minimize the reflections from the interface of the port models and the splitter model.

Assume that a stripline in a full-wave model is excited against only one of its two references. Figure 2.3 shows the current distribution associated with this excitation

and also shows the current distribution associated with a stripline excited against both references. The microstrip style excitation leads to a larger current density on the lower reference and a much lower current density on the upper reference. This distribution is not suitable to match with the field distribution of the transmission line model.

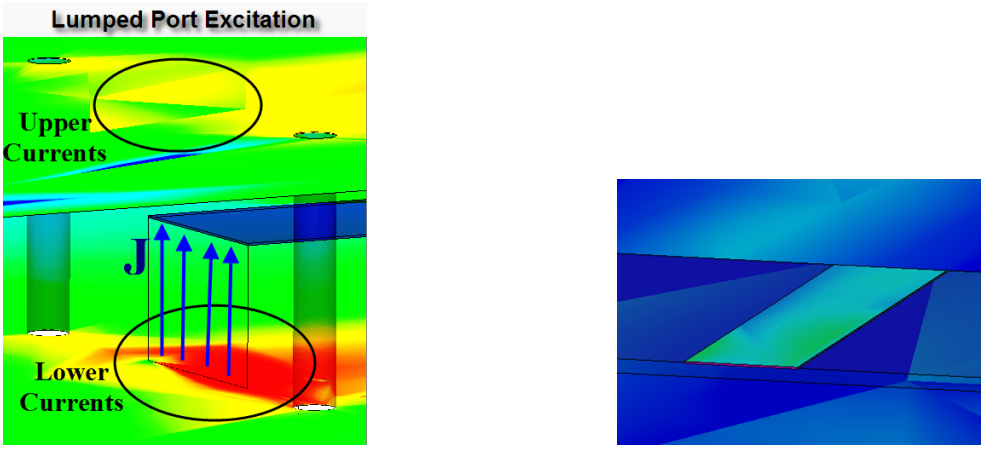

(a) Excitation against a single reference plane

(b) Excitation against both references planes

Figure 2.3 Stripline excitations and the current distribution

In addition to exciting the stripline in a way that matches the transmission line model, it is also important to model enough of the stripline so that non-TEM modes are attenuated. The traces separating the ports and the splitter geometry are too short for full attenuation of the non-TEM modes. So, the traces are extended in the model, and the added electrical length is removed in post-processing. This step is referred to as de-embeddin the port. Figure 2.4 and Figure 2.5 show the input port and the first output port, respectively. The effective port locations with de-embedding are indicated. In order to define a port to connect to lumped circuits, the voltage must be clearly defined at the port boundary. An accurate voltage definition is possible with an electrically small conductor separation and TEM fields present at the port. This condition is also required to extract an equivalent circuit of the geometry, which has lumped circuit ports itself.

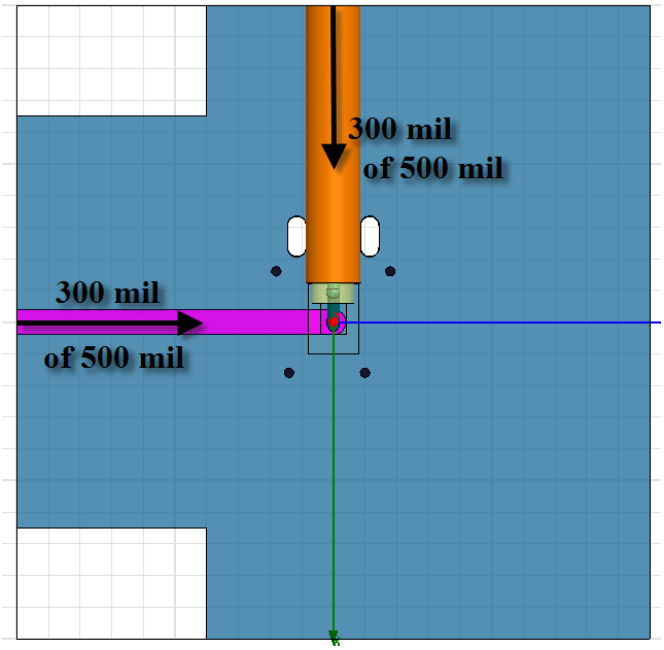

Figure 2.4 The splitter input port model with arrows to indicate the effective port locations after de-embedding

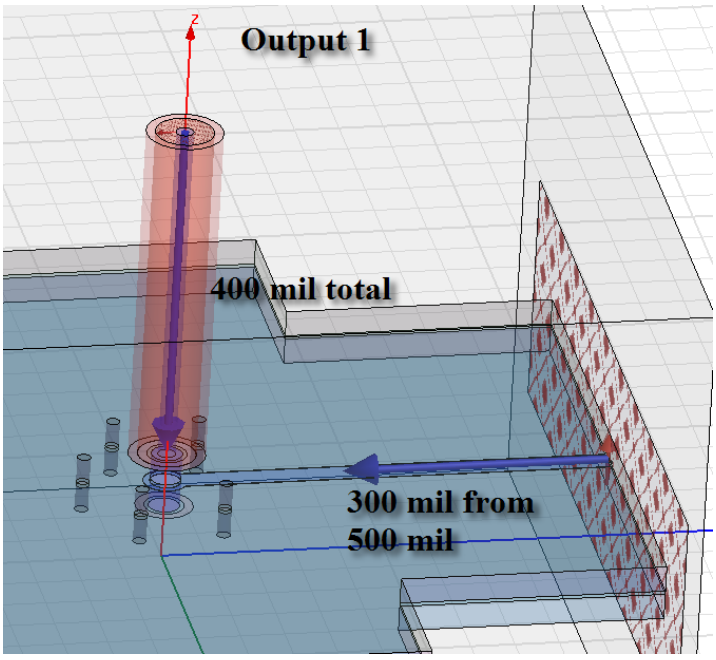

Figure 2.5 The model of the output feeding the attached ANSERLIN antenna with arrows to indicate the effective port locations after de-embedding

When completed, an ANSERLIN antenna element with dielectrics will be attached to the upper surface of the splitter. This condition is different than in the models shown in Figure 2.4 and Figure 2.5. The final forms of the port geometries include dielectrics similar to those represented in the models in Figure 2.6. However, the coaxial connections are needed for the splitter measurements. So, two sets of port models are required: one for matching measurements and a second for system design.

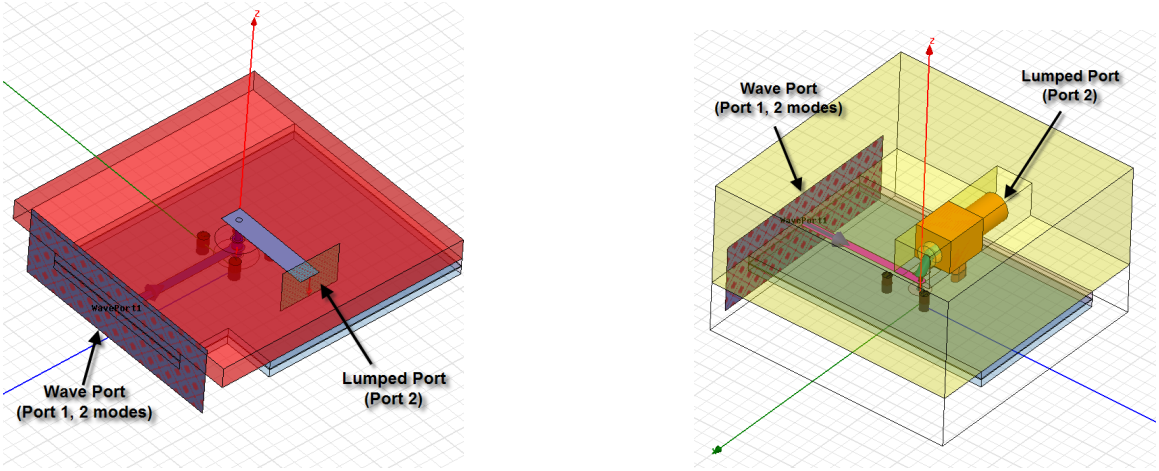

(a) Antenna feed geometry

(b) Feed with antenna dielectric and cable clamp

Figure 2.6 Full-wave models for the feed ports for the completed system

The port geometries have been assumed to be the most significant factor in the poor characteristics of the design. While the connections must remain the same in general, the antipad radii for the via connections can be changed. Parametric studies, using the full-wave models described previously, were used to find a radius for each port that minimizes reflections. Making the antipads too small results in excessive coupling from the via stub to the lower plane. However, if the antipad is made too large, the connection may have too much inductance. Finding the balance is essential.

For the antenna feed, S_{11} was observed to decrease as the antipad size increased in Figure 2.7. However, a dip around 2.1 GHz occurs for larger radii. While the simulation indicates this as being a great match at the center of the frequency band,

it may also indicate that the sensitivity of the response at that size is high. Small variations in the antipad size in construction may result in narrow band response as a worst case.

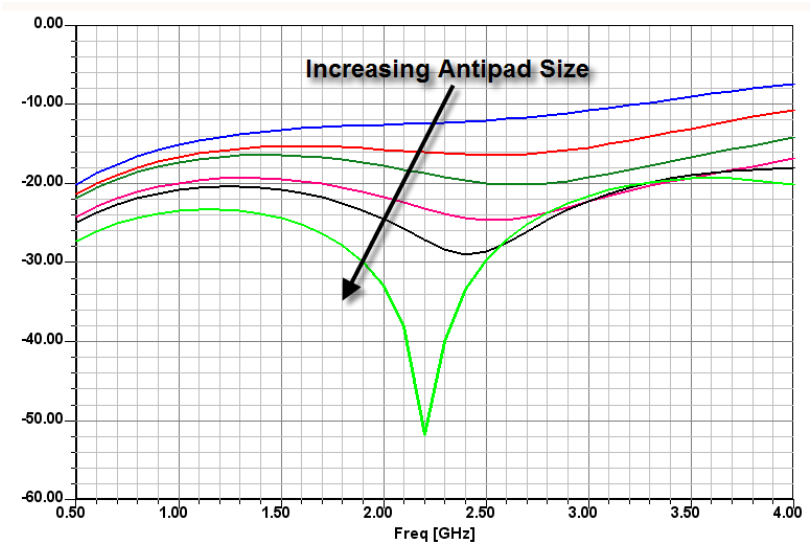

Figure 2.7 $|S_{11}|$ for the antenna feed geometry given different antipad sizes

The input feed geometry presents a slightly different behavior with respect to the antipad size. The constants in the goemetry are the 15-mil via diameter and the 25-mil via pad. Figure 2.8 indicates that the return loss initially decreases, and then increases. Increasing the antipad diameter by approximately 20 mil brings the return loss back to almost the same as the initial diameter. At this point in the analysis the accuracy of the model must be considered. The return loss is low enough for any of the cases, and the difference in the return loss is roughly 6 dB. In this case, a median antipad diameter was chosen.

2.1.2. Current Mapping and a Physics-Based Circuit Extraction. Translating complex geometries into equivalent circuits provides an alternative model that can be simulated quickly and connected to other models in SPICE simulators. Then, anything that can be simulated in SPICE can be tested with the geometry. Often it is possible to match the behavior of complicated structures at low frequencies with very simple second or third order circuits. However, the simplest circuit that fits may not always be the best circuit to use. Designing an equivalent circuit based

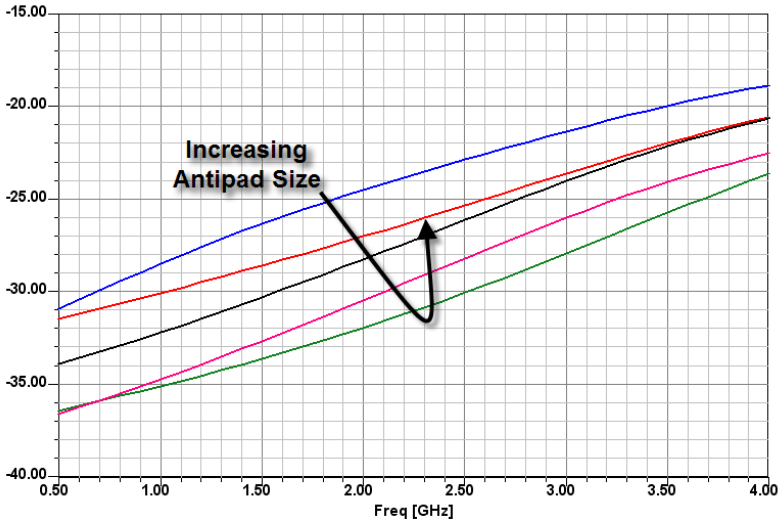

Figure 2.8 $|S_{11}|$ for the coax feed geometry given different antipad sizes

on the physics of the geometry can yield a circuit that not only matches the behavior of the struture but also gives interpretation of how the individual elements of the structure affect the overall response. This idea is demonstrated with the splitter port geometries.

Two-dimensional representations of the port geometries are shown in Figure 2.9 and Figure 2.10. The analysis begins by mapping all possible current paths, both conducted and displacement, on the diagram. Conducted currents (in green) translate to inductances, and displacement currents (in red) translate to capacitances. Then, the equivalent circuit components can be drawn directly over the diagram and connected to get the circuit. From this procedure the geometry is directly related to the equivalent circuit, and behaviors associated with particular circuit elements are directly related to an element of the geometry. Therefore, if the behavior of the circuit can be improved by adjusting an equivalent circuit value, then, the physical change required to achieve the functional change is straight forward.

Optimizations in Agilent's Advanced Design System (ADS) were combined with the S-parameters simulated in Ansoft HFSS to match the parasitic values. Table 2.1 shows the circuit quantities determined from the optimization in ADS. Figure 2.11 shows the equivalent circuit structure. Although the port geometries differ, their current paths lead to the same equivalent circuit structure. Each port has different values for the equivalent circuit elements.

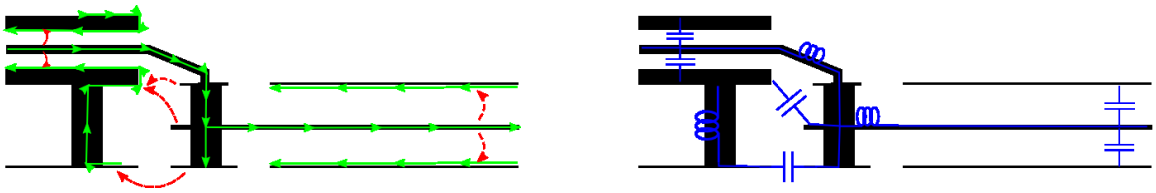

(a) Current paths

(b) Equivalent circuit elements overlaid on the geometry

Figure 2.9 A 2D diagram of the geometry for the input and second output ports with the conduction and displacement current paths indicated

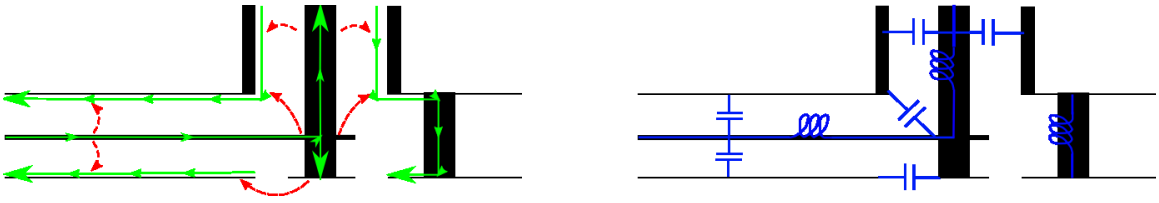

(a) Current paths

(b) Equivalent circuit elements overlaid on the geometry

Figure 2.10 A 2D diagram of the geometry for the first output port with the conduction and displacement current paths indicated

Table 2.1 Equivalent circuit quantities

	Lcenter (nH)	Ltrace (nH)	Lsvia (nH)	Ccenter (pF)	Cmid (pF)	Ctrace (pF)	Cstub (pF)
Input	1.91	1.27	0.013	0.309	0.341	0.258	0.391
Output 1	0.715	1.00	0.263	0.362	0.165	0.168	0.252
Output 2	1.94	1.48	0.052	0.326	0.259	0.223	0.427

These equivalent circuits are by no means the only possible structures that could match the S-parameters, but they are sufficient for matching the simulated S-parameters and reflect the physics of the geometry. Note that the components in

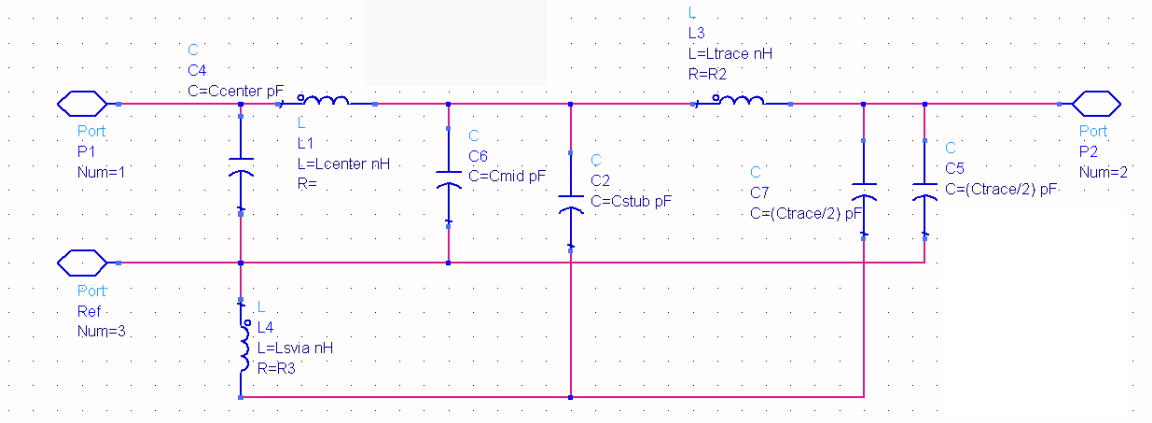

Figure 2.11 The equivalent circuit used to model the port geometries

Figure 2.11 match the circuit elements overlaid on Figure 2.9 and Figure 2.10. Previously, the antipad radii for each of the ports was determined to be too small. That is evident in the value of Cstub. This parameter can be tuned in SPICE simulations to quickly find the best response. Then steps may be taken to find the antipad size to achieve a close match to the optimal parameter value.

2.1.3. Transmission Line System Model with Port Circuit Models. The splitter design comprises offset stripline, broadside coupled striplines, shorting vias, and the port geometries. The port geometries have been considered in detail in the previous sections. To complete the system level model, the splitter element itself is represented by transmission line elements and multiconductor transmission line models. A schematic representation was assembled in ADS. Subcircuits for the port equivalent circuits are added to the transmission lines. Figure 2.12 shows the schematic representation of the system.

Initial simulations showed significant discrepancies between the simulated and measured results. Assuming the port models to be correct, the rest of the splitter geometry was scrutinized. Like the port geometries, there are discontinuities in the splitter that exhibit non-TEM fields. The previous model, based on transmission lines did not account for the non-TEM fields. Therefore, additional parasitic components were added to the previous model where significant discontinuities existed. After the additional parasitics were added and manually tuned, the simulated and measured data matched fairly well although there are still some discrepancies. It has been demonstrated on the port geometries that physics-based equivalent circuits can be constructed to match the complex behavior exhibited. The same could be done for

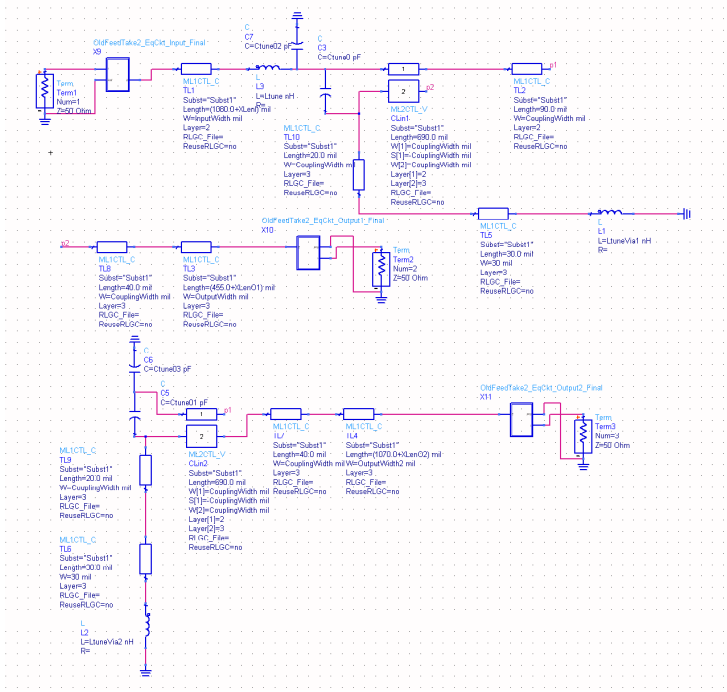

Figure 2.12 The system level model including equivalent circuits for the ports, transmission lines for the splitter, and additional parasitic components to account for other non-TEM mode effects

parts of splitter. Instead a frequency domain full-wave model of just the splitter was constructed.

Figure 2.13 shows the full-wave model of the splitter. As with the port geometries, the conductors were extended to allow the non-TEM modes distance to attenuate prior to reaching the simulation ports. De-embeding was then used to remove the excess length of conductor. The extra length of line is important to avoid reflections from the port. Such reflections would not occur in the real device and must be avoided in the model.

The S-parameters from the simulation of the model in Figure 2.13 are used with the equivalent circuit models for the port geometries. This schematic is shown in Figure 2.14. The results for both the transmission-line based model and the full-wave splitter based model are shown in Figures 2.15 to 2.20. In general, the full-wave (FW) splitter model agrees with the measurements better than the hand-tuned transmission-line (Tx) model for the splitter.

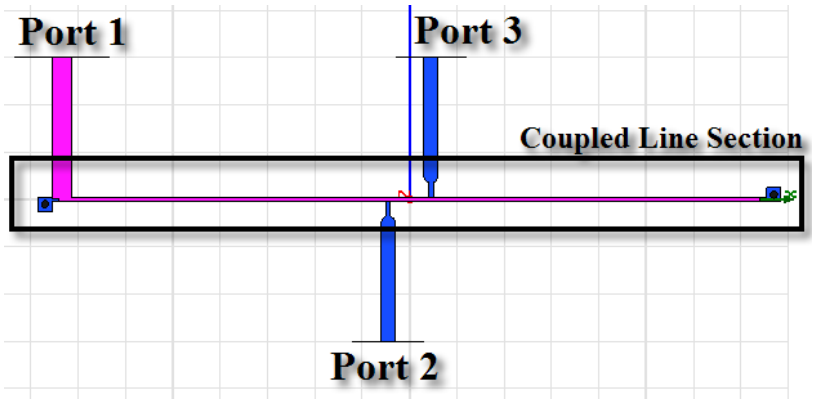

Figure 2.13 The reduced full-wave model isolating the complex fields associated with the coupler and its connecting traces

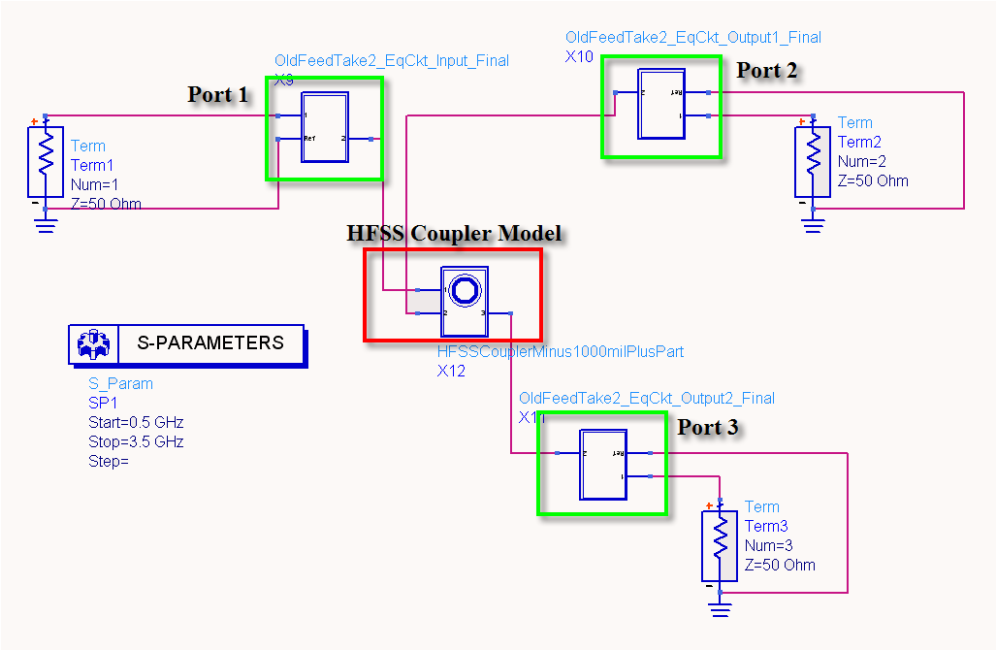

Figure 2.14 The combined system model including the port equivalent circuits and the full-wave splitter model from Figure 2.13

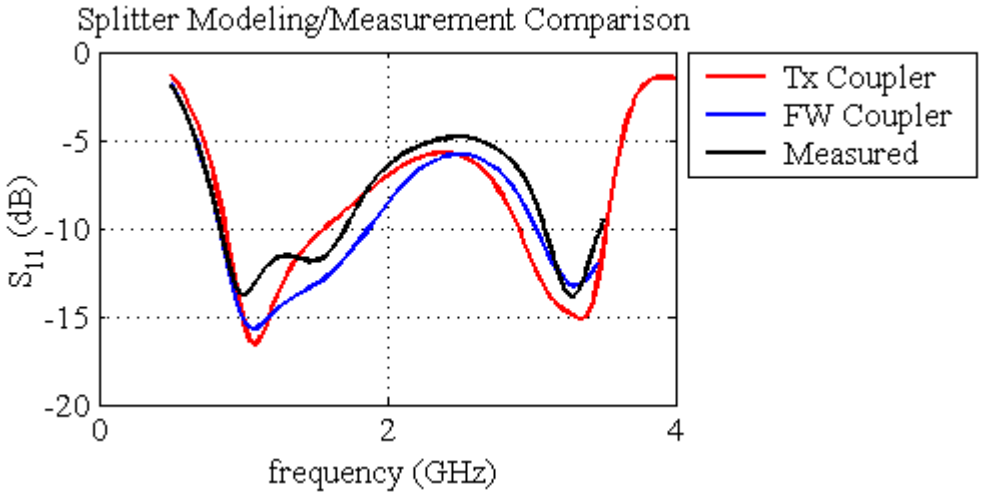

Figure 2.15 Splitter modeling and measurement comparison (S_{11})

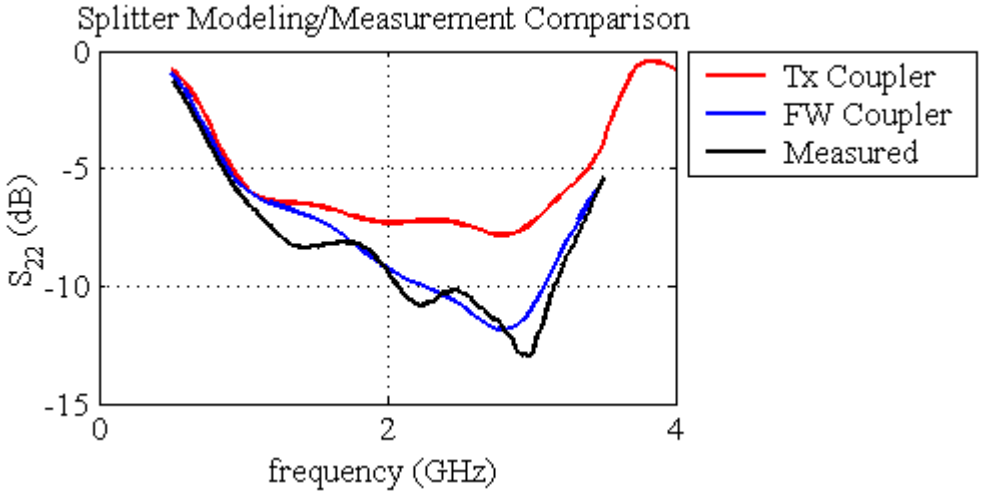

Figure 2.16 Splitter modeling and measurement comparison (S_{22})

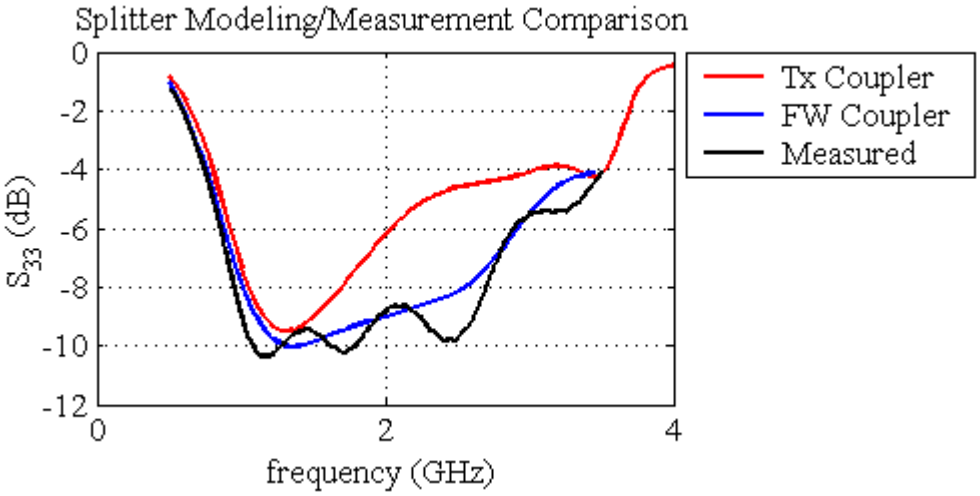

Figure 2.17 Splitter modeling and measurement comparison (S_{33})

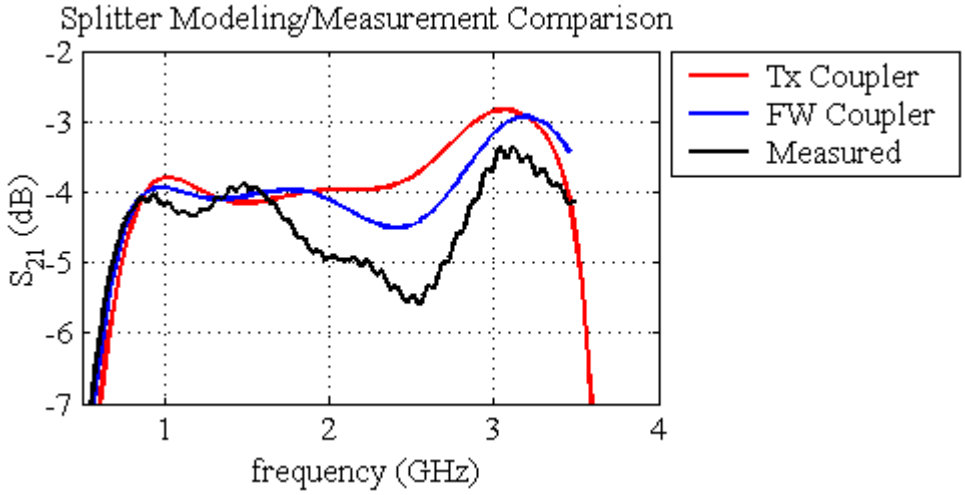

Figure 2.18 Splitter modeling and measurement comparison (S_{21})

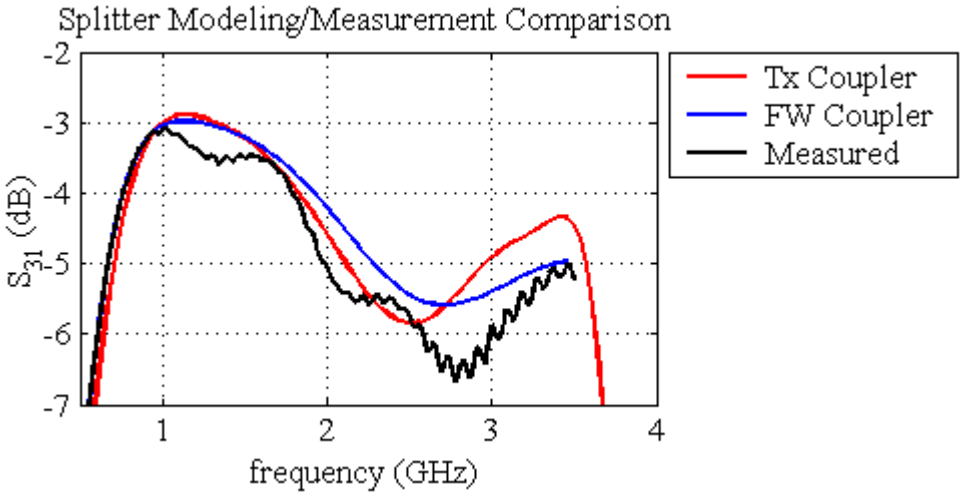

Figure 2.19 Splitter modeling and measurement comparison (S_{31})

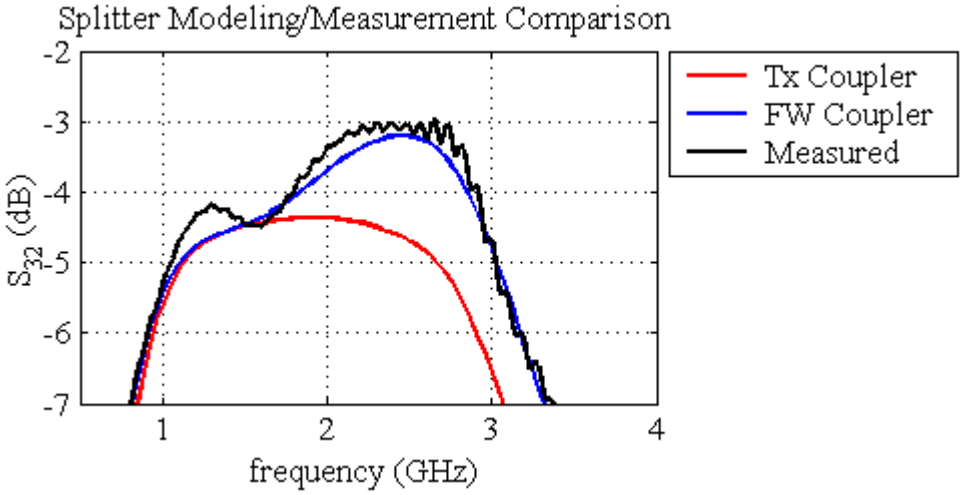

Figure 2.20 Splitter modeling and measurement comparison (S_{32})

2.2. SPLITTER REDESIGN

Given the knowledge of the port behavior from the previous design, a new design is constructed. Some modifications are made to the splitter element itself, allowing the coupled output lines to be connected in parallel rather than in series. Figure 2.21 shows a simplified diagram of this new splitter. The reasoning for that change is presented in the next section.

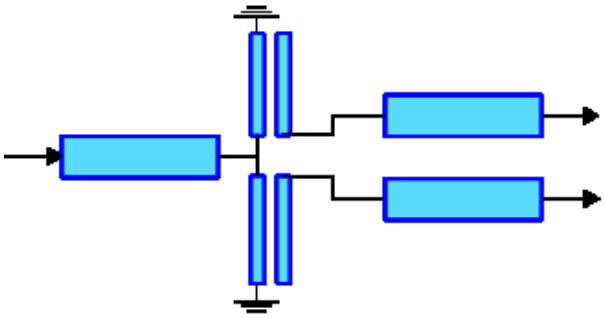

Figure 2.21 The new splitter configuration using two sets of coupled lines in parallel

2.2.1. Analysis of the Coupled Lines. The new splitter design functions using two coupled-line sections in parallel. The design is a variation of the Marchand balun, which provides 180° phase difference in its outputs. This splitter uses a very similar coupled line combination, but feeds them in parallel instead of series. In addition, the input inpedance seen at the input to the coupled line pair is approximately 50 Ω. Then, the transmission line widths selected are only slightly narrower or wider than a 50-Ω trace.

First, consider a single coupled line section. Figure 2.22 shows Line 1 shorted at the far end while Line 2 is open. The near side of Line 1 is assumed to be the input of the structure, and the near side of Line 2 is the output, which have a load connected. Cross-sectional analysis yields the per-unit inductance matrix for the pair of lines to be

$$L = \begin{bmatrix} l_s & l_m \\ l_m & l_s \end{bmatrix}$$

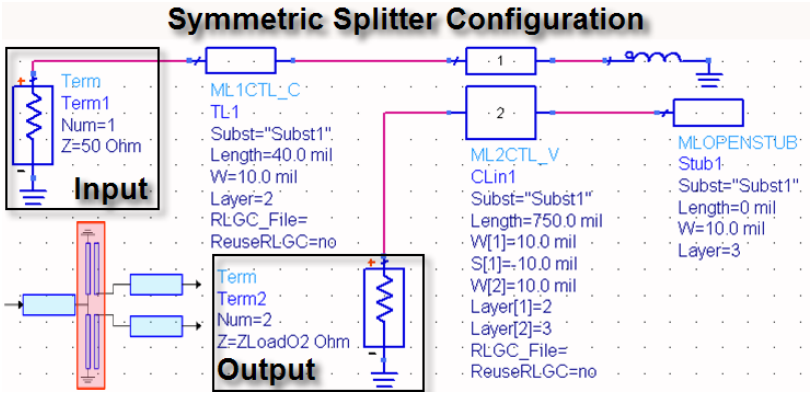

Figure 2.22 Circuit model for the broadside coupled striplines

and the per-unit capacitance matrix is

$$C = \begin{bmatrix} c_s & -c_m \\ -c_m & c_s \end{bmatrix}$$

These lines have symmetry and could be analyzed using simplifications for symmetric coupled lines. However, in this case, the lines and their terminations were analyzed using a multiconductor transmission line (MTL) formulation.

A modal transformation is used to relate the line voltage and current to even and odd mode signals. The transformation matrix is given by

$$T = \frac{1}{\sqrt{2}} \begin{bmatrix} 1 & 1 \\ 1 & -1 \end{bmatrix} . \tag{2.1}$$

The modal progagation is determined using

$$\gamma_m^2 = T^{-1}(j\omega)^2 CLT = (j\omega)^2 \begin{bmatrix} (c_s - c_m)(l_s + l_m) & 0 \\ 0 & (c_s + c_m)(l_s - l_m) \end{bmatrix} \tag{2.2}$$

Then, the propagation matrix is given as

$$\gamma_m = j\omega \begin{bmatrix} \sqrt{(c_s - c_m)(l_s + l_m)} & 0 \\ 0 & \sqrt{(c_s + c_m)(l_s - l_m)} \end{bmatrix} \tag{2.3}$$

or more simply, let $\beta_m = 1.58 \cdot 10^{-13}$ rad/mil.

Define a characteristic impedance as in C. R. Paul MTL:

$$Z_c = (j\omega)^{-1} C^{-1} T \gamma_m T^{-1} \ . \tag{2.4}$$

Then, the solution to the MTL equations can be expressed as

$$V(z) = Z_c T \left(e^{-j\beta_m z} I_m^+ + e^{j\beta_m z} I_m^- \right) \tag{2.5}$$

$$I(z) = T \left(e^{-j\beta_m z} I_m^+ - e^{j\beta_m z} I_m^- \right) \tag{2.6}$$

where I_m^+ are I_m^- are the coefficient vectors for the forward and reverse modal currents, respectively.

The coupler works on a $\lambda/4$ effect. This effect is similar to a quarter-wave transformer implementation. However, the lines are terminated in open and short circuit combinations. Additionally, the multiconductor geometry allows for more than one propagating mode: an even mode and an odd mode. These boundary conditions and the propagating modes are further analyzed to determine the input impedance required to match the load impedance.

Let $\beta_m z \to \theta$ so that $\theta = 0$ represents the near end of the lines, and $\theta = \pi/2$ represents the far end. The boundary at the near side is

$$\begin{aligned} 0 &= -V_s + Z_s I(0) + V(0) \\ &= -V_s + Z_s T (I_m^+ - I_m^-) + Z_c T (I_m^+ + I_m^-) \\ &= -V_s + (Z_s + Z_c) T I_m^+ + (-Z_s + Z_c) T I_m^- \ . \end{aligned} \tag{2.7}$$

The source impedance is given by

$$\begin{bmatrix} Z_{in} & 0 \\ 0 & Z_{out} \end{bmatrix} \ , \tag{2.8}$$

where Z_{in} is the source impedance, and Z_{out} is the load impedance. The far side boundary conditions are mixed. Line 1 is shorted. So,

$$\begin{aligned} 0 = V_1(\theta = \pi/2) &= -j \begin{bmatrix} Z_{c11} & Z_{c12} \end{bmatrix} T (I_m^+ - I_m^-) \\ &= \frac{-j}{\sqrt{2}} \begin{bmatrix} Z_{even} & Z_{odd} \end{bmatrix} (I_m^+ - I_m^-) \end{aligned} \ , \tag{2.9}$$

where $Z_{even} = Z_{c11} + Z_{c12}$ and $Z_{odd} = Z_{c11} - Z_{c12}$. The boundary conditions can be combined into a matrix equation

$$\begin{bmatrix} Z_{in}^s + Z_{even} & Z_{in}^s + Z_{odd} & -Z_{in}^s + Z_{even} & -Z_{in}^s + Z_{odd} \\ Z_{out} + Z_{even} & -Z_{out} - Z_{odd} & -Z_{out} + Z_{even} & Z_{out} - Z_{odd} \\ Z_{even} & Z_{odd} & -Z_{even} & -Z_{odd} \\ 1 & -1 & 1 & -1 \end{bmatrix} \begin{bmatrix} I_m^+ \\ I_m^- \end{bmatrix} = \begin{bmatrix} \sqrt{2}V_s \\ 0 \\ 0 \\ 0 \end{bmatrix} \tag{2.10}$$

After solving for I_m^+ and I_m^- the input impedance can be found from

$$Z_{in}(z=0) = \frac{V_1(z=0)}{I_1(z=0)} \,, \tag{2.11}$$

which can be found using (2.5) and (2.6). The input impedance calculation can be used get a load profile. The approximate relation is

$$Z_{in}(z=0) \approx 2Z_{load} \,. \tag{2.12}$$

When two roughly 50-Ω loads are connected to the input in parallel with the coupled sections, the input impedance is also approximately 50 Ω.

The Marchand balun design uses line terminations opposite to those described above. The input line of the coupled pair is open circuited while the ouput line is shorted. Analysis like that above leads to the approximate relation that $Z_{in} \approx Z_{load}/2$. This combination is impractical in parallel, but it suits the series layout of the Marchand balun.

2.2.2. Line Width Selection and Layout Considerations. The analytical models presented in the last section give a good first approximation to this design. However, real geometries and transmission lines will not have the same ideal behavior. For a more accurate perspective, transmission line models with some parasitics are used. These transmission line models have been developed in Agilent ADS in steps working from the coupled lines outward to the ports.

As with the analysis of the previous splitter, full-wave models are used for the port geometries. These models are the similar to those shown in Figure 2.6. The results of the parametric studies in Section 2.1.1 have been used to choose appropriate antipad sizes reduce reflections from the port feeds. With the new coupled line configuration presented in the last section, the transmission lines can be made very close to 50 Ω . The line impedance is varied slightly to match the effects of the input and output ports.

The Thevenin impedance seen looking from the coupled lines towards the splitter is 49 Ω at the center of the band, 2.1 GHz. Figure 2.22 shows the schematic representation for the coupled lines and their terminations. This simulation uses terminations with parasitic models rather than the ideal boundary conditions in Section 2.2.1. A parametric simulation steps the inductance associated with the shorting via, and Figure 2.23 shows equivalent load impedances that match the input as simulated previously.

The output paths with port models included are simulated in SPICE, and the quarter-wave transformer impedance needed to match the input calculated at band center. The results are shown in Figure 2.24.

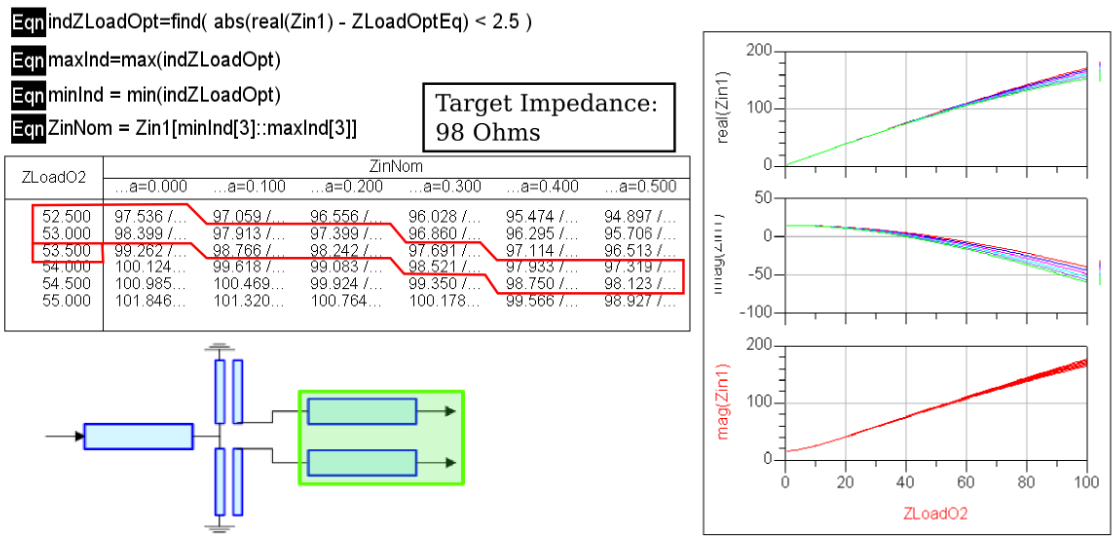

Figure 2.23 Load and via inductance sweeps for tuning the input impedance

2.2.3. Splitter Layout. With all of the line widths defined such that the match at band center is almost perfect, the complete board model can be synthesized as shown in schematic representation, Figure 2.25. To maintain as much symmetry as possible at the output ports, the output trace length is kept as equal as is possible. To do so requires shifting the coupling section. Care must be taken not to route output traces too close to the coupling section, which could lead to unintentional coupling that may increase the output imbalance or reduce the amount of signal reaching the

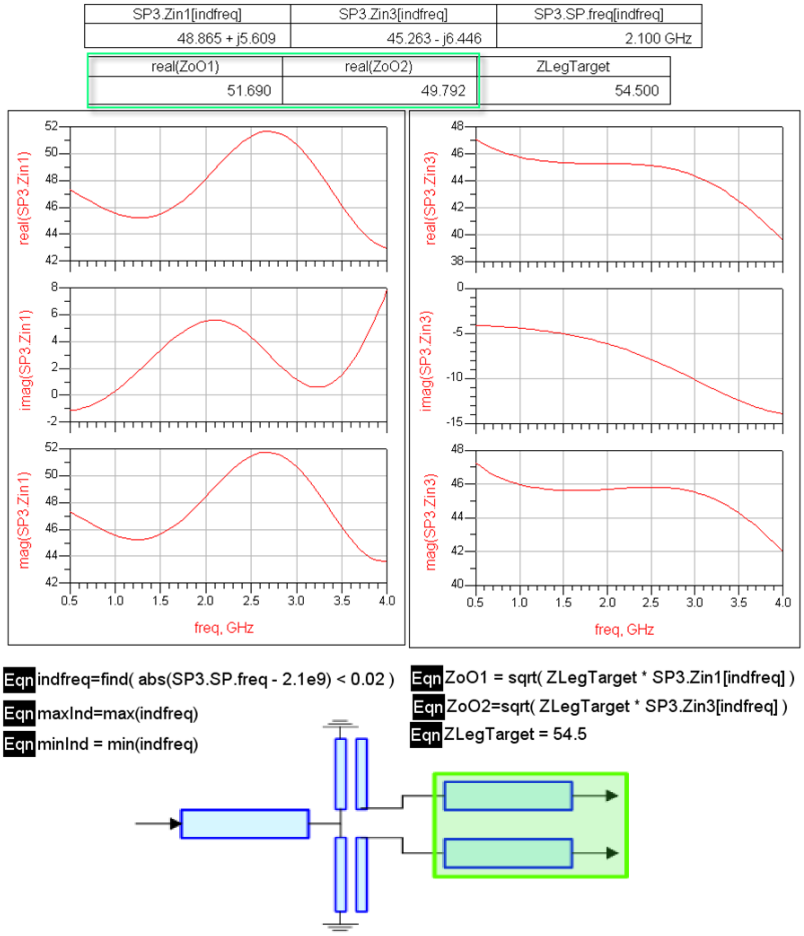

Figure 2.24 The impedance looking from the splitter into the outputs and the matching $\lambda/4$-transformer impedance, denoted by the green box

outputs. This practice also limits the amount of parasitic analysis required to validate the model. The layout of the splitter for an example antenna is shown in Figure 2.26.

The schematic representation shown in Figure 2.25 uses port models as was the case in the system analysis of the previous splitter. The schematic also includes a transmission-line representation of the coupled-line geometry. Additionally, a full-wave model for the coupled-line geometry was generated as shown in Figure 2.27. The schematic representation of this model is shown in Figure 2.28. Both system models were simulated and compared with measured results in Figures 2.29 to 2.33.

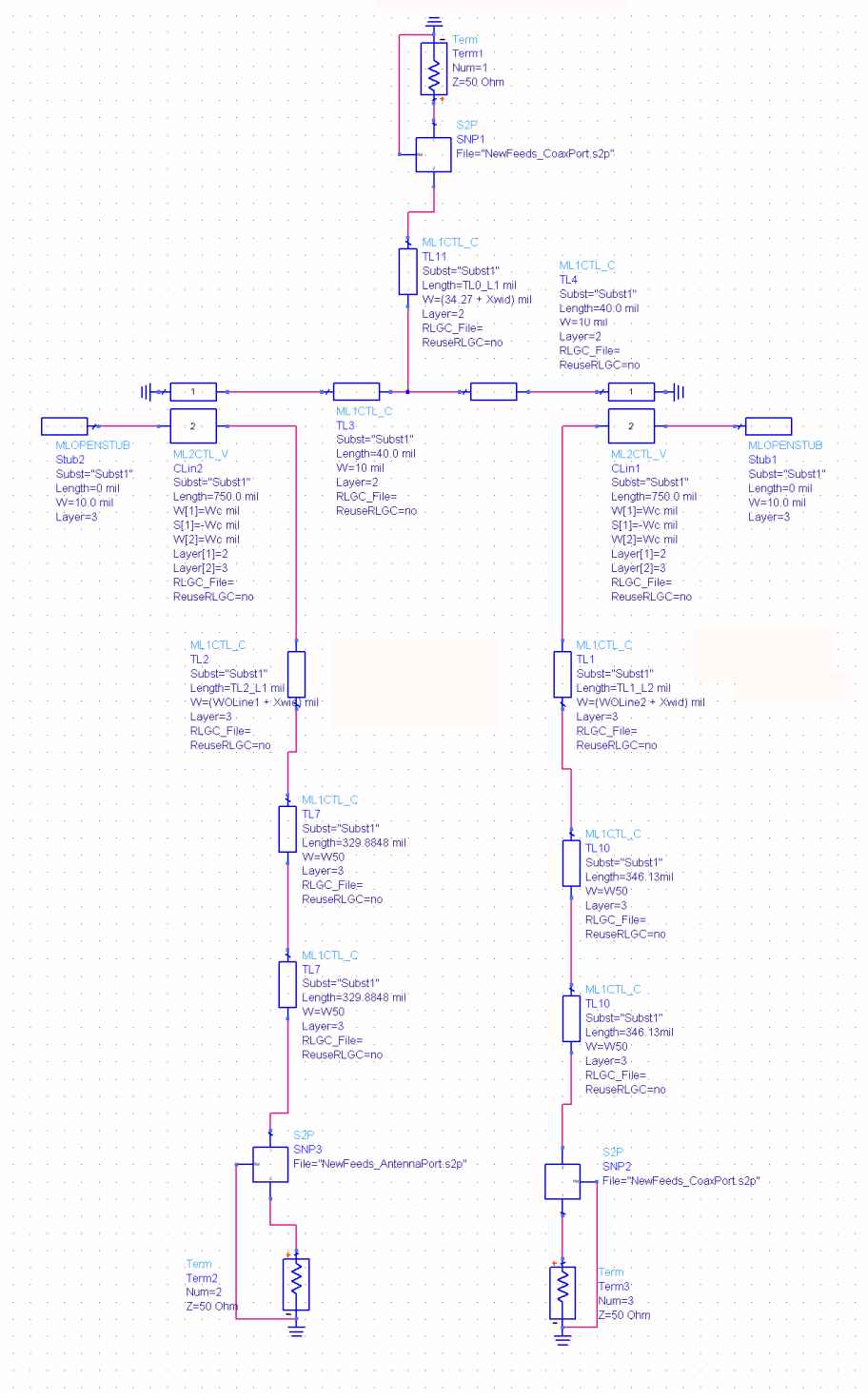

Figure 2.25 Final schematic representation of the redesigned splitter system

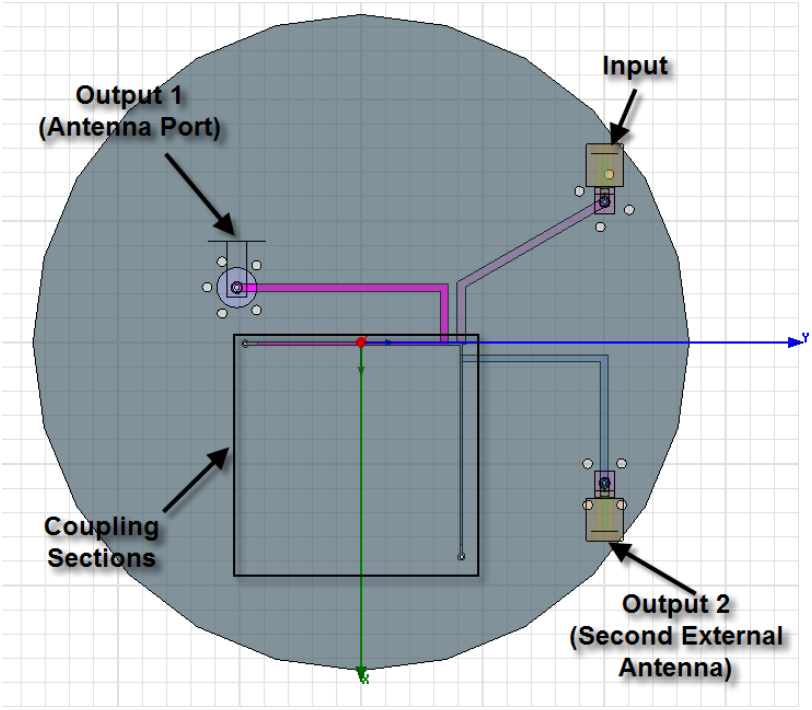

(a) Splitter layout

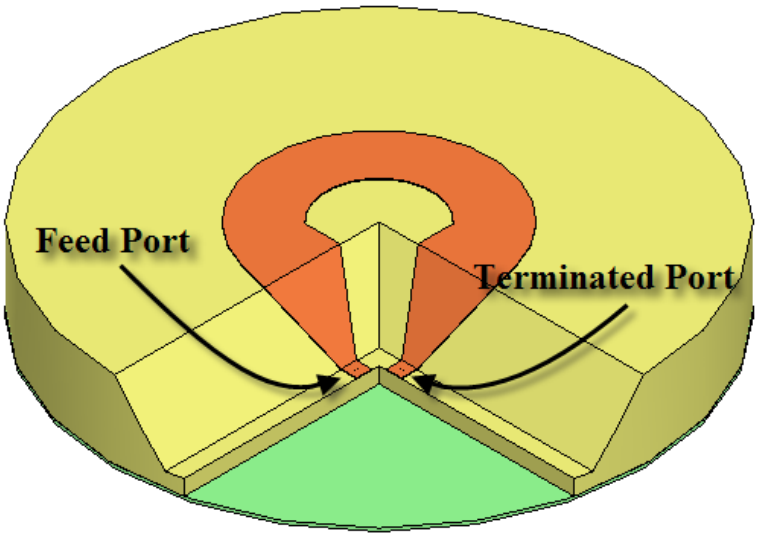

(b) ANSERLIN antenna

Figure 2.26 Splitter layout for an ANSERLIN antenna

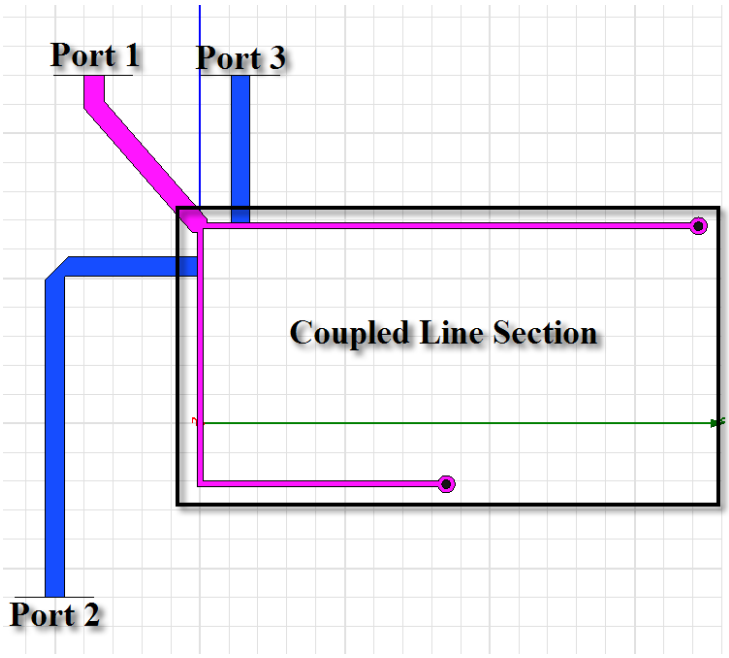

Figure 2.27 Reduced full-wave representation of the revised splitter

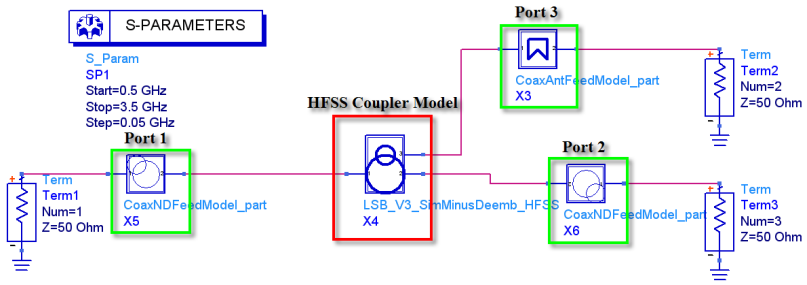

Figure 2.28 The revised splitter including HFSS models of the new port geometries and a separate HFSS model of the splitter

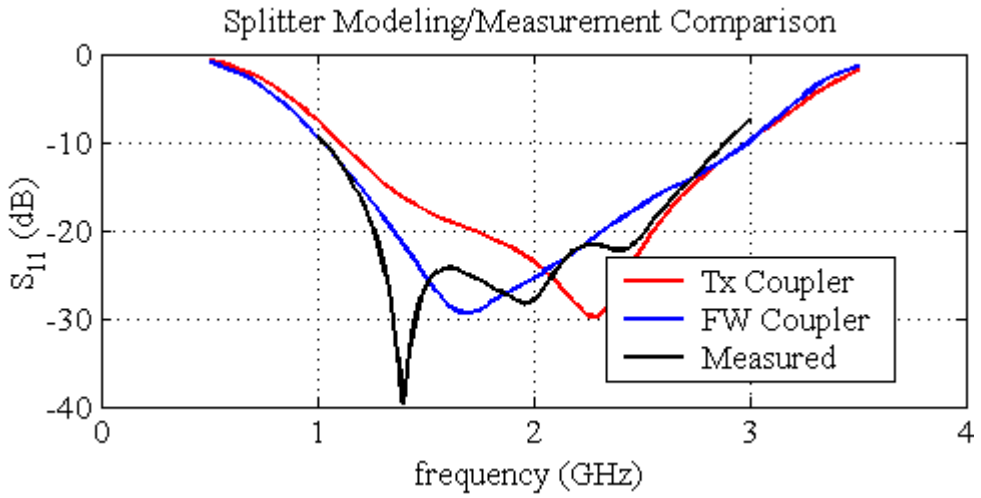

Figure 2.29 Revised splitter modeling and measurement comparison (S_{11})

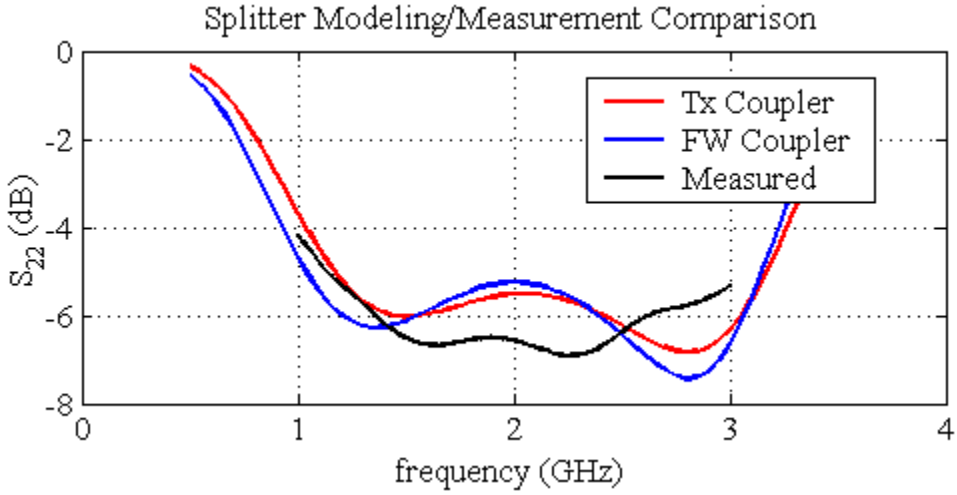

Figure 2.30 Revised splitter modeling and measurement comparison (S_{22})

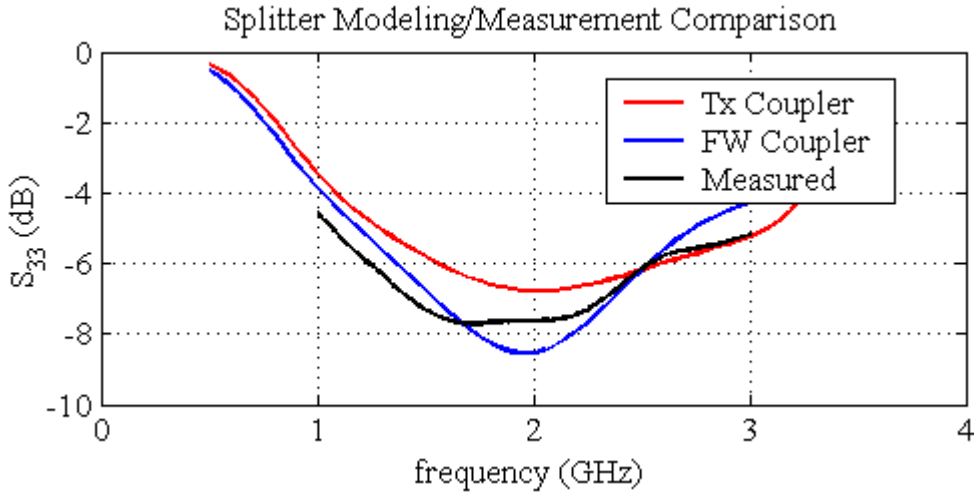

Figure 2.31 Revised splitter modeling and measurement comparison (S_{33})

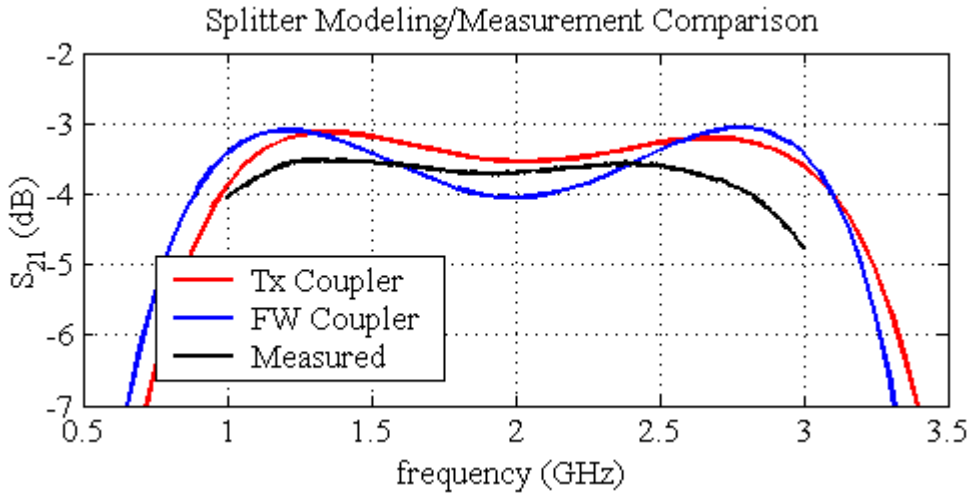

Figure 2.32 Revised splitter modeling and measurement comparison (S_{21})

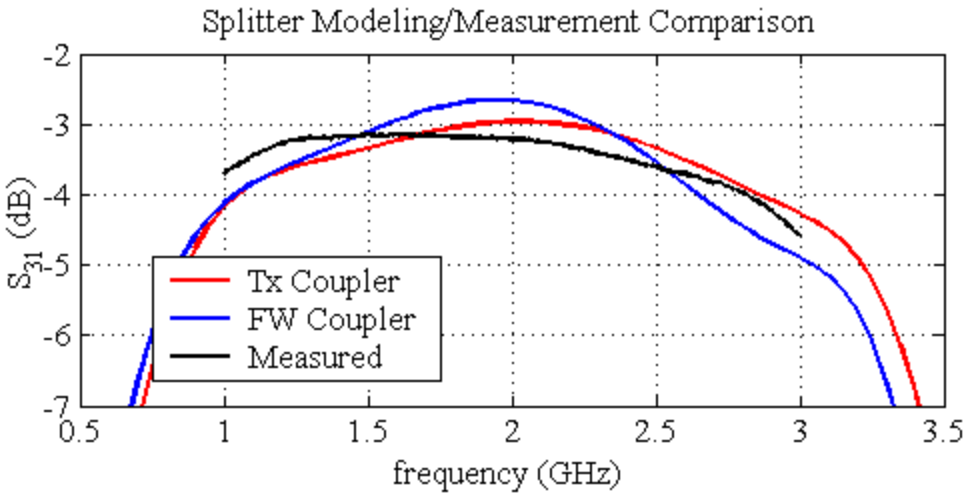

Figure 2.33 Revised splitter modeling and measurement comparison (S_{31})

2.3. SUMMARY AND CONCLUSIONS

An RF splitter for a two-antenna system has been shown in two configurations. After building an initial version of the splitter, an alternate configuration for the broad-side coupled lines was found to be a preferrable option. The new design can be built to match 50-Ω systems without extra matching circuits. In addition to the inherent difficulties of working with the first splitter configuration, the port geometries negatively affected both the return loss and the output balance of the splitter. A combination of full-wave models and SPICE models were used to build complete system models of the splitter. The SPICE models were derived from full-wave models of the port geometries to identify the sensitive design areas in the ports and find the best solution for the redesign. For the redesign, system models were again developed to predict the behavior of the new splitter design. After construction these results were compared with the measured data.

For system models, full-wave methods based on Maxwell's equations are to be preferred when the situation allows. However, most systems are far too complicated to model in one simulation. If special care is taken to match boundary conditions between models, even vastly different modeling methods may be combined to achieve full-system models.

3. DERIVATION OF THE PEEC METHOD

Many previous papers have described the basic derivation of the PEEC method [25–28]. However, these derivations only touch on particular results and lack many of the details. In addition, constant scaling factors for the nonorthogonal PEEC formulation are omitted. The missing factors are misleading and if not noticed lead to solutions with somewhat correct behavior but completely inaccurate results. The following section includes the specifics of these scaling factors with the generalization of an unspecified Green's function.

3.1. NONORTHOGONAL PEEC FORMULATION FOR A GENERAL GREEN'S FUNCTION

The quasi-static form of the free-space Green's function, given by

$$G_s(\vec{r},\vec{r}') = \frac{1}{4\pi|\vec{r}-\vec{r}'|}\ , \tag{3.1}$$

is often used as the kernel for the vector magnetic potential and the scalar electric potential. For most situations this choice is adequate for accurate results. However, the phase relations between PEEC cells are lost. In the time domain the effect of the phase term is incorporated as a time delay, and in the frequency domain center to center phase approximations are used to approximate the phase information for a pair of cells. For many of the results presented elsewhere in this work the dynamic form of the free-space Green's function is used as shown in (3.2).

$$G(\vec{r},\vec{r}') = \frac{e^{-jk|\vec{r}-\vec{r}'|}}{4\pi|\vec{r}-\vec{r}'|} \tag{3.2}$$

It is not necessary to include the form of the Green's function for the majority of the partial parameter derivation. Therefore, it is left unspecified in this section.

The PEEC derivation begins with the electric field integral equation (EFIE), expressed in the frequency domain as

$$\vec{E}(\vec{r}) = \vec{E}^i(\vec{r}) - j\omega\vec{A}(\vec{r}) - \nabla\phi(\vec{r}) \tag{3.3}$$

This brief derivation will consider only the conductors of the models and will also exclude the incident fields. Therefore, let

$$\vec{E}(\vec{r}) = \frac{\vec{J}(\vec{r})}{\sigma} \text{ and } \vec{E}^i(\vec{r}) = 0,$$

and (3.3) becomes

$$\frac{\vec{J}(\vec{r})}{\sigma} + j\omega\vec{A}(\vec{r}) + \nabla\phi(\vec{r}) = 0 \tag{3.4}$$

The geometry is discretized into general hexahedra, which may be described in terms of a local coordinate system for each hexahedron given by

$$\vec{r}(a,b,c) = \frac{1}{8}\sum_{k=1}^{8}(1+a_k a)(1+b_k b)(1+c_k c)\vec{r}_k^m. \tag{3.5}$$

where $\vec{r}_k^m$ for $k \in \{1,...,8\}$ are the corners of the hexahedron. Let the volume enclosed by the mth hexahedron as V_m. Then, $\vec{r} \in V_m \ \forall \ a,b,c \in [-1,1]$. This particular coordinate system and nonorthogonal formulation was discussed in [26]. The EFIE expression in (3.4) is enforced in a weighted integral sense by

$$\int_{V_m} \vec{w}_m \cdot \left[\frac{\vec{J}(\vec{r})}{\sigma} + j\omega A(\vec{r}) + \nabla\phi(\vec{r})\right] dV(\vec{r}) = 0 \ \ \forall \ m \tag{3.6}$$

where $\vec{w}_m$ is a weight function described by

$$\vec{w}_m(\vec{r}) = \Pi_m(\vec{r}) \left(\frac{\frac{\partial\vec{r}}{\partial a_m}}{4\mathcal{J}_m}\right) \ . \tag{3.7}$$

The weight function is composed of $\Pi_m(\vec{r})$, a pulse function that is 1 for $\vec{r} \in V_m$ and 0 otherwise; the directional vector, $\frac{\partial\vec{r}}{\partial a_m}$; and the Jacobian, given by

$$\mathcal{J}_m = \left|\frac{\partial\vec{r}}{\partial a_m} \cdot \left(\frac{\partial\vec{r}}{\partial b_m} \times \frac{\partial\vec{r}}{\partial c_m}\right)\right| \ . \tag{3.8}$$

The current density is discretized by

$$\vec{J}(\vec{r}) = \sum_n I_n \vec{w}_n(\vec{r}) \ . \tag{3.9}$$

The basis function for the current discretization and the weight function in (3.6) are the same, making this Galerkin approach.

Consider each term from (3.6) separately. The potential term becomes

$$\begin{aligned}\int_{V_m} \vec{w}_m(\vec{r}) \cdot \nabla\phi(\vec{r}) dV(\vec{r}) &= \int_{-1}^{1}\int_{-1}^{1}\int_{-1}^{1} \left(\frac{\frac{\partial \vec{r}}{\partial a_m}}{4\mathcal{J}_m}\right) \cdot \nabla\phi(\vec{r}(a,b,c))\mathcal{J}_m dadbdc \\ &= 0.25\int_{-1}^{1}\int_{-1}^{1}\int_{-1}^{1} \frac{\partial \vec{r}}{\partial a_m} \cdot \nabla\phi(\vec{r}(a,b,c)) dadbdc \ .\end{aligned} \tag{3.10}$$

The integrand can be expanded in terms of partial derivatives. The result is a chain rule expression that simplifies,

$$\frac{\partial \vec{r}}{\partial a_m} \cdot \nabla\phi(\vec{r}(a,b,c)) = \frac{\partial \phi}{\partial x}\frac{\partial x}{\partial a_m} + \frac{\partial \phi}{\partial y}\frac{\partial y}{\partial a_m} + \frac{\partial \phi}{\partial z}\frac{\partial z}{\partial a_m} = \frac{\partial \phi}{\partial a_m} \ . \tag{3.11}$$

Then, the integral with respect to a can be evaluated as

$$\begin{aligned}0.25\int_{-1}^{1}\int_{-1}^{1}\int_{-1}^{1} \frac{\partial \phi}{\partial a_m} dadbdc& \\ =& 0.25\int_{-1}^{1}\int_{-1}^{1} [\phi(\vec{r}(1,b,c)) - \phi(\vec{r}(-1,b,c))] dbdc \\ =& \overline{\phi(a=1)} - \overline{\phi(a=-1)} \ .\end{aligned} \tag{3.12}$$

The mean voltage is calculated over the end faces of the current cell. While this is technically correct, the result to the end formulation would be an asymmetric potential coefficients matrix. The target and source regions would not be equivalent for all cases. For example, there is another current cell that extends orthogonally from charge cell m. Since both cell directions must be considered equally in the formulation, a volume average is taken. This decision leads to an offset gridding of the current and charge cells.

The vector electric potential term leads to the partial inductance expression,

$$\begin{aligned}&\int_{V_m} \vec{w}_m \cdot \left(j\omega\vec{A}(\vec{r})\right) dV(\vec{r}) = j\omega \int_{V_m} \vec{w}_m \cdot \int_V G(\vec{r},\vec{r}')\mu\vec{J}(\vec{r}') dV(\vec{r}') dV(\vec{r}) \\ &= \left\{ j\omega \sum_{n=1}^{M} \frac{I_n}{16} \int_{-1}^{1}\int_{-1}^{1}\int_{-1}^{1}\int_{-1}^{1}\int_{-1}^{1}\int_{-1}^{1} \left(\frac{\partial \vec{r}}{\partial a} \cdot \frac{\partial \vec{r}}{\partial a'}\right) \right. \\ &\qquad \left. \times G(\vec{r},\vec{r}') da' db' dc' dadbdc \right\} = j\omega \sum_{n=1}^{M} I_n L_{mn} \ .\end{aligned} \tag{3.13}$$

Therefore, the partial inductance is

$$L_{mn} = \frac{1}{16}\int_{-1}^{1}\int_{-1}^{1}\int_{-1}^{1}\int_{-1}^{1}\int_{-1}^{1}\int_{-1}^{1}\left(\frac{\partial\vec{r}}{\partial a}\cdot\frac{\partial\vec{r'}}{\partial a'}\right) \times G(\vec{r},\vec{r'})da'db'dc'dadbdc \tag{3.14}$$

Similarly, the leading current term leads to a resistance. The result is given by

$$\int_{V_m}\vec{w}_m\cdot\left(\frac{1}{\sigma}\vec{J}(\vec{r})\right)dV(\vec{r}) = I_m\frac{1}{16\,\sigma}\int_{-1}^{1}\int_{-1}^{1}\int_{-1}^{1}\frac{\left|\frac{\partial\vec{r}}{\partial a_m}\right|^2}{\mathcal{J}_m}dadbdc = I_m R_m\ . \tag{3.15}$$

The partial potential coefficient derivation is shown in Section 3.2.2 to demonstrate the idea of subgridding for partial parameter accuracy.

3.2. FAST ELEMENT EVALUATION TECHNIQUES

Both the orthogonal and nonorthogonal formulas for partial inductance and potential coefficients produce dense matrices, requiring $N(N+1)/2$ calculations per matrix, assuming symmetry. Additionally, the diagonal elements of both matrices require integration of singular integrands. This section shows the development of integration formulas to decrease the calculation time while providing accurate answers for even the diagonal elements.

3.2.1. Adaptive Quadrature Order Selection. The proximity of cells, whether potential or current, influences the quadrature order required to accurately calculate the partial parameters. Using a high-order numerical quadrature on parameter calculations may be sufficient, but it is not always necessary. Nearest neighbor cells require significantly more quadrature points for accurate calculations than cells separated by significant distance. An adaptive quadrature order selection is applied to select the quadrature order. This procedure is similar to using a fast multipole method (FMM) [1].

The cell interactions are divided into a fixed number of groups, with each group using a predefined quadrature order. The group is found for each numerical integration based on the ratio of the mean length in the integration direction to the center-to-center cell distance. This relation is illustrated in Figure 3.1. In general, the quadrature orders for an element determined are the same for all three dimensions of the element. But for a PCB, cell thickness is often much thinner than the

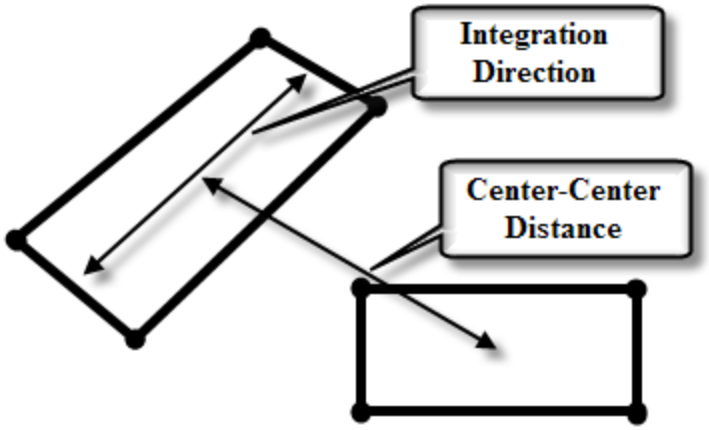

Figure 3.1 Relative cell dimensions used for quadrature order selection

length and width. Thus, a low-order quadrature is sufficient for the integration of the thickness of the PCB.

3.2.2. Subgridding Cells for Convergent, Iterative Calculation of Partial Element Integrals. Subgridding schemes that do not add unknowns have been considered before for PEEC [7]. In this paper subgridding is used iteratively to ensure convergence of the partial coefficients being evaluated. It is common to use Gaussian integration to evaluate integrals such as expressed in Section 3.1. Accurately calculating the partial coefficient integrations may require a high order integration. Iterations of increasingly higher order integrations may be used to converge to a solution. Alternatively, iterative subgridding may be used to perform the same task.

Most of the integrands discussed so far have a $1/R$ dependence. For simplicity, consider

$$f(x) = \int_a^b \frac{1}{x} dx \ . \tag{3.16}$$

It has been observed that Gaussian integration of (3.16) can be calculated accurately with low order integrations provided that $\log_{10}(b/a) \leq 1$. This rule is not strict. Table 3.1 shows the error for different quadrature orders and values of $\log_{10}(b/a)$. The left column is meant to represent $\log_{10}(R_{max}/R_{min})$. This data can serve as a criterion for selecting integration degrees.

The final expression for the potential coefficient illustrates the concept of the subgridding scheme. The coefficients are found by discretizing the charge on a potential cell. The charge is limited to the surfaces of the conductors. Therefore, let the

Table 3.1 The integral $\int_a^b 1/x\ dx$ calculated with different degree Gauss, Bond, and Gauss-Patterson quadrature weights and roots

$\log_{10}(b/a)$	Gauss Degree	Gauss Err (%)	Bond Err (%)	Δ G-B (%)	Pat Base 2 Err (%)
0.25	2	0.059	2.7	2.7	0.059
	3	0.0012	2.1	2.1	
	4	0.000026	0.030	0.030	
	5	0.00000052	0.044	0.044	0.0000075
	6	0.000000011	0.00043	0.00043	
0.5	2	0.83	9.8	9.4	0.83
	3	0.068	7.7	7.5	
	4	0.0054	0.39	0.40	
	5	0.00043	0.62	0.62	0.0013
	6	0.000034	0.022	0.022	
1	4	0.68	2.6	3.2	
	5	0.19	6.1	6.1	0.028
	6	0.051	0.67	0.62	
	7	0.014	1.6	1.6	
	8	0.0038	0.12	0.13	
	9	0.0010	0.44	0.44	
2	4	17.3	10.0	8.4	
	5	11.9	29.3	22.0	8.3
	6	8.1	11.6	3.8	
	11	1.2	4.5	5.6	0.16
	12	0.81	0.23	0.58	
	18	0.076	0.20	0.12	
3	4	40.3	34.4	9.3	
	5	34.7	49.7	26.0	30.7
	6	30.3	33.5	4.8	
	11	16.1	6.7	10.6	9.6
	23	3.9	0.73	4.7	0.75
	35	0.90	1.3	2.2	

charge be discretized as

$$q(\vec{r}) = \sum_{j=1}^{P} \Pi_j(\vec{r}) \frac{Q_j}{S_j} \tag{3.17}$$

where S_j is the total exterior surface area of the potential node, and P is the total number of charges in the model. Take the weighted average of the potential over the surface of potential cell i. Assume that the ith cell has N_i exterior sides, and the

integration is broken up over the sides.

$$\begin{aligned}\Phi_i &= \int_{S_i} \frac{1}{S_i}\phi(\vec{r})dS(\vec{r}) = \frac{1}{S_i}\sum_{m=1}^{N_i}\int_{S_{im}} \phi(\vec{r})dS(\vec{r}) \\ &= \sum_{j=1}^{P} Q_j \frac{1}{S_i S_j \varepsilon}\sum_{m=1}^{N_{ij}}\sum_{n=1}^{N_{ji}}\int_{-1}^{1}\int_{-1}^{1}\int_{-1}^{1}\int_{-1}^{1} \\ &\quad G(\vec{r},\vec{r}')\left[\frac{\partial\vec{r}'}{\partial a'}\times\frac{\partial\vec{r}'}{\partial b'}\right]da'db'\times\left[\frac{\partial\vec{r}}{\partial a}\times\frac{\partial\vec{r}}{\partial b}\right]dadb\end{aligned} \tag{3.18}$$

Then, the partial potential coefficients are then given by

$$\begin{aligned}p_{ij} &= \frac{1}{S_i S_j \varepsilon}\sum_{m=1}^{N_{ij}}\sum_{n=1}^{N_{ji}}\int_{-1}^{1}\int_{-1}^{1}\int_{-1}^{1}\int_{-1}^{1} \\ &\quad G(\vec{r},\vec{r}')\left[\frac{\partial\vec{r}'}{\partial a'}\times\frac{\partial\vec{r}'}{\partial b'}\right]da'db'\times\left[\frac{\partial\vec{r}}{\partial a}\times\frac{\partial\vec{r}}{\partial b}\right]dadb\end{aligned} \tag{3.19}$$

In the above expressions $N_i \rightarrow N_{ij}$ and $N_j \rightarrow N_{ji}$ to indicate that the number of plates used in the calculation may vary depending on the other cell in the calculation. In this formulation the coefficient represents the whole potential cell rather than the individual surface plates. Since there is already a sum over the individual plates, the equation is essentially unchanged when the integration is further divided over more plates to increase the integration accuracy. A convergent calculation of the partial coefficients is achieved by iteratively subdividing the original regions along their longest dimension and recalculating the coefficient.

3.2.3. Fast Evaluation of the Partial Potentials. An analytical solution for the surface integral can be employed to decrease calculation time for the evaluation of the coefficients of potential [18]. In [20] a general solution to

$$\int_S \frac{d\xi d\eta}{|\vec{r}-\vec{r}'|}$$

was developed for quadrilaterals in the xy plane with vertices (ξ_n, η_n), given in clockwise order, as shown in Figure 3.2. The solution is given as

$$\Psi = \int_S \frac{d\xi d\eta}{|\vec{r}-\vec{r}'|} = \sum_{n=1}^{4}\left\{\begin{array}{c}\left[(x-\xi_n)\dfrac{\delta\eta_n}{s_n} - (y-\eta_n)\dfrac{\delta\xi_n}{s_n}\right] \\ \times\log\left(\dfrac{R_n+R_{n+1}+s_n}{R_n+R_{n+1}-s_n}\right)\end{array}\right\} - z\Phi\ , \tag{3.20}$$

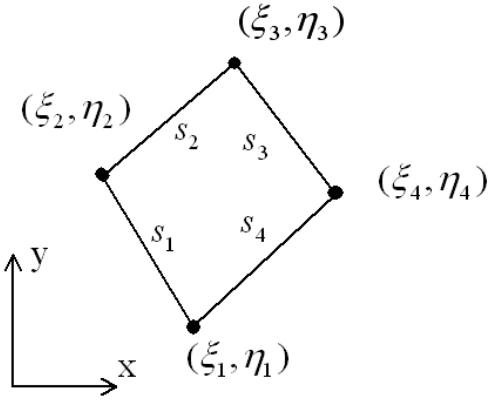

Figure 3.2 Definition of the quadrilateral panel

and

$$\Phi = \sum_{n=1}^{4} \left\{ \tan^{-1} \left[\frac{\delta\eta_n[(x-\xi_n)^2 + z^2] - \delta\xi_n(x-\xi_n)(y-\eta_n)}{R_n z \delta\xi_n} \right] - \int \tan \left[\frac{\delta\eta_n[(x-\xi_{n+1})^2 + z^2] - \delta\xi_n(x-\xi_{n+1})(y-\eta_{n+1})}{R_{n+1} z \delta\xi_n} \right] \right\} , \tag{3.21}$$

where $\delta\xi_n = \xi_{n+1} - \xi_n$, $\delta\eta_n = \eta_{n+1} - \eta_n$, $R_n = \sqrt{(x-\xi_n)^2 + (y-\eta_n)^2 + z^2}$, and $s_n = \sqrt{(\delta\xi_n)^2 + (\delta\eta_n)^2}$.

The singularity in the integrand of the self potential coefficient occurs when the observeration point, $\vec{r}$, and the source point, $\vec{r}\,'$, are equal. Using (3.20) and (3.21), the integration domain is changed from the quadrilateral to the boundary of the quadrilateral, and the abscissae for Gaussian integration are all in the interior of the integration domain. Therefore, the problem of the singularity is avoided by using the above formula for one of the surface integrations and a Gaussian quadrature for the other surface integration.

In general, the quadrilateral will require rotating and shifting to position it in the xy plane. This can be accomplished using an Euler rotation of the form

$$R_Q = R_Q(\phi, \theta, \psi) = \begin{bmatrix} \cos\phi & \sin\phi & 0 \\ -\sin\phi & \cos\phi & 0 \\ 0 & 0 & 1 \end{bmatrix} \begin{bmatrix} 1 & 0 & 0 \\ 0 & \cos\theta & \sin\theta \\ 0 & -\sin\theta & \cos\theta \end{bmatrix} \begin{bmatrix} \cos\psi & \sin\psi & 0 \\ -\sin\psi & \cos\psi & 0 \\ 0 & 0 & 1 \end{bmatrix} , \tag{3.22}$$

illustrated in Figure 3.3.

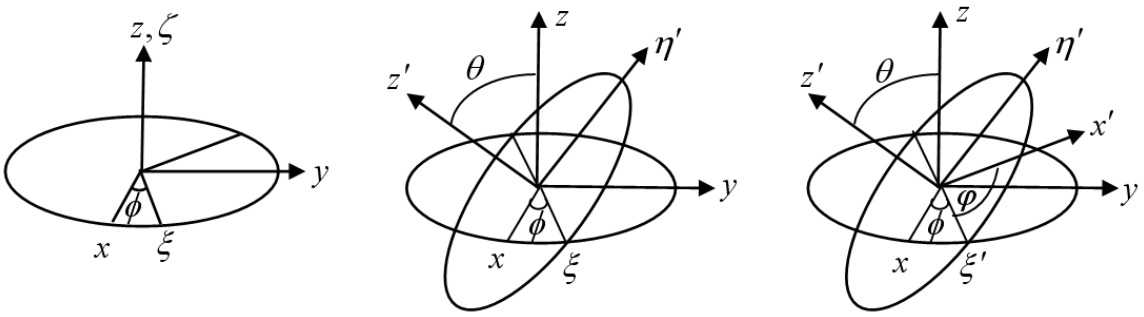

Figure 3.3 The Euler angle rotations to rotate the quadrilateral parallel to the xy plane

The potential coefficients are found starting from

$$P_{ij} = \int_{S_i} s_i(\vec{r}) \int_{S_j} \frac{G(\vec{r},\vec{r}\,')s_j(\vec{r}\,')}{\varepsilon_o} dS(\vec{r}\,')dS(\vec{r}) \ , \tag{3.23}$$

a more general form than used in Section 3.2.2. Let s_i use the basis function

$$s_i(\vec{r}) = \Pi_i(\vec{r}) \frac{1}{\left| \frac{\partial \vec{r}}{\partial a_i} \times \frac{\partial \vec{r}}{\partial b_i} \right|} \ , \tag{3.24}$$

let s_j using the basis used for (3.17), and substitute (3.1) for the Green's function. Then, the fast integration form of the potential coefficients is given by

$$P_{ij} = \frac{1}{4\pi\varepsilon_o A_j} \int_0^1 \int_0^1 \left[\int_{S_j} \frac{1}{|\vec{r} - \vec{r}\,'|} dS(\vec{r}\,') \right] da_i db_i \ . \tag{3.25}$$

3.2.4. Fast Evaluation for the Partial Inductances. Referring to (3.14) for zero-thickness conductors, the volume integral becomes a surface integral which is nearly identical to the form of the previous calculation. Thus, the same approach used on the potential coefficients can be adapted to use on the inductance calculation. As with the potential cofficient calculation, the goal in this section is to derive an integration formula to decrease the number of numerical integrations and also handle the singularity in the self inductance with a lower order quadrature. The derivation that follows here is nearly identical with that shown in [11], which used an approach similar to that in [2].

Start again with a general form of the partial inductance expression,

$$L_{mn} = \int_{V_m} \vec{w}_m(\vec{r}) \cdot \int_{V_n} G(\vec{r},\vec{r}\,')\mu_o \vec{w}_m(\vec{r}\,')\; dV(\vec{r}\,')dV(\vec{r}) \; . \tag{3.26}$$

For $\vec{w}_n$, use the basis function

$$\vec{w}_n(\vec{r}) = \Pi_n(\vec{r})\frac{\hat{a}_n}{A_n} \; , \tag{3.27}$$

where $\Pi_n(\vec{r})$ is a pulse function supported over cell n, $\hat{a}_n$ is the unit vector in the direction of the current, and A_n is the cross sectional area of the cell. Being constant over the cell, these quantities can be pulled out of the inner volume integral. Then, use (3.7) for $\vec{w}_m$. Approximate $\hat{a}_n$ and A_n by their mean values. Once constant, they can both be pulled from the integrals. Denote the means as $\underline{\hat{a}}_n$ and $\underline{A}_n$. Then, (3.26) can manipulated such that we can apply Gauss's theorem,

$$L_{mn} = \frac{\mu_o \underline{\hat{a}}_n}{4\pi \underline{A}_n} \cdot \int_0^1 \int_0^1 \int_0^1 \frac{\partial r}{\partial a_m} \left[\int_{V_n} \frac{1}{|\vec{r} - \vec{r}\,'|} dV(\vec{r}\,') \right] da_m db_m dc_m \; . \tag{3.28}$$

Utilize the expression $\nabla \cdot \hat{r}/2 = 1/r$, and apply Gauss's theorem such that

$$\begin{aligned} L_{mn} &= \frac{\mu_o \underline{\hat{a}}_n}{4\pi \underline{A}_n} \cdot \int_0^1 \int_0^1 \int_0^1 \frac{\partial r}{\partial a_m} \left[\frac{1}{2} \int_{V_n} \nabla \cdot \frac{(\vec{r}\,' - \vec{r})}{|\vec{r}\,' - \vec{r}|} dV(\vec{r}) \right] da_m db_m dc_m \\ &= \frac{\mu_o \underline{\hat{a}}_n}{4\pi \underline{A}_n} \cdot \int_0^1 \int_0^1 \int_0^1 \frac{\partial r}{\partial a_m} \sum_{k=1}^{6} \left[\frac{1}{2} \int_{S_{nk}} \hat{n}_k \cdot \frac{(\vec{r}\,' - \vec{r})}{|\vec{r}\,' - \vec{r}|} dV(\vec{r}) \right] da_m db_m dc_m \; , \end{aligned} \tag{3.29}$$

where the S_{nk} are the quadrilateral sides of V_n with $\hat{n}_k$ as the outward normals. Note that since S_{nk} is planar,

$$\zeta_k = \hat{n}_k \cdot (\vec{r}\,' - \vec{r}) \tag{3.30}$$

is constant for the source integral. Then,

$$L_{mn} = \frac{\mu_o \underline{\hat{a}}_n}{8\pi \underline{A}_n} \cdot \int_0^1 \int_0^1 \int_0^1 \frac{\partial r}{\partial a_m} \sum_{k=1}^{6} \left[\zeta_k \int_{S_{nk}} \frac{1}{|\vec{r} - \vec{r}\,'|} dV(\vec{r}) \right] da_m db_m dc_m \; , \tag{3.31}$$

and (3.20) can be used to solve the source integral analytically. The formula in (3.31) is valid for self and mutual partial inductances, but is essential for self partial inductances, as it efficiently deals with the singularity in the integrand.

3.3. MATRIX FORMULATION

The original PEEC formulation takes the partial parameters described in the last section and create a SPICE netlist to calculate frequency and time domain results. This section describes a matrix formulation alternative to the netlist. The three matrix equations that make up the matrix solution are

$$(R + j\omega L + \frac{1}{j\omega}{C_e}^{-1})I_L + \Gamma\Phi = 0 \tag{3.32a}$$

$$PQ = \Phi \tag{3.32b}$$

$$-\Gamma^T I_L + j\omega Q = I_T \ . \tag{3.32c}$$

The matrix descriptions are given in Table 3.2. The charges are removed from the solution by inverting P and substituting for Q in the continuity equation yielding the block matrix equation. Let $Z = R + j\omega L + \frac{1}{j\omega}{C_e}^{-1}$. Then, the combined matrix equation is

$$\begin{bmatrix} Z & \Gamma \\ -\Gamma^T & j\omega P^{-1} \end{bmatrix} \begin{bmatrix} I_L \\ \Phi_C \end{bmatrix} = \begin{bmatrix} 0 \\ I_T \end{bmatrix} \ . \tag{3.33}$$

This equation can be further condensed by solving the first row for I_L and substituting it in the second row equation to get

$$\left[\Gamma^T Z^{-1}\Gamma + j\omega P^{-1}\right]\Phi = I_T \ , \tag{3.34}$$

and the impedance matrix for the structure is

$$Z_p = \left[\Gamma^T Z^{-1}\Gamma + j\omega P^{-1}\right]^{-1} \ . \tag{3.35}$$

Note that Z_p is not equivalent to the Z in (3.33).

3.3.1. Controlled Impedance Ports. The solution for the admittance matrix of the system was given in the last section as

$$YV = I_T \tag{3.36}$$

where Y is the admittance matrix from the PEEC discretization, V is a vector of the node voltages, and I_T is a vector of impressed currents on the nodes. The impedance and admittance matrices are well suited for analyzing some models. However, the S-parameter matrix is more commonly used in RF applications. The S-parameter matrix can be found from the impedance and admittance equations in most cases.

Table 3.2 Description of matrix terms for the PEEC formulation

Matrix	Description
R	Resistances
L	Partial Inductances
C_e	Excess Capacitances
P	Partial Potential Coefficients
Γ	Connectivity Matrix
I_L	Inductor Currents
Q	Charges
Φ	Potentials
I_T	External Terminal Currents

However, for nearly open or shorted devices, the calculations may prove inaccurate. This issue is avoided if the S-parameters are calculated directly, which is the topic of this section.

After adding some constraints into the formulation, the S-parameters can be solved directly. The additional equation on the nodes connecting the port is

$$V_p - V_n + Z_o\lambda = V_s \tag{3.37}$$

where V_p and V_n are the positive and negative voltage nodes respectively, λ is the port current directed into the positive node, and V_s is the driving voltage source.

Each port adds one equation to the system of equations. In addition, the equations involving Y must be adjusted to consider the additional current. Define the row vectors e_k for each port k such that

$$\{e_k\}_i = \begin{cases} 1 & i \text{ is the positive node} \\ -1 & i \text{ is the negative node} \\ 0 & \text{otherwise} \end{cases} \tag{3.38}$$

with

$$A = \begin{bmatrix} e_1 \\ e_2 \\ \vdots \end{bmatrix} \tag{3.39}$$

Then, the new matix equation is

$$\begin{bmatrix} Y & A^T \\ A & Z_o I_{Q\times Q} \end{bmatrix} \begin{bmatrix} \Phi \\ \lambda \end{bmatrix} = \begin{bmatrix} I_T \\ V_s \end{bmatrix} \tag{3.40}$$

where Q is the number of ports and I is the identity matrix. Rather than solving the matrix for each port excitation individually, the new matrix is inverted. The form of this matrix can be divided into block matrices, only one of which is needed for the final solution.

$$\begin{bmatrix} \Phi \\ \lambda \end{bmatrix} = \begin{bmatrix} \cdots & \cdots \\ \cdots & Y_T \end{bmatrix} \begin{bmatrix} I_T \\ V_s \end{bmatrix} \tag{3.41}$$

The KVL at port m is

$$V_m = V_m^+ + V_m^- = -Z_o \lambda_m + V_{sm} \tag{3.42}$$

where $\lambda = Y_T V_s$ and V_m^+ and V_m^- are, respectively, the forward and backward traveling voltages seen at port m. Assume that the nth port is excited. The forward voltage wave from port n is given as $V_n^+ = V_{ns}/2$, and

$$\lambda_m = Y_{Tmn} V_{sn} = 2 Y_{Tmn} V_n^+ \ . \tag{3.43}$$

Then, (3.42) becomes

$$V_m^- = -2 Z_o (Y_{Tmn}) V_n^+ + V_m^+ \tag{3.44}$$

However, $V_m^+ = 0$ unless $m = n$. Therefore, $V_m^+ = \delta_{mn} V_n^+$, and the S-parameters can be calculated as

$$S_{mn} = \frac{V_m^-}{V_n^+} = \delta_{mn} - 2 Z_o Y_{Tmn} \ . \tag{3.45}$$

3.3.2. Multinode Controlled Impedance Ports. Using only a single node for each terminal of the model ports is the simplest way to set up a port excitation, however, it invites inaccuracies associated with current spreading from the single node. This section describes the connectivity matrices and matrix algebra required to introduce multinode terminals.

The original port connectivity matrix was called A. This derivation relies on three connectivity matrixes, two of which are derived from the first, called B. The number of rows in B is twice the number of ports, and the number of columns in B

is the same as the number of charge cells. The matrix is defined as

$$B_{mn} = \begin{cases} 1\ , & \text{cell } n \text{ is in port terminal } m \\ 0\ , & \text{otherwise} \end{cases} \tag{3.46}$$

From this matrix C and D are derived. The additional variables Λ (the port currents), V_T (the port terminal voltages), and λ (the nodal port currents) are used in the auxiliary port equations.

C maps the elements of V_T onto potential nodes that are connected to terminals and provides a mapping for the equation that keeps potentials connected to a specific terminal the same.

$$CV_T - D\Phi = 0 \tag{3.47}$$

D maps the PEEC nodes onto the port terminals. It is used additionally to map the terminal nodal currents λ on the PEEC nodes, as in

$$Y\Phi - D^T\lambda = 0 \tag{3.48}$$

and

$$BD^T\lambda - \tilde{I}\Lambda = 0\ . \tag{3.49}$$

$\tilde{\Lambda}$ is defined as

$$\tilde{\Lambda} = \begin{bmatrix} I \\ -I \end{bmatrix}\ , \tag{3.50}$$

where I is an identity matrix the same size as the number or ports.

The last expression introduced enforces the lumped condition between the terminal voltages, the port currents, and the port source voltages. The entries in V_T are ordered such that all of the positive terminal voltages are listed first, and the negative terminal voltages are listed last, and the boundary condition at the port is expressed as

$$Z_p\Lambda + \tilde{I}^T V_T = V_s\ . \tag{3.51}$$

The Z_p is the port impedance matrix. In the most general case, port coupling terms beyond the scope of the PEEC goemetry could be included in this matrix. These port conditions could include coupling between the ports, port extensions through transmission lines, or even connections to other PEEC models.

The solution to these equations for the S parameters is not trivial.

$$D\Phi = (DY^{-1}D^T)\lambda \tag{3.52}$$

$$CV_T = (DY^{-1}D^T)\lambda \tag{3.53}$$

$$\lambda = (DY^{-1}D^T)^{-1}CV_T \tag{3.54}$$

$$BD^T\lambda - \tilde{I}{Z_p}^{-1}\left(V_s - \tilde{I}^T V_T\right) = 0 \tag{3.55}$$

$$BD^T(DY^{-1}D^T)^{-1}CV_T - \tilde{I}{Z_p}^{-1}\left(V_s - \tilde{I}^T V_T\right) = 0 \tag{3.56}$$

$$BD^T(DY^{-1}D^T)^{-1}CV_T + \tilde{I}{Z_p}^{-1}\tilde{I}^T V_T = \tilde{I}{Z_p}^{-1}V_s \tag{3.57}$$

$$V_T = \left[\tilde{I}{Z_p}^{-1}\tilde{I}^T + BD^T(DY^{-1}D^T)^{-1}C\right]^{-1}\tilde{I}{Z_p}^{-1}V_s \tag{3.58}$$

The terminal voltages are then related to the wave voltages by

$$V^+ + V^- = \tilde{I}^T V_T \ , \tag{3.59}$$

and

$$V_s = 2V^+ \ . \tag{3.60}$$

Then,

$$V^+ + V^- = \left\{\tilde{I}^T\left[\tilde{I}{Z_p}^{-1}\tilde{I}^T + BD^T(DY^{-1}D^T)^{-1}C\right]^{-1}\tilde{I}{Z_p}^{-1}\right\}2V^+ \ , \tag{3.61}$$

and

$$V^- = \left\{2\left\{\tilde{I}^T\left[\tilde{I}{Z_p}^{-1}\tilde{I}^T + BD^T(DY^{-1}D^T)^{-1}C\right]^{-1}\tilde{I}{Z_p}^{-1}\right\} - I\right\}V^+ \ . \tag{3.62}$$

The expression for the S-parameters above is useful in that it is a direct expression, using the PEEC parameters. No further post processing is required. However, the number of inversions in the formula make it less efficient than solving the block matrix formulation by Gaussian elimination.

The construction of C and D follows from B. The following is an example of how to construct C given a B matrix of the form

$$B = \frac{\left[\text{Positve Terminals}\right]}{\left[\text{Negative Terminals}\right]} = \left[\begin{array}{cccccccccc} 1 & 0 & 0 & 0 & 1 & 1 & 0 & 0 & 0 & 0 \\ 0 & 1 & 0 & 0 & 0 & 0 & 1 & 0 & 0 & 0 \\ \hline 0 & 0 & 1 & 0 & 0 & 0 & 0 & 1 & 0 & 0 \\ 0 & 0 & 0 & 1 & 0 & 0 & 0 & 0 & 1 & 0 \end{array}\right] \ . \tag{3.63}$$

Then, C can be derived with the Matlab algorithm shown in Figure 3.4, resulting in a matrix of the form

$$C = \begin{bmatrix} 1 & 0 & 0 & 0 \\ 1 & 0 & 0 & 0 \\ 1 & 0 & 0 & 0 \\ 0 & 1 & 0 & 0 \\ 0 & 1 & 0 & 0 \\ 0 & 0 & 1 & 0 \\ 0 & 0 & 1 & 0 \\ 0 & 0 & 0 & 1 \\ 0 & 0 & 0 & 1 \end{bmatrix} . \tag{3.64}$$

```
% Construct the C matrix from B
C = zeros(sum(sum(B)), size(B,1));
nodecounts = sum(B');
ind1 = 1;
for m = 1:size(B,1)
  ind2 = ind1 + nodecounts(m) - 1;
  C((ind1:ind2), m) = 1;
  ind1 = ind2 + 1;
end
```

Figure 3.4 Algorithm for the construction of the C connectivity matrix

The construction of D can be handled with matrix operations in Matlab using the algorithm shown in Figure 3.5. Some experimentation revealed that $C^T = BD^T$, a term in (3.49). This is the only use of B in the formulation. Thus, the formulation can be reduced to using C and D for connectivity alone.

3.4. IMPRESSED FIELDS

In general, the field equation that the PEEC method stems from includes impressed electric fields. These were previously ignored, but are considered in this

```
Construct the D matrix from B
D = zeros(size(C,1), N); % Maps nodes onto port node connections.
[ind1, ind2] = find(B==1);
ind1 = [1:length(ind2)]'; % put each entry on a separate row.
indconverted = ind1 + (ind2-1)*size(D,1);
D(indconverted) = 1;
```

Figure 3.5 Algorithm for the construction of the D connectivity matrix

section. The PEEC problem is first posed as

$$\vec{E}(\vec{r}) = \vec{E}^i - j\omega\vec{A}(\vec{r}) - \nabla\Phi(\vec{r}) \ , \tag{3.65}$$

where the potential field quantities compose the scattered field. Enforce (3.65) in a weighted integral sense as in Section 3.1. The result of integrating the impressed field over a current cell, α, is given by

$$V_\alpha^i = \int_{V_\alpha} \vec{w}_\alpha(\vec{r}) \cdot \vec{E}^i(\vec{r}) dV(\vec{r}) \ . \tag{3.66}$$

The form of the impressed electric field is left general. The matrix equations previously discussed become

$$ZI_L + \Gamma_i\Phi_i + \Gamma\Phi_e = V^i \tag{3.67a}$$

$$\Phi_e = PQ \tag{3.67b}$$

$$-\Gamma_e^T I_L + j\omega Q = I_{Te} \tag{3.67c}$$

$$-\Gamma_i^T I_L = I_{Ti} \ . \tag{3.67d}$$

The connectivity matrix Γ has been split into internal (i) and external (e) parts. The internal potential nodes do not have any charged surfaces. Therefore, they do not require an entry in the potential coefficient matrix. Solve the equations simultaneously to get an admittance matrix with an impressed electric field source.

$$\left[\left(\Gamma^T Z^{-1}\Gamma\right) + \begin{bmatrix} j\omega P^{-1} & 0 \\ 0 & 0 \end{bmatrix}\right] \Phi = I_T + \Gamma^T Z^{-1} V^i \tag{3.68}$$

4. ANALYSIS OF DISTRIBUTED COUPLING ALONG NONPARALLEL TRACES USING PEEC WITH A DYNAMIC GREEN'S FUNCTION AND PHASE TERM EXPANSIONS

Electrically large problems require full-wave calculations that can be handled using PEEC using either static phase approximations, phase term expansions, or the dynamic Green's function directly. When distributed coupling is significant between traces, parallel or nonparallel, a quasi-static approximation will return incorrect results in the coupling terms. Nonparallel coupled lines pose a problem that is not easily solved by transmission lines, but may in some cases be analyzed by lumped element models or quasi-static models when near-end coupling dominates.

Unintentional coupling must be considered when designing printed circuit boards. If the coupling is primarily from parallel trace sections, then the design can be analyzed with transmission line theory. However, where the dominant coupling sections are not parallel, a more complex calculation is required. The problem can be further divided into geometries where the near side coupling is dominant and the more general case where significant coupling is present at separations on the order of a wavelength. The near-side dominant case was discussed in [17]. In that paper a quasi-static Green's function extension of the the partial element equivalent circuit (PEEC) method was used to achieve good results. A similar problem was addressed with a circuit based approach in [10]. Other full-wave methods, like the finite-difference time-domain, may also be applied to such a problem [31]. It is important to note that with coupled lines that are neither parallel nor perpendicular, rectangular gridding methods will have to deal with staircasing issues in the coupling as well as with the electrical length of at least one of the lines. For that reason the nonorthogonal formulation is applied in this paper for the analysis [26].

For the more general case, however, coupling may occur over distances where there is a significant phase difference. In that case a dynamic Green's function formulation is required that is valid over the whole frequency range of concern. Such calculations were done in [4], however, this process is not efficient for practical problems, because of the need to recalculate the partial parameters. For that reason, a compromise was derived that produces accurate results across a band of frequencies without the need to recalculate the partial parameters.

4.1. EXTRACTION OF THE SINGULARITY IN THE DYNAMIC GREEN'S FUNCTION

If the partial coefficient integrations include singularities, high order numerical integrations will be required to achieve the desired accuracy. This problem is avoidable if the singularity can be extracted from the integrand and integrated separately by an analytic expression. The integrations of the self coefficients in the PEEC formulation include such singularities. Formulas to calculate the integrals for the self terms are available for the quasi-static Green's function formulation. These same formulas can be used for a dynamic Green's function formulation with by separating the quasi-static portion of the function from the rest.

The quasi-static form of the Green's function is extracted from the dynamic form to get

$$\begin{aligned} G(\vec{r},\vec{r}') &= \frac{e^{-jk|\vec{r}-\vec{r}'|}}{4\pi|\vec{r}-\vec{r}'|} \\ &= \frac{1}{4\pi|\vec{r}-\vec{r}'|} + \frac{e^{-jk|\vec{r}-\vec{r}'|}-1}{4\pi|\vec{r}-\vec{r}'|} \\ &= G_s(\vec{r},\vec{r}') + G_p(\vec{r},\vec{r}') \ . \end{aligned} \tag{4.1}$$

The first term contains the singularity while the second is numerically integrable for all $\vec{r}$ and $\vec{r}'$, including when $R = |\vec{r}-\vec{r}'| \to 0$. That limit is given by

$$\begin{aligned} \lim_{R\to 0} G_p(R) &= \lim_{R\to 0} \frac{e^{-jkR}-1}{4\pi R} \\ &= \lim_{R\to 0} \frac{-jke^{-jkR}}{4\pi} = \frac{-jk}{4\pi} \ . \end{aligned} \tag{4.2}$$

When the two components of (4.1) are included separately in the PEEC parameter calculations, the quasi-static component need only be calculated once for the whole frequency band, while the numerically integrable phase term must be recalculated at every frequency point. This method is used in the following section to accurately calculate the coupling between nonparallel lines in the next section. The results are compared with the quasi-static results using the same meshing. The recalculations associated with the dynamic Green's function add a significant and often prohibitive amount of time to the overall calculation. For that reason a more efficient approach is suggested and developed in Section 4.3.

4.2. NONPARALLEL COUPLED TRANSMISSION LINE CALCULATION WITH A DYNAMIC GREEN'S FUNCTION

Nonparallel calculations can be done using quasi-static calculations so long as the near side coupling dominates. When a significant portion of the coupling occurs outside this region, a dynamic Green's function may provide more accuracy. The geometry shown in Figure 4.1 was designed to allow for coupling on the near side but still have significant coupling at the far end of the traces. The separation at the far end is roughly $\lambda/3$ at 3 GHz, allowing for a significant phase difference between the two far ends.

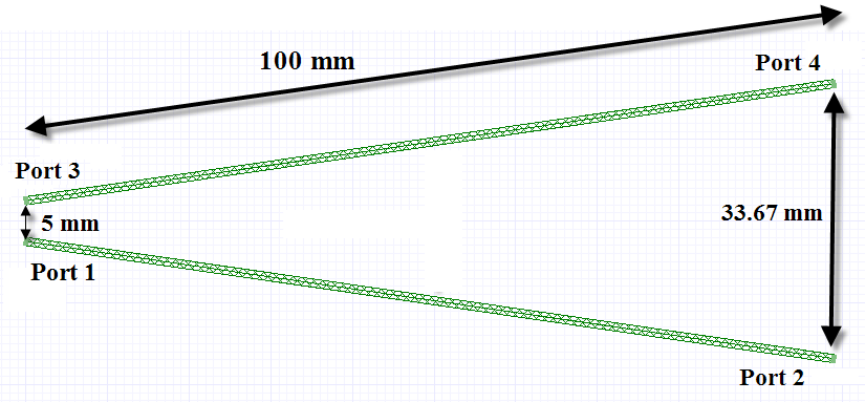

Figure 4.1 A nonparallel microstrip geometry with a far end separation of approximately $\lambda/3$ at 3 GHz

The geometry was simulated on two different PEEC solvers: one using a quasi-static Green's function and the other using a dynamic Green's function. For validation the geometry was also simulated in Ansoft Designer and Agilent ADS. The S_{11} results from the simulations are shown in Figures 4.2 and 4.3. There are no major discrepancies between the simulations in these plots. The return loss is dominated by the conducted currents on each trace, which propagate from current cell to current cell with a fairly small phase difference. Therefore, the quasi-static formulation and the dynamic formulation function equally well.

The near side coupling, S_{31}, is plotted in Figures 4.4 and 4.5. In these plots the quasi-static results exhibit spikes at a few frequency points in both the magnitude and phase plots. Any signal at port 3 must be coupled to it from the other trace, which

at the far end is $\lambda/3$ away at 3 GHz. The quasi-static Green's function contributes the correct magnitude for coupling across these distances. However, the resulting phase difference between the source point and the target point is zero since there is no phase component in the quasi-static Green's function. When the coupling distance is $\lambda/2$, the coupled signal is π radians out of phase from what it should be. Thus, where certain coupled signals should have canceled one another, they may instead add constructively.

There is 100 MHz between the frequency points in the previous PEEC simulations. The S-parameters were recalculated with a smaller frequency step about 2.5 GHz, since the most significant spike in S_{31} phase occured there. Figure 4.6 shows the phase results from 2.38 GHz to 2.62 GHz with 15 MHz between points. While the phase at 2.395 GHz is close to the other simulations, the phase at 2.38 GHz is even farther from other simulations than the error at 2.5 GHz. The dynamic Green's function results do not exhibit any of these spikes, and follow the other two simulations closely.

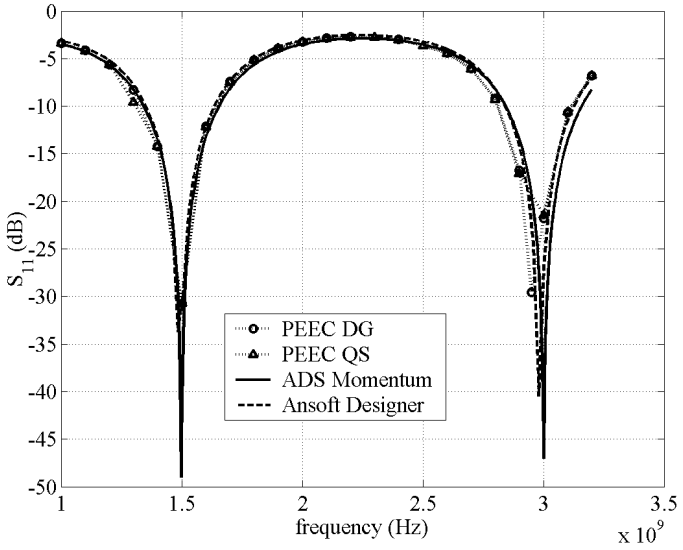

Figure 4.2 $|S_{11}|$ results for four simulation methods

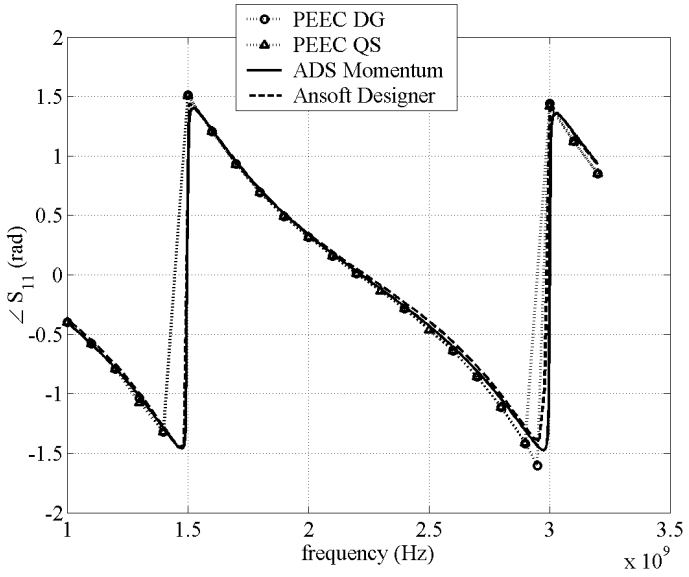

Figure 4.3 The phase of S_{11} results for the four simulations

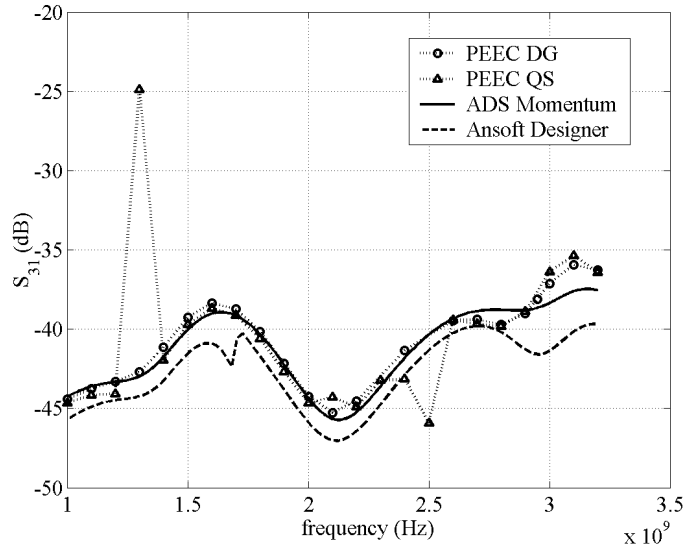

Figure 4.4 $|S_{31}|$ showing the magnitude of the coupling between the two ports on the near side of the coupled transmission lines

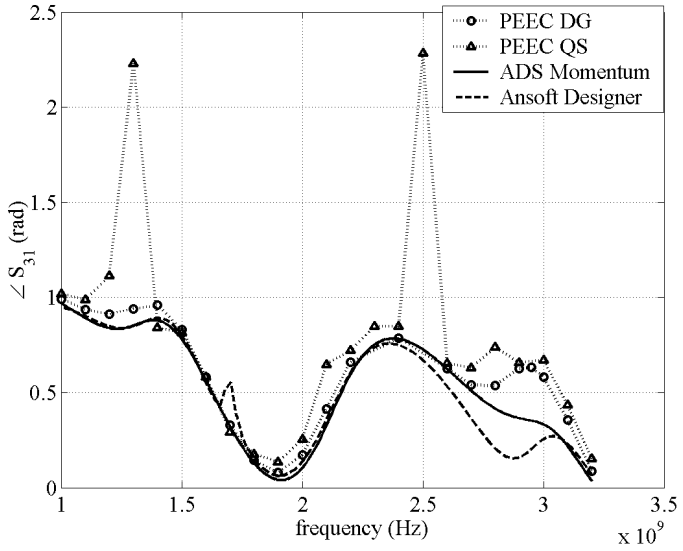

Figure 4.5 The S_{31} phase with similar quasi-static discrepancies as $|S_{31}|$

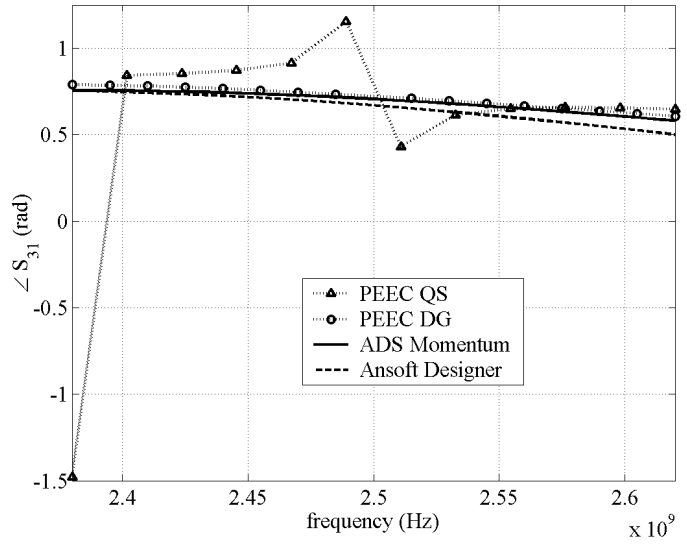

Figure 4.6 The $|S_{31}|$ phase for a narrow-band region about 2.5 GHz

4.3. WIDE-BAND PEEC SOLUTIONS USING TAYLOR EXPANSIONS OF THE GREEN'S FUNCTION

The PEEC method takes a Maxwell equation solution and translates the matrix quantities into circuit parameters. Take the partial inductance term, for example. Within the PEEC formulation there exist a matrix term with a $j\omega$ multiplier. Consider this voltage drop over a single current cell, which can be expressed as

$$V_{Lm} = \sum_n j\omega L_{mn} I_n \ , \tag{4.3}$$

where I_n is the current through the nth current cell. L_{mn} are partial inductance terms which in circuit terms are expressed as either self or mutual inductances. However, (4.3) can be modified so that the mutual terms become dependent sources. That expression is given as

$$V_{Lm} = j\omega L_{mm} I_m + \sum_{n \neq m} \frac{L_{mn}}{L_{nn}} V'_{Ln} \ , \tag{4.4}$$

where $V'_{Ln} = j\omega L_{nn} I_n$, which is not the total drop over the current cell, but rather just the drop associated with the self inductance term.

The partial inductance L_{mn} is calculated by an expression of the form

$$L_{mn} = \mu_0 \int_{V_m} \int_{V_n} \vec{w}_m(\vec{r}) \cdot \vec{w}_n(\vec{r}\,') G(\vec{r}, \vec{r}\,') dV(\vec{r}\,') dV(\vec{r}) \ . \tag{4.5}$$

The permeability is assumed to be constant or it would also be within the integrals. $G(\vec{r}, \vec{r}\,')$ is a Green's function. Commonly, the quasi-static Green's function approximation for free-space is used. This approximation is convenient because it yields real results for L_{mn}. To be fully accurate in the time domain, a delay must be included to account for the speed of light in the medium [8]. This delay is also commonly used in PEEC solvers, but the stability of such solvers using this method is often questionable. Reasons for the instability have been proposed, which suggest that step changes at the arrival of a delayed reaction imply infinite bandwidth [13]. Filtering schemes have been suggested to limit the bandwidth required maintain stability.

This problem can be addressed from a different angle starting with the dynamic Green's function,

$$G(\vec{r}, \vec{r}\,') = \frac{e^{-jkR}}{4\pi R}, \ R = |\vec{r} - \vec{r}\,'| \ . \tag{4.6}$$

The dynamic Green's function is the most accurate form to use in the problem solution. However, using this form, requires that the partial parameters be recalculated at each frequency step. For any practical problem, this extra step is too time consuming to make the accuracy worthwhile. Full-wave PEEC solutions use time delays to retain the phase accuracy. These delays may be approximated by center-to-center cell distances. Or, another method used calculates the partial parameter at a particular frequency with the dynamic Green's function. This complex partial parameter provides a weighted-integral estimate of the phase and thus, the delay.

First, take a Taylor expansion of the exponential term about $j\omega_0$

$$\begin{aligned} e^{-jkR} &= e^{j\omega(-R/c_0)} \\ &= e^{-j\omega_0 R/c_0}\left[1 + (j\omega - j\omega_0)\left(\frac{-R}{c_0}\right) + \frac{(j\omega - j\omega_0)^2}{2}\left(\frac{-R}{c_0}\right)^2 + \cdots\right] \\ &= e^{-j\omega_0 R/c_0}\sum_{n=0}^{\infty}\frac{(j\omega - j\omega_0)^n}{n!}\left(\frac{-R}{c_0}\right)^n . \end{aligned} \tag{4.7}$$

Then, combine (4.7) with (4.6) to get

$$\begin{aligned} G(\vec{r},\vec{r}\,') &= \frac{e^{-j\omega_0 R/c_0}}{4\pi R}\sum_{n=0}^{\infty}\frac{(j\omega - j\omega_0)^n}{n!}\left(\frac{-R}{c_0}\right)^n \\ &= \sum_{n=0}^{\infty} g_n(\vec{r},\vec{r}\,') . \end{aligned} \tag{4.8}$$

Note that $g_0(\vec{r},\vec{r}\,')$ is simply the quasi-static Green's function with a exponential phase term fixed in frequency.

When the expansion is introduced into (4.5), the single partial element matrix can be considered as multiple matrices with $j\omega$ multipliers.

$$\begin{aligned} L_{mn} &= \sum_{k=0}^{\infty}\mu_0\int_{V_m}\int_{V_n}\vec{w}_m(\vec{r})\cdot\vec{w}_n(\vec{r}\,')g_k(\vec{r},\vec{r}\,')dV(\vec{r}\,')dV(\vec{r}) \\ &= \sum_{k=0}^{\infty}(j\omega - j\omega_0)^k\frac{\mu_0}{k!}\int_{V_m}\int_{V_n}\vec{w}_m(\vec{r})\cdot\vec{w}_n(\vec{r}\,') \\ &\qquad\qquad \times\frac{e^{-j\omega_0 R/c_0}}{4\pi R}\left(\frac{-R}{c_0}\right)^k dV(\vec{r}\,')dV(\vec{r}) \\ &= \sum_{k=0}^{\infty}(j\omega - j\omega_0)^k L_{mn}^k \end{aligned} \tag{4.9}$$

L^k_{mn} is kth expansion term of the partial inductances. The same process is used to find the expansion terms for the partial potentials.

When integrating the expansion terms, the only singularity is in the integrand of the 0th order term, which is given by

$$g_0(\vec{r},\vec{r}') = \frac{e^{-j\omega_0 R/c_0}}{4\pi R} \ . \tag{4.10}$$

The term in (4.10) is identical to the dynamic Green's function calculated at f_0. Therefore, the integrations previously developed for Sections 4.1 and 4.2 can be reused again for this integration. The higher-order terms of the expansion do not have any finite singularities. So, these terms can be integrated numerically.

In practice, the term matrices are calculated once and stored. Then, at each frequency point the term matrices are recombined using (4.5). The process of multiplying the term matrices by the next frequency and summing takes a small fraction of the time required for the solution of the system of equations, making it a much preferable choice to the parameter recalculations required for the dynamic Green's function.

As an example, the model described in Section 4.2 was recalculated using the wide-band PEEC solution for several terms in Figure 4.7. As the number of terms in the calculation is increased the results converge.

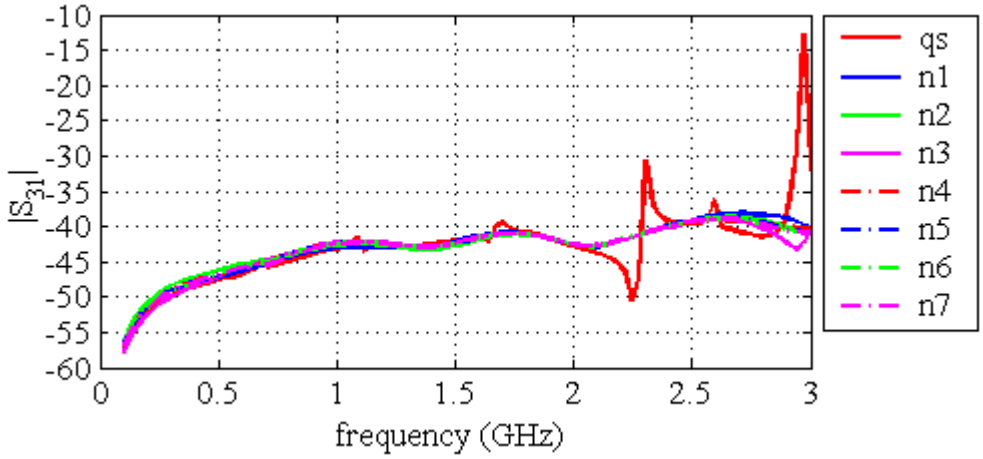

Figure 4.7 $|S_{31}|$ for the nonparallel lines with expansions from 1 to 7 terms

4.4. WIDE-BAND PEEC SIMULATIONS ON COUPLED TRACES

In this section a similar model to that of Figure 4.1 is considered. This general layout of this model is shown in Figure 4.8. The parameter calculations described in Section 4.3 have many factors determining the accuracy of the solution. Some factors, like the number of terms used and the choice of center frequency, are inherent in the expansion. An additional factor is introduced limiting the support of the approximation to avoid using inaccurate parameter calculations. In addition, three positions for Line 1 in Figure 4.8 are considered, and results for each are discussed where they provide insight to the workings of the wide-band PEEC solution. The grids for these calculations are shown in Figure 4.9.

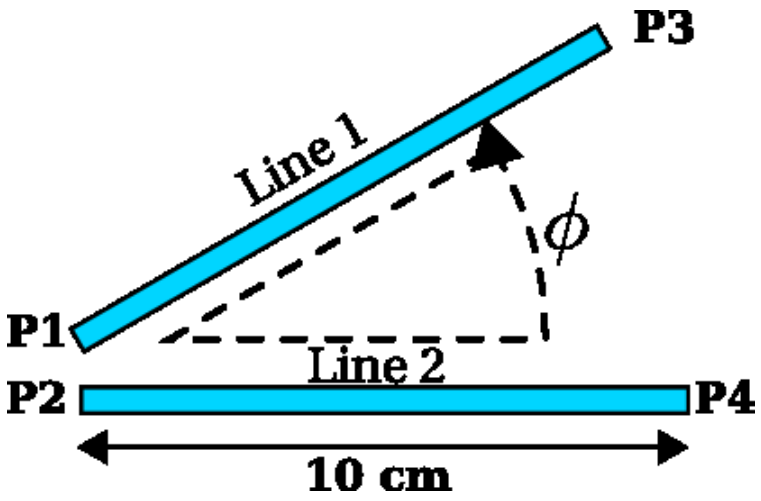

Figure 4.8 Two coupled traces with Line 1 rotated relative to Line 2

4.4.1. Number of Expansion Terms. In general Taylor expansions converge as more terms are added. The speed of this convergence depends on the function in question. Progressively adding terms seems like it should only be able to add accuracy. However, there are exceptions. Using $n = 1$ provides an approximation exact at the center frequency and approximate over a small band. The $n = 1$ approximation is also bounded. Conversely, $n = 2, 3$ provide more accurate approximations at nearby frequencies but are unbounded. For increasing $f - f_0$, $n = 1$ will actually retain more accuracy, or rather less inaccuracy, than an approximation with a few more terms.

The S-parameters were calculated for the grids shown in Figure 4.9 using a center frequency of 3 GHz. The return loss, S_{11}, and the through loss, S_{31}, are not affected by the trace orientation or the number of terms used. Figure 4.10 shows $|S_{11}|$ for the parallel traces. All of the PEEC traces overlap with the dynamic Green's function result. More terms are required for the 30°- and 45°-trace pairs than the parallel traces. The coupling terms for the parallel traces are shown in Figure 4.11 through Figure 4.13. With the exception of the $n = 1$ solution, there is is little distinguishing the other expansion solutions from the dynamic Green's function solution.

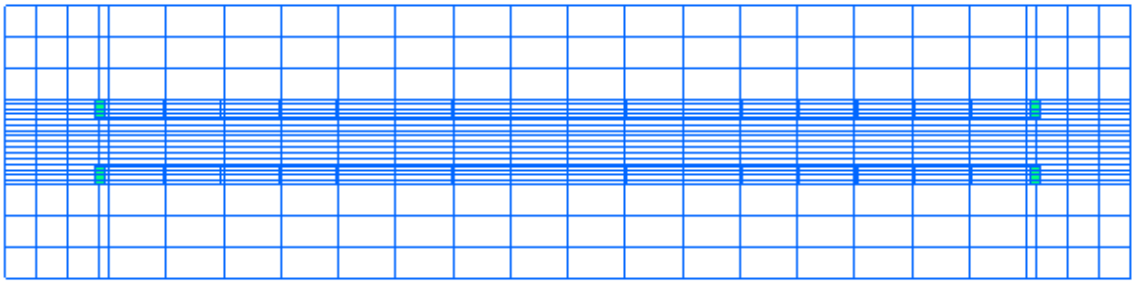

(a) Parallel Traces ($\phi = 0°$)

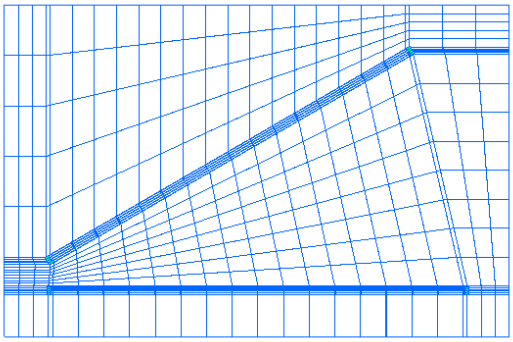

(b) Nonparallel Traces ($\phi = 30°$)

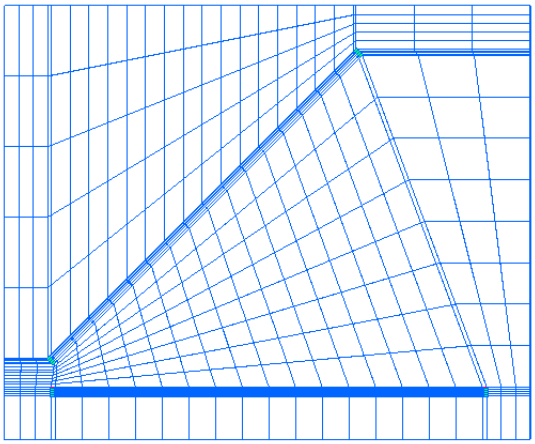

(c) Nonparallel Traces ($\phi = 45°$)

Figure 4.9 Coupled trace grids for PEEC

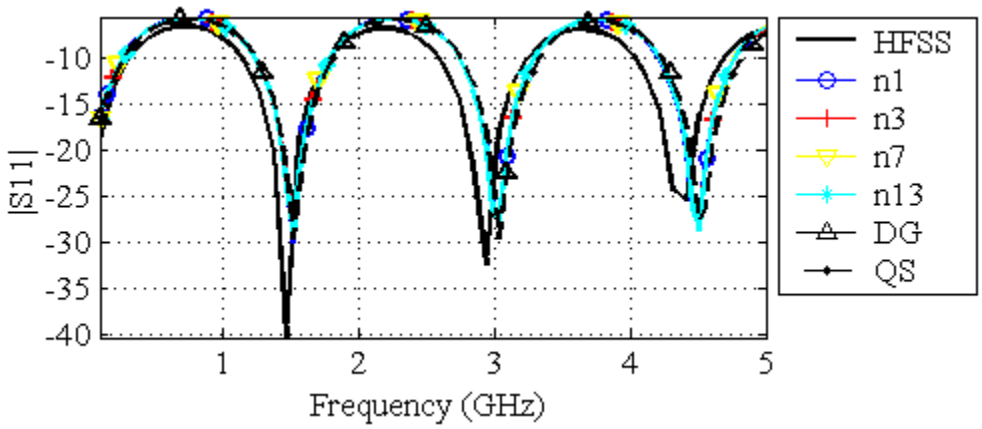

Figure 4.10 $|S_{11}|$ for parallel traces using the quasi-static, dynamic, and expansion Green's function solutions

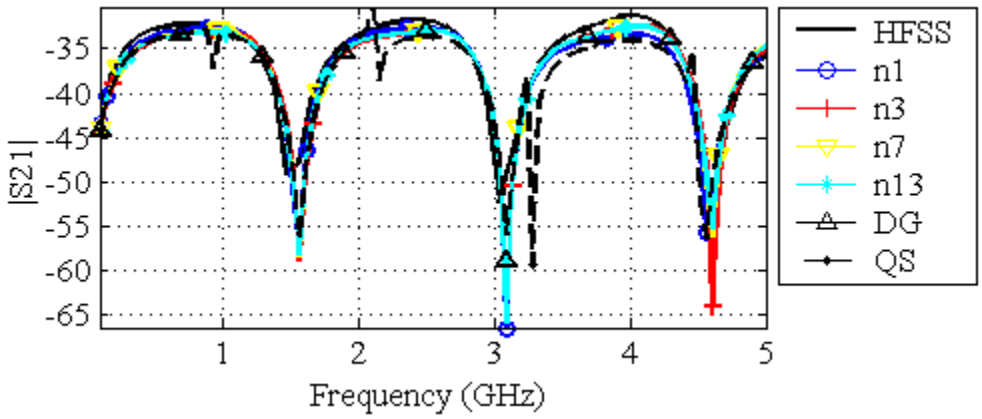

Figure 4.11 $|S_{21}|$ for parallel traces using expansion solutions and a dynamic Green's function solution

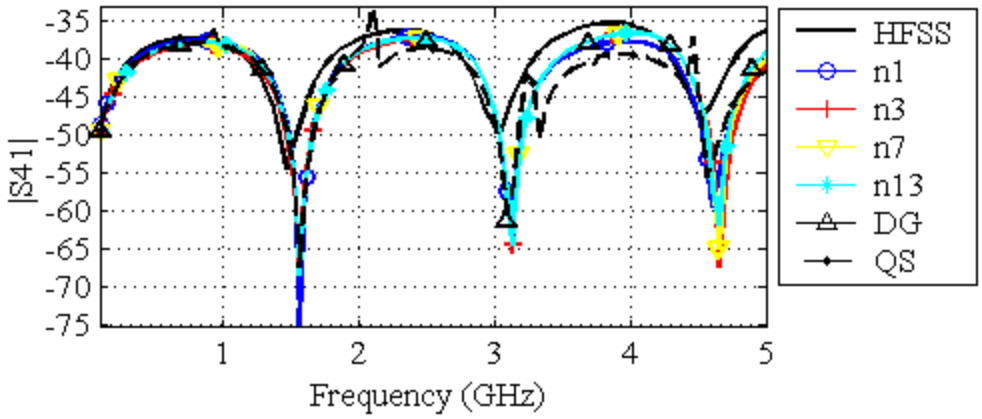

Figure 4.12 $|S_{41}|$ for parallel traces using expansion solutions and a dynamic Green's function solution

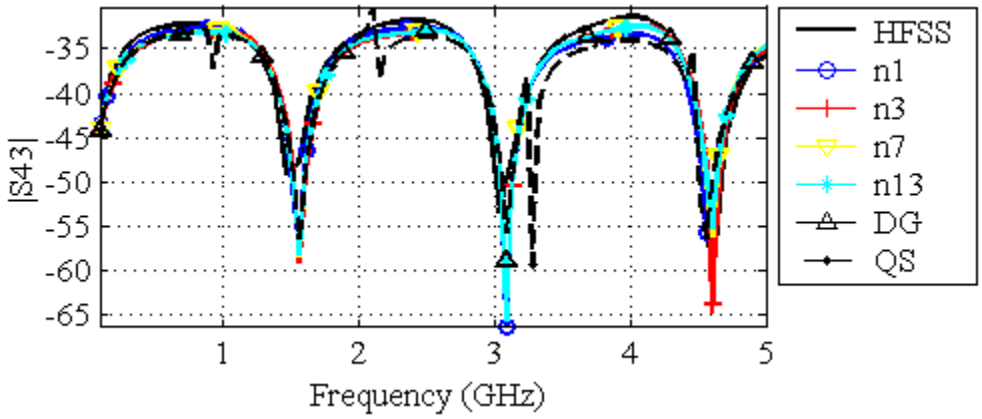

Figure 4.13 $|S_{43}|$ for parallel traces using expansion solutions and a dynamic Green's function solution

The coupling parameters for the 30°-trace pair are shown in Figure 4.14 through Figure 4.16. The near-side coupling, S_{21} calculation is fairly accurate with all of the expansion calculations. However, it requires seven or more terms for the traces to start to converge near the edges of the calculation band. The far-side coupling, S_{43}, is even slower to converge. Solutions with up thirteen terms are shown to see the convergence.

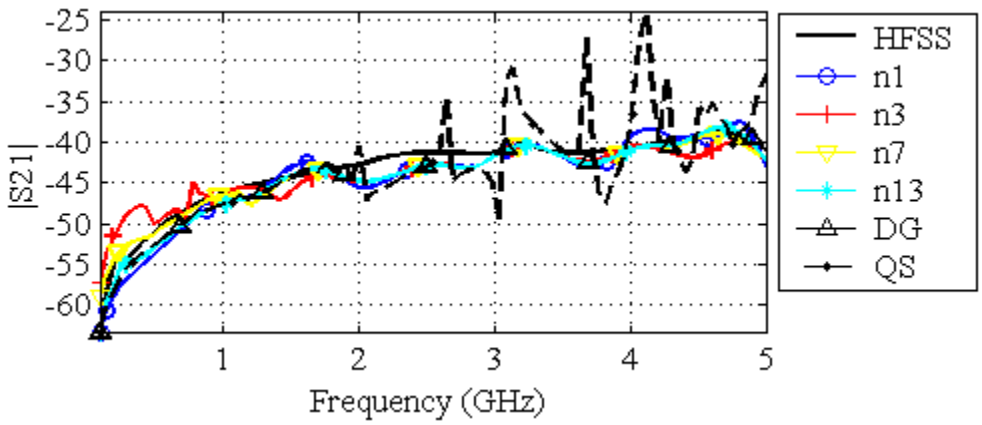

Figure 4.14 $|S_{21}|$ for nonparallel traces with a 30° separation using expansion solutions and a dynamic Green's function solution

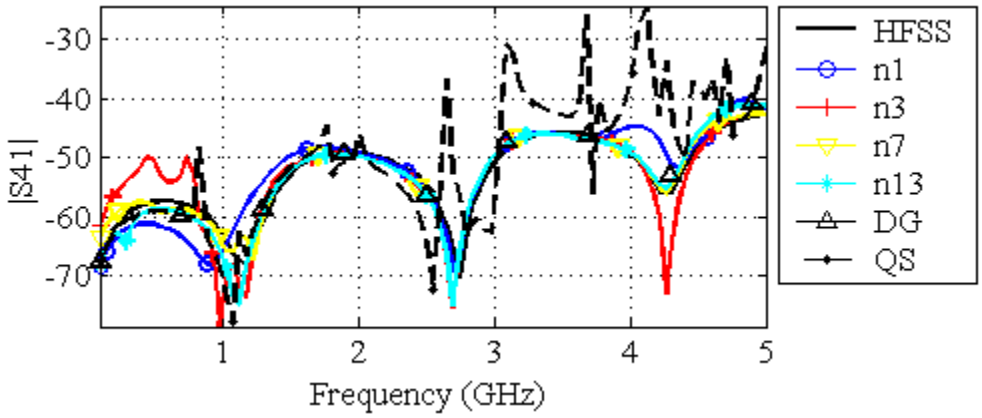

Figure 4.15 $|S_{41}|$ for nonparallel traces with a 30° separation using expansion solutions and a dynamic Green's function solution

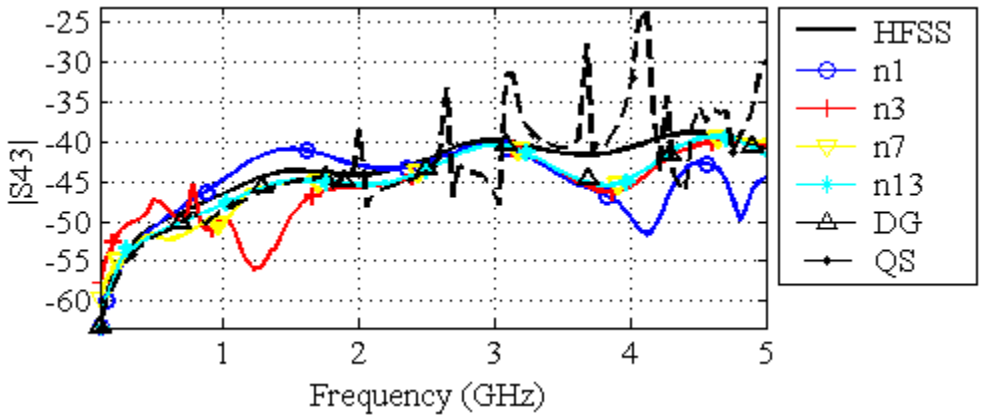

Figure 4.16 $|S_{43}|$ for nonparallel traces with a 30° separation using expansion solutions and a dynamic Green's function solution

The coupling parameters for the 45°-trace pair are shown in Figure 4.17 through Figure 4.19. The results here are similar to the results for the 30°-trace pair, but more terms are again required to converge for the entire frequency band. Only with eleven and thirteen terms do the traces get close to converging across the full frequency band. Actually, the traces for the expansion calculations significantly diverge below 2 GHz and above 4 GHz. The expansion calculations are well-grouped in 2-GHz span about the center frequency. Clearly, the greater separation of the far ends for the 45°-trace pair requires the phase component of the Green's function to be accurate to calculate the correct coupling terms. The near-end couplings require fewer terms to get very close the dynamic Green's function calculation than the far-end couplings.

Overall, the one-term approximation provides better solutions than the three-term approximations. This may be owed to the unbounded nature of the three-term approximation. As more terms are added, the approximation converges to the dynamic solution. However, even considering the far-end coupling in Figure 4.19, the one-term approximation is not bad over a span of 1 GHz.

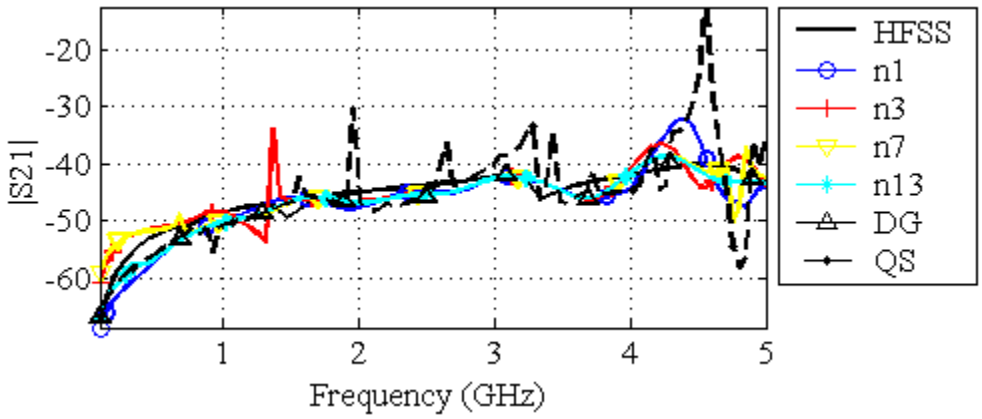

Figure 4.17 $|S_{21}|$ for nonparallel traces with a 45° separation using expansion solutions and a dynamic Green's function solution

4.4.2. Center Frequency Effect on Result Accuracy. The 30°-separated pair of traces is used in this section to investigate the effect of the center frequency, f_0, on accuracy at other frequencies. The placement of the center frequency determines the most accurate frequency region in the calculation. Ultimately, error estimates like the one presented in the next section can be used to predict when the

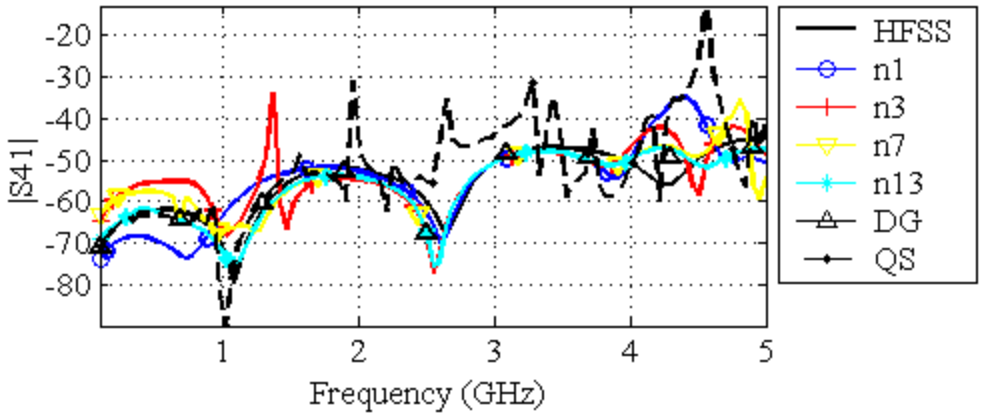

Figure 4.18 $|S_{41}|$ for nonparallel traces with a 45° separation using expansion solutions and a dynamic Green's function solution

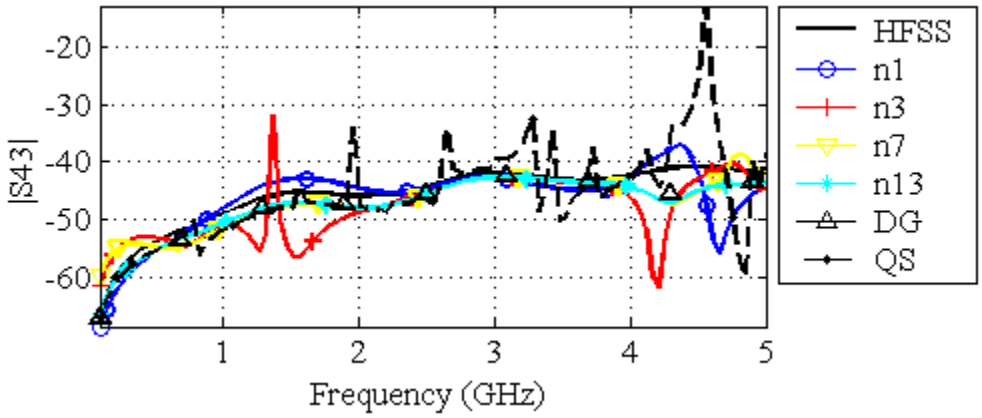

Figure 4.19 $|S_{43}|$ for nonparallel traces with a 45° separation using expansion solutions and a dynamic Green's function solution

Green's function approximation has reached the limit of its accuracy with respect to frequency. Once the limit has been reached, a new center frequency can be set, and new partial parameters calculated. Depending on the number of terms used in the approximation, a single parameter calculation may be all that is needed for a wide-band calculation, spanning many gigahertz.

The nonparallel trace geometry was simulated with three different center frequencies, using a 7-term approximation. As should be expected, the results are most accurate for the simulation using $f_0 = 2.5$ GHz, which is in the middle of the band.

The S-parameters calculated are shown in Figure 4.20 through Figure 4.23. The return loss results are nearly unchanged by the choice of f_0. However, the far-end coupling calculations are very different. For $f_0 = 0.1$ GHz, the results are only accurate up to 1 GHz. For $f_0 = 2.5$ GHz the approximation matches the dynamic solution within a dB up to 4 GHz. From 3 GHz and to 5 GHz, the approximation centered at 4.9 GHz is accurate with respect to the dynamic solution.

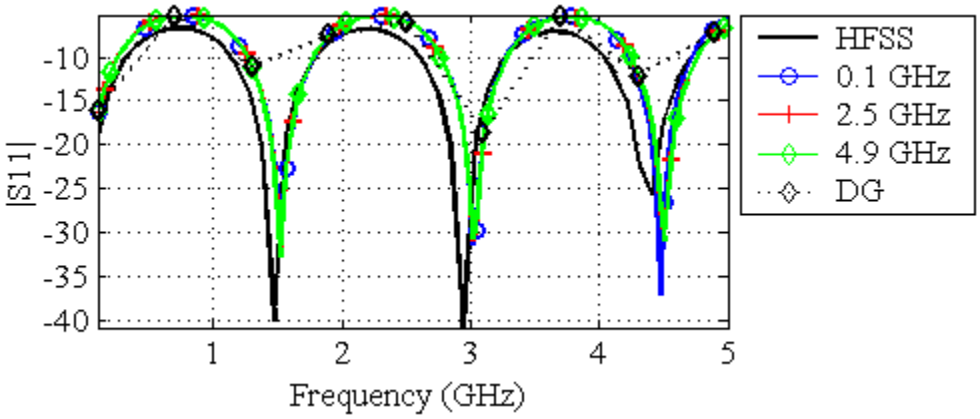

Figure 4.20 $|S_{11}|$ calculated for three center frequencies

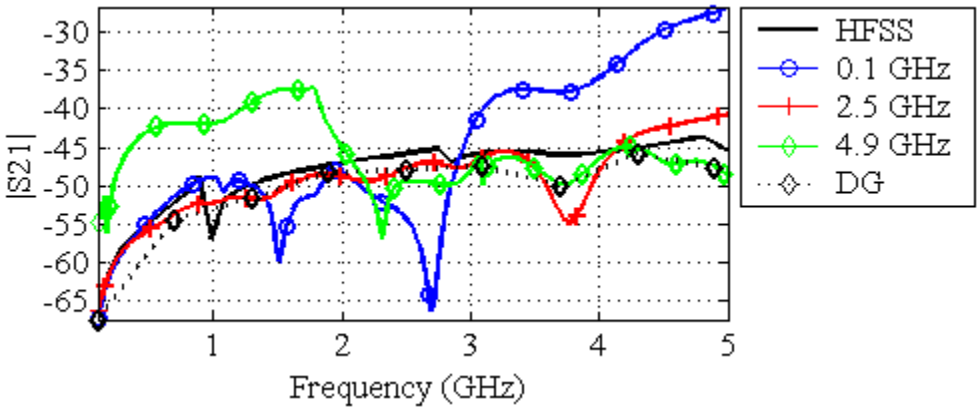

Figure 4.21 $|S_{21}|$ calculated for three center frequencies

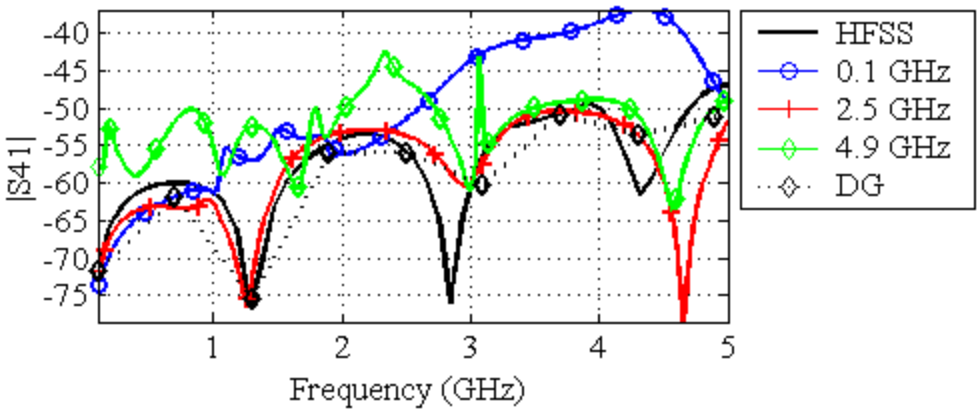

Figure 4.22 $|S_{41}|$ calculated for three center frequencies

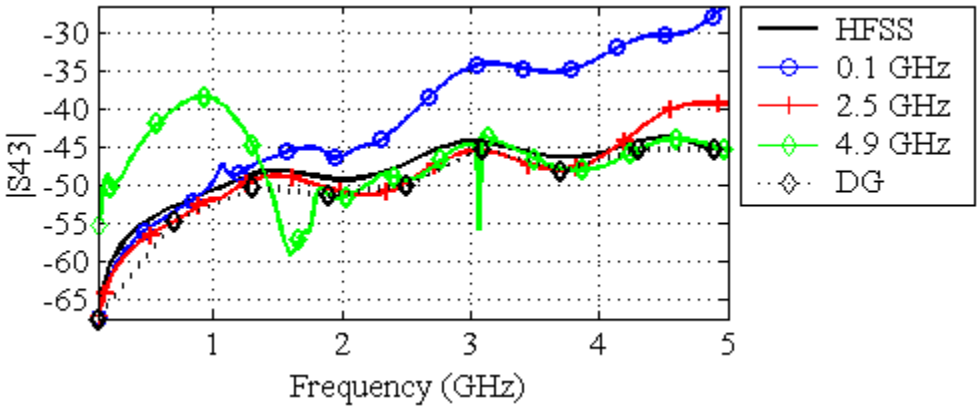

Figure 4.23 $|S_{43}|$ calculated for three center frequencies

4.4.3. Green's Function Error Approximation and Range Limiting. As the difference in f and f_0 increases, so does the difference in the dynamic Green's function and the Taylor expansion of Green's function used in the previous sections. An error estimate for the complex exponential part of the Green's function is developed based on Taylor's formula. This estimate is used to determine frequencies and distances where the expansion exceeds an arbitrary error limit.

For a N-time continuously differentiable real-valued function of a real variable, $f(x)$, Taylor's formula gives the following equality:

$$f(x) = \sum_{n=0}^{N-1} \frac{f^{(n)}(x_0)}{n!}(x - x_0)^n + \frac{f^{(N)}(a)}{N!}(x - x_0)^N \ , \tag{4.11}$$

for some a between x_0 and x. The function that has been expanded in this report is a complex exponential, which can be decomposed into its real and imaginary parts and treated separately by Taylor's formula and recombined. The result is

$$e^{jx} = \sum_{n=0}^{N-1} \frac{e^{jx_0}}{n!}(x - x_0)^n + (-j)^N \frac{\cos(a_1) + j\sin(a_2)}{N!}(x - x_0)^N \ , \tag{4.12}$$

for a_1 and a_2 between x_0 and x. Then, the error is given as

$$\begin{aligned} \epsilon_N &= \left| (-j)^N \frac{\cos(a_1) + j\sin(a_2)}{N!}(x - x_0)^N \right| \\ &= \frac{|\cos(a_1) + j\sin(a_2)|}{N!}|x - x_0|^N \ . \end{aligned} \tag{4.13}$$

Let $a = \frac{a_1+a_2}{2}$ and $\delta a = \frac{a_1-a2}{2}$. Then, the cosine and sine portion of (4.13) becomes

$$\begin{aligned} |\cos(a_1) + j\sin(a_2)| &= \left| e^{ja}\cos\delta a + -je^{-ja}\sin\delta a \right| \\ &= \sqrt{1 - \sin(2a)\sin(2\delta a)} \ , \end{aligned} \tag{4.14}$$

which is always greater than 0 and less than 2. Assuming that $\delta a \approx 0$, then (4.14) becomes 1. This error estimate will be used as a guide in the calculations. Using the assumption, the error estimate from (4.13) becomes

$$\epsilon_N = \frac{|x - x_0|^N}{N!} \ . \tag{4.15}$$

Replace x and x_0 with jkR and jk_0R, respectively. Then, two useful forms of the error can be formed. The first is a frequency limit given by

$$|f_{\text{lim}} - f_0| = \frac{(\epsilon_N N!)^{1/N}}{2\pi R/c_0} \ . \tag{4.16}$$

The frequency limit is meant to be used to determine at what frequencies the partial parameters should be recalculated. Several parameter calculations may be required

for very large frequency ranges. The second expression is a limit on R given by

$$R_{\text{lim}} = \left(\frac{c_0}{2\pi}\right) \frac{(\epsilon_N N!)^{1/N}}{|f - f_0|} \tag{4.17}$$

The phase error estimate is tested against the actual error calculated for different values of N in Figure 4.24 through Figure 4.26. The error estimate is given in red, and the black and gray regions mark values of R and f for which the error is below the set limit. While the red curve is an error estimate, the acceptable error region (in black and grey) is calculated by a direct comparison of the dynamic Green's function and the value of the estimate. So, the error estimate is accurate and acceptable for the use of determining valid cell interactions on a phase error basis. It is worth noting that the error for a 1-term approximation or a quasi-static approximation never exceeds 2, however, approximations with more than 1 term are unbounded, and require the error bound to avoid excessive error.

For the simulations described in this report, a limit for R is calculated given the highest frequency of interest and the number of terms used in the Green's function approximation. This is a static approximation with respect to frequency after the initial calculation. When the partial parameters are calculated, the center-to-center distance of the cells is calculated, and if this distance exceeds the limit on R, the partial parameter is set to zero. Alternatively, the limit can be enforced at each calculation of the Green's function approximation. This application of the limit was used for results in Figure 4.7. This method tends to produce more accurate results when larger cells are used. However, it is troublesome when applied with iterative integrations.

Figure 4.27 shows a diagram of how the static limit on R works with the error estimate. Provided f_0 is not set in the middle of the calculation band, the error limit is exceeded at some lower frequencies. Additionally, in the middle of the band, the limit is much lower than necessary. When $f \to f_0$, the approximation becomes exact and valid for all R. These problems can be avoided by initially calculating all of the partial parameter interactions for each term. Then, when the partial inductance or partial potentials matrix is being assembled for each frequency step, interactions that fall outside the error limit for that frequency can be set to zero. This method requires a separate matrix storing the cell distances.

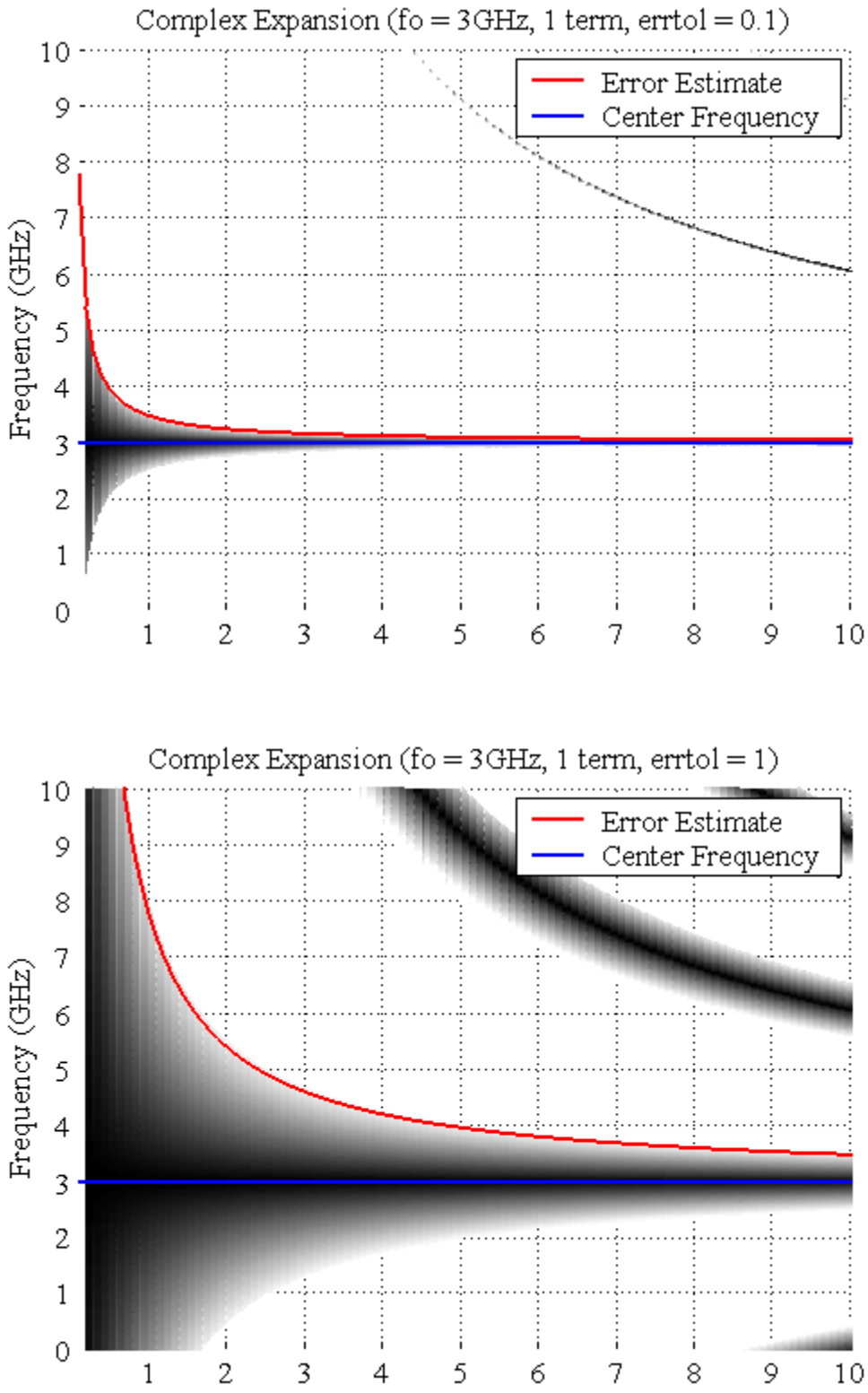

Figure 4.24 The region of accuracy for the Green's function approximation for $n = 1$

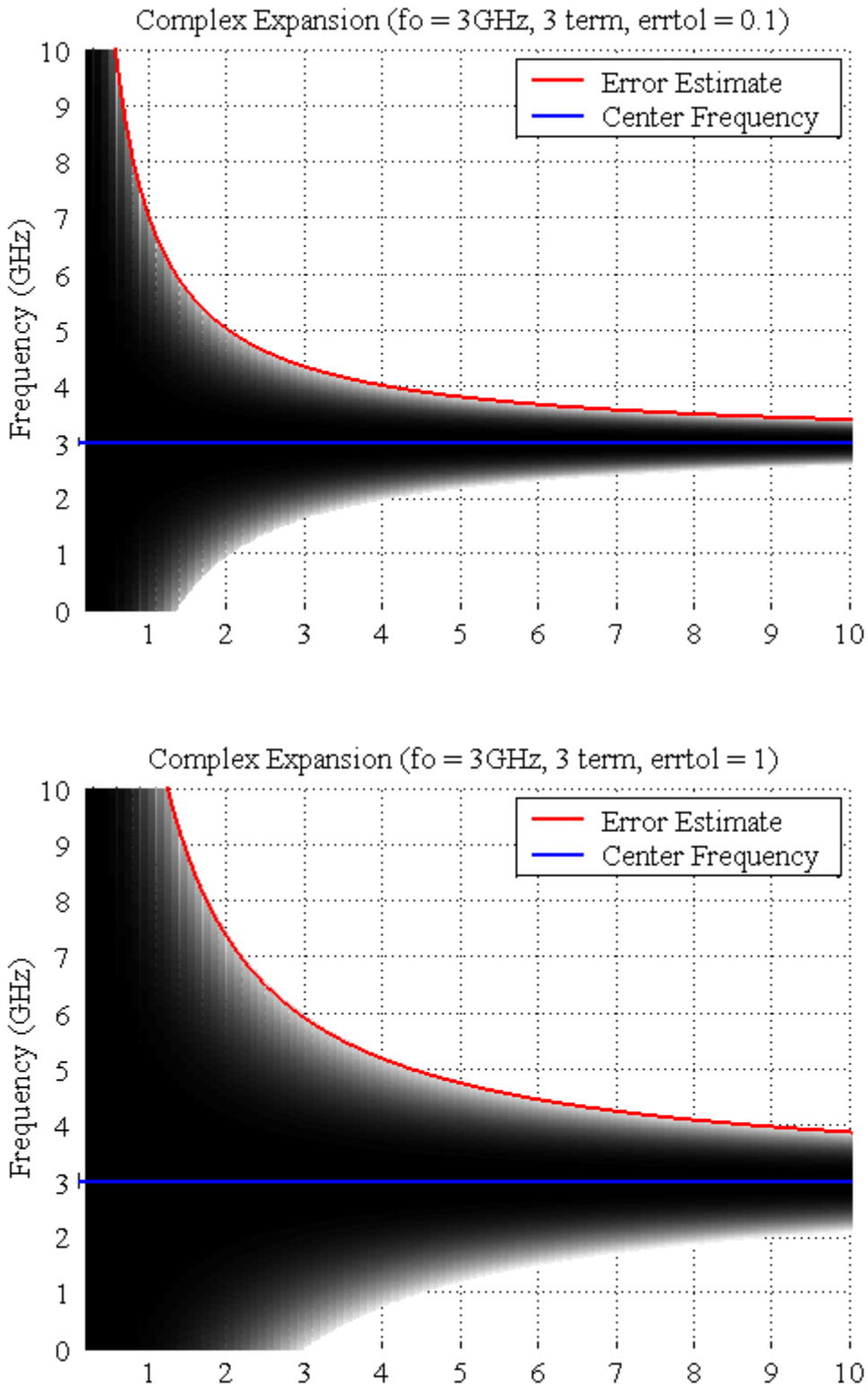

Figure 4.25 The region of accuracy for the Green's function approximation for $n = 3$

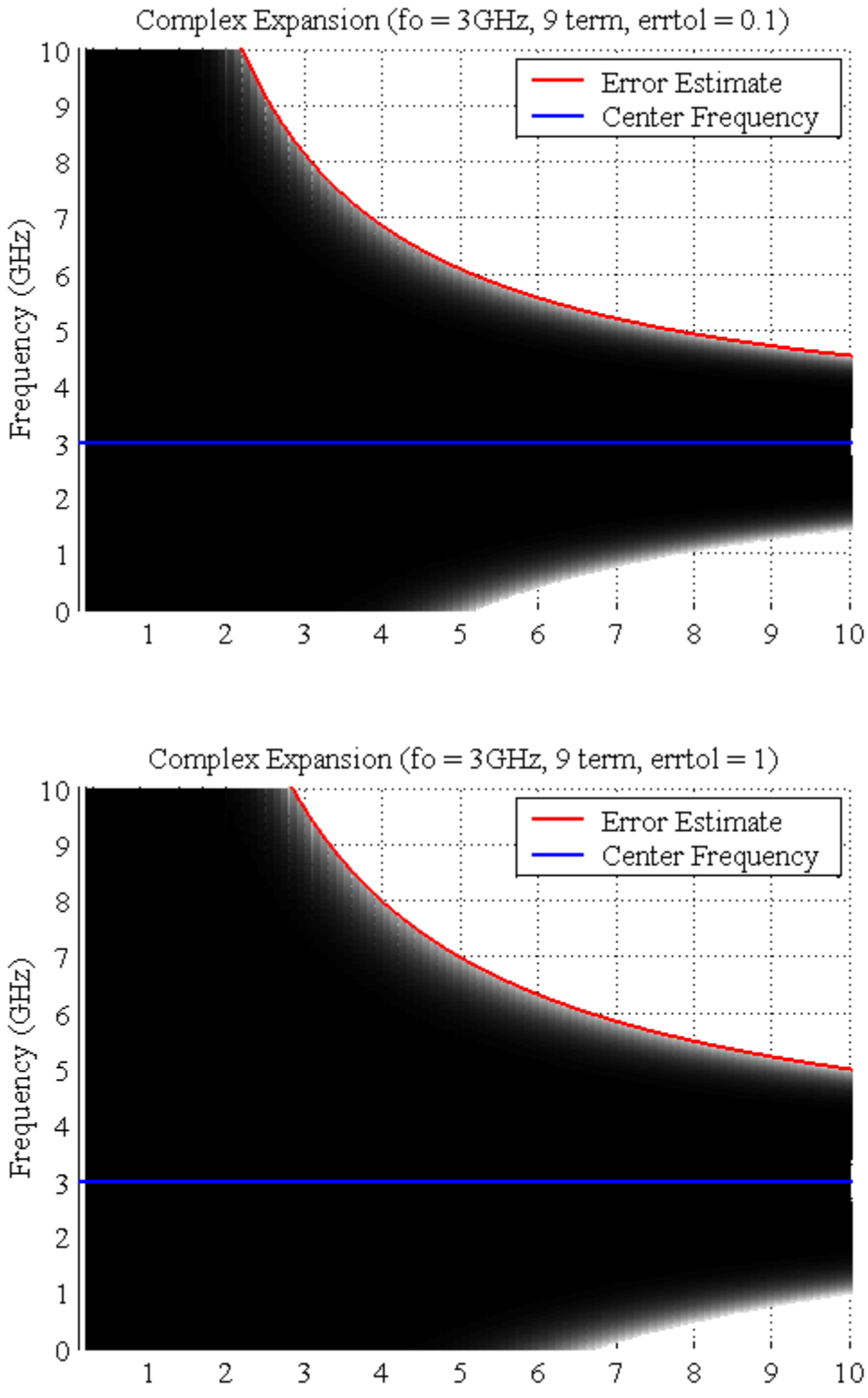

Figure 4.26 The region of accuracy for the Green's function approximation for $n = 9$

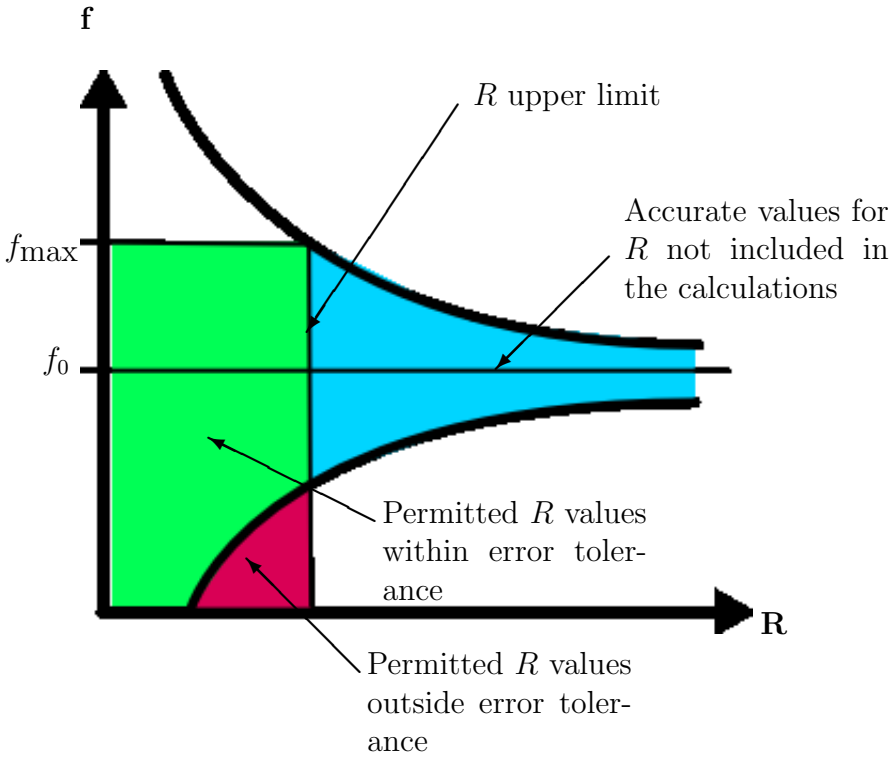

Figure 4.27 Limits set on R given the center frequency and error tolerance

Table 4.1 shows the maximum distance for cell interactions allowed for the three error levels. Figure 4.28 through Figure 4.31 show the S-parameters calculated using a 3-term approximation with a center frequency at 3 GHz. The error is allowed to be 0.1, 1., or 10^{50}. A limit of 10^{50} effectively allows all cell interactions in this model.

Table 4.1 R limits based on a 7-term Green's function approximation with the upper frequency set at 5 GHz and the center frequency at 3 GHz

ϵ_7	R_{lim} (cm)
0.1	5.81
1.0	8.07
10^{50}	1.1×10^8

When compared with HFSS and each other, the near-end coupling, S_{21}, shown in Figure 4.29 is not severely effected by these error settings. Since R_{lim} is significantly greater than the near-end trace separation for this model, the dominant interactions are captured in all three simulations. The near to far end coupling, S_{41}, in Figure 4.30 is represented well by $\epsilon_7 = 1.$ and $\epsilon_7 = 10^{50}$, but the $\epsilon_7 = 0.1$ simulation is less consistent. This trend continues in the far-end coupling shown in Figure 4.31, where only the $\epsilon_7 = 10^{50}$ simulation allows enough terms to retain accuracy through the full frequency range. Allowing such a large error is not a good idea for approximations with few terms, but in this case, the results are not bad. A lower error tolerance of 10 or lower would be preferable.

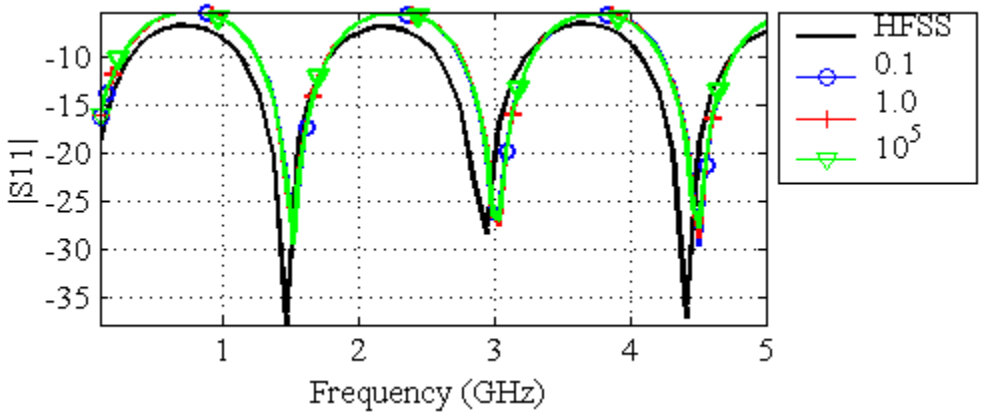

Figure 4.28 $|S_{11}|$ calculated using a 7-term approximation with different Green's function error tolerances for the 45°-trace pair

4.5. SUMMARY AND CONCLUSIONS

For nonparallel traces a quasi-static PEEC formulation may be used, but the results may include some errors due to the lack of in phase information. These phase differences are incorporated by using a dynamic Green's function in the formulation. The dynamic Green's function requires new calculation algorithms to deal with the complex exponential in the integrand. However, the singularity in the Green's function can be extracted with a little algebra to get the original quasi-static term and another numerically integrable term associated with the phase information. Thus,

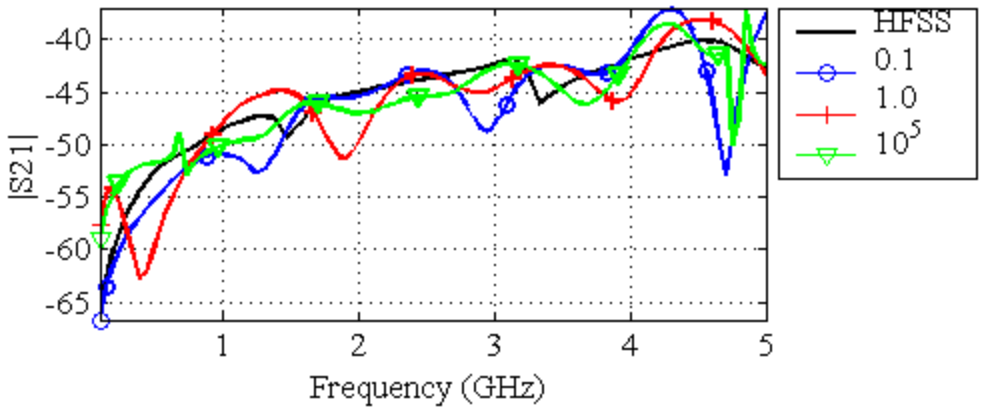

Figure 4.29 $|S_{21}|$ calculated using a 7-term approximation with different Green's function error tolerances for the 45°-trace pair

previous analytical expressions for quasi-static formulations may be reused, and the phase term calculated separately without compromising the dynamic Green's functions accuracy. Further accuracy in these calculations is obtained by using a subgridding method that does not increase the number of unknowns.

Wide-band PEEC solutions can be generated using a Taylor expansion for the phase term in the dynamic Green's function. These approximations to the Green's function have accuracy over a band of frequencies, where as the dynamic Green's function is exact a single frequency. For a true dynamic Green's function solution, the partial parameters need to be recalculated at every frequency point. The approximation allows large bands to be calculated with a single parameter calculation. The accuracy of this method is subject to the number of terms used in the Green's function approximation, the expansion frequency, and an error tolerance that was derived.

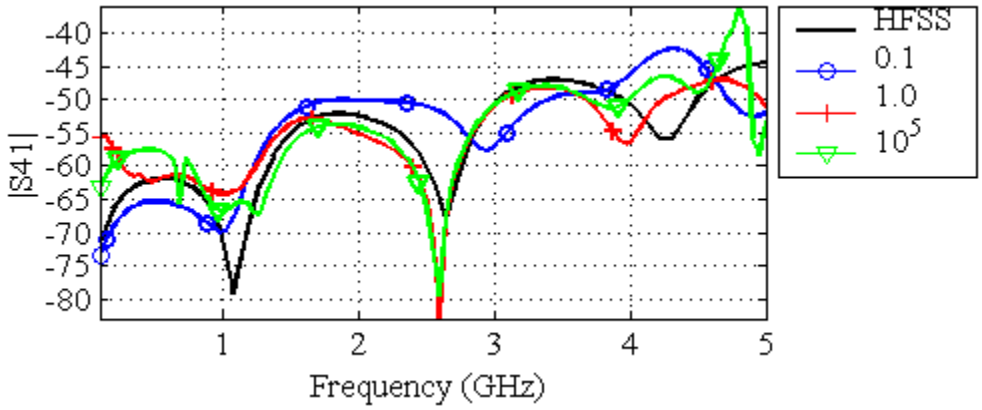

Figure 4.30 $|S_{41}|$ calculated using a 7-term approximation with different Green's function error tolerances for the 45°-trace pair

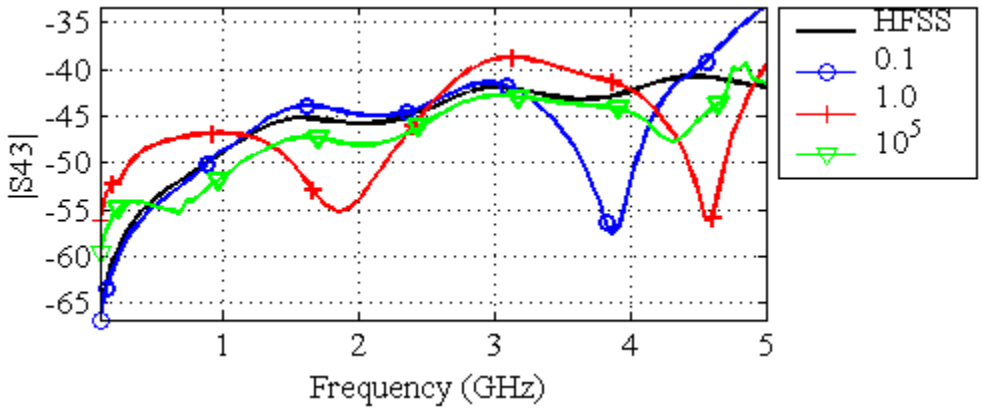

Figure 4.31 $|S_{43}|$ calculated using a 7-term approximation with different Green's function error tolerances for the 45°-trace pair

5. HYBRID PEEC-CAVITY MODELS FOR INTERCONNECTS ON POWER BUSES

The cavity model has been applied to power buses of various shapes and sizes. These models are effective at simulating decoupling capacitors on power buses. The partial-element equivalent-circuit (PEEC) method is effective for modeling complex interconnect structures in a full-wave sense. However, due to the full-matrix nature of the PEEC matrices, it is impractical to model large power bus structures. Combining the two methods may achieve the best characteristics from both methods.

Power distribution network (PDN) analysis is a crucial component in design. Bit errors are more likely when sufficient power is not available for circuits during fast transients. Cavity model based solvers have been used for some time now to calculate the input and transfer impedances for a power bus structure [16]. SPICE files may be generated from the cavity models. Then, via circuit models and component parasitics can be introduced at the ports to get an accurate answer over wide bandwidths [14, 15, 32, 33]. This approach will work well as long as their is a circuit equivalent for the power bus interconnect in question.

The partial-element equivalent-circuit (PEEC) method is very good for calculating equivalent circuits for general, 3D interconnects. However, a large number of unknowns is required for modeling large power bus structures in PEEC, which is not typically feasible. This work endeavors to combine the best capabilities of the PEEC and cavity methods to solve interconnect problems for PDNs and interconnect problems in the presencet of PDNs.

5.1. TRACE-FED PATCH ANTENNA

A trace-fed cavity, or a microstrip patch antenna, is shown in Figure 5.1. The PEEC and cavity model division will be made along a line for simplicity. This problem will be handled in at least two different divisions. For the first hybrid model the trace alone is simulated by PEEC, and the cavity is completely handled by the cavity model. For the second hybrid model PEEC is used to model the trace and part of the cavity.

The connecting trace is 1 cm long by 0.2 cm wide, and the cavity is 5 cm long by 4 cm wide to avoid degenerate modes. A dielectric constant of $\varepsilon_r = 9.8$ is used for the substrate. The bottom of the structure is a solid copper sheet, which is modeled

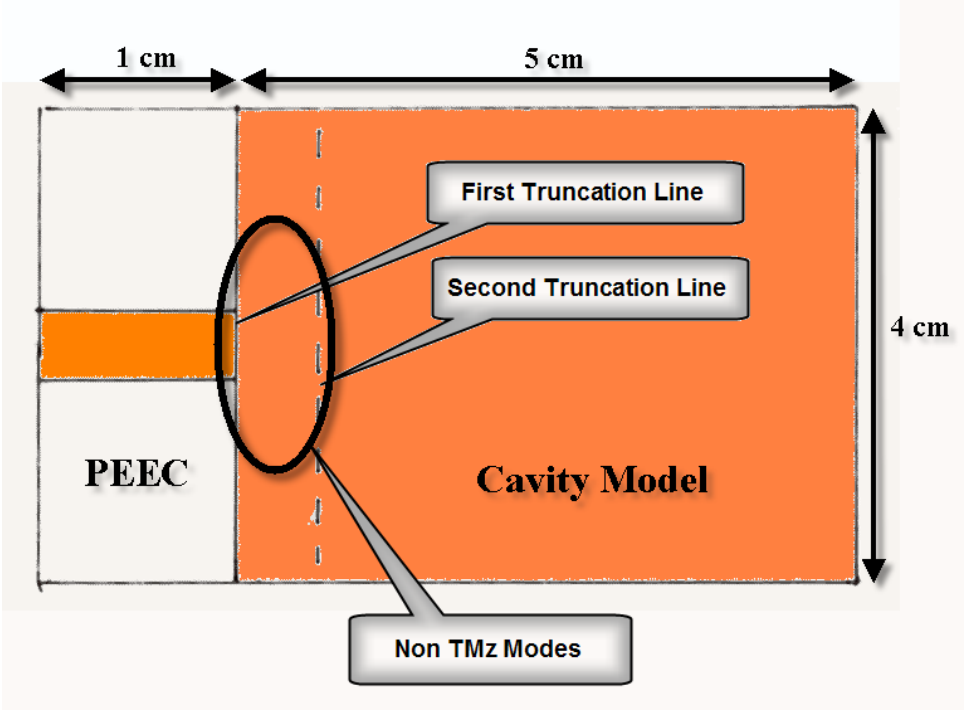

Figure 5.1 A trace-fed cavity with the model split at two different points, once at the trace end and the other on the patch

with volume cells. The trace is also modeled with volume cells. The ports connecting the cavity model to the PEEC model are only present at the end of the trace. This leaves the rest of the return plane on the PEEC model disconnected from the cavity, which is not ideal.

For the second model, the break between the PEEC model and the cavity model is made on the patch rather than at the trace-patch interface. The cavity model is valid where TM_z fields dominate. The models should be connected where both have a nearly pure TM_z field distribution. Then, the tangential fields should theoretically match.

The models were combined 1 cm past the end of the trace. This location was chosen after viewing the tangential E-field components calculated in HFSS and shown in Figure 5.2. Provided

$$\sqrt{|E_x|^2 + |E_y|^2} \ll |E_z| \tag{5.1}$$

is satisfied over the whole cavity region, the model division should be valid. The hybrid model setup is shown in Figure 5.3.

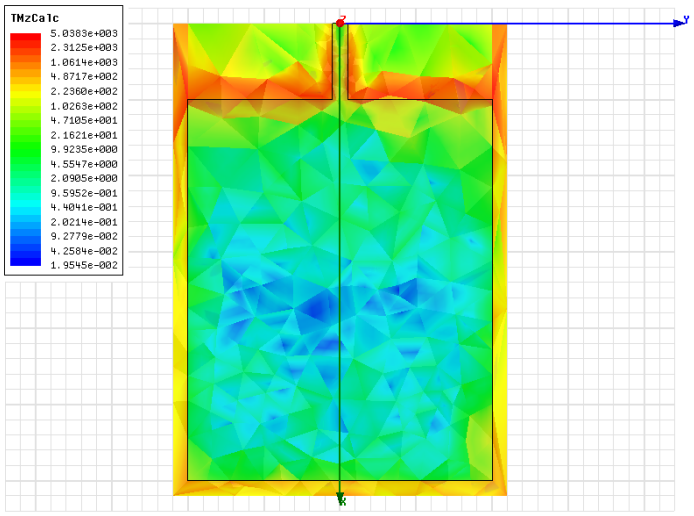

Figure 5.2 The tangential E-fields plotted in HFSS

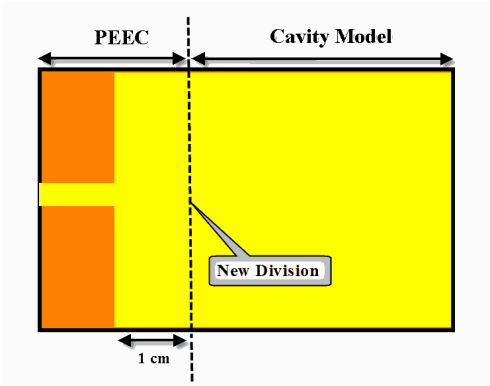

Figure 5.3 The division between the PEEC and cavity models on the patch

The two connection schemes were simulated and S_{11} calculated from 0.1 GHz to 2.5 GHz. The $|S_{11}|$ from both models and an HFSS model are shown in Figure 5.4. Hybrid 1 denotes the model with a PEEC model for the trace only. This model is matches the HFSS results at most of the resonance points. Hybrid 2 denotes a PEEC model for the trace and 1 cm of the patch and cavity for the remaining patch. This model has multiple resonances close to single resonances of the HFSS and Hybrid 1 models. The Hybrid 2 model has perhaps too few PEEC cells to be accurate. However, adding many more cells to the PEEC model will make it much more time and memory consuming. The main goal of a hybrid PEEC and cavity

method is accuracy and speed over other full-wave solution methods. Adding too many PEEC cells defeats that purpose.

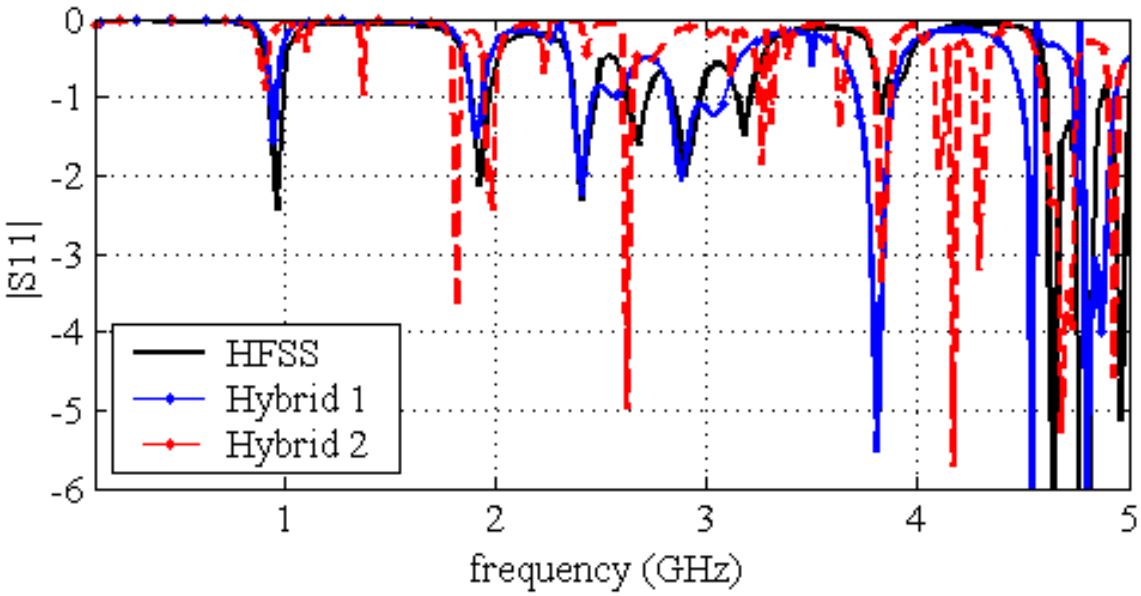

Figure 5.4 $|S_{11}|$ for a trace-fed cavity simulation plotted with simulations using the hybrid method and HFSS

5.2. VIA SHORTING TO A PLANE

The second problem considered is a 1.5-in by 1-in board with 20-mil plane spacing, pictured in Figure 5.5. A via shorting to the lower plane is positioned 125 mil in from the lower and left edge of the board. A 250-mil square section of the board is modeled by PEEC, shown in Figure 5.6. This problem could be simulated by a cavity model alone. However, the goal with this model is to combine the PEEC and cavity methods in a way that the same results are obtained as with the cavity model alone.

There are two differences in this model compared with the patch model. The coupling from the upper plane to the lower plane in the PEEC model has been removed. This is accomplished by setting up zones in the model such that PEEC cells only couple with other cells in their own or the immediately adjacent zone. Conducted

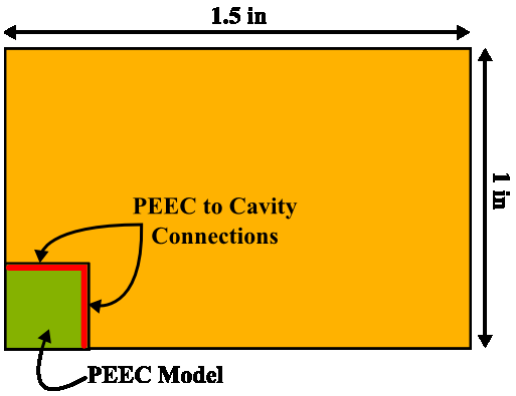

Figure 5.5 The PEEC model connected to the cavity model through ports along two adjacent sides

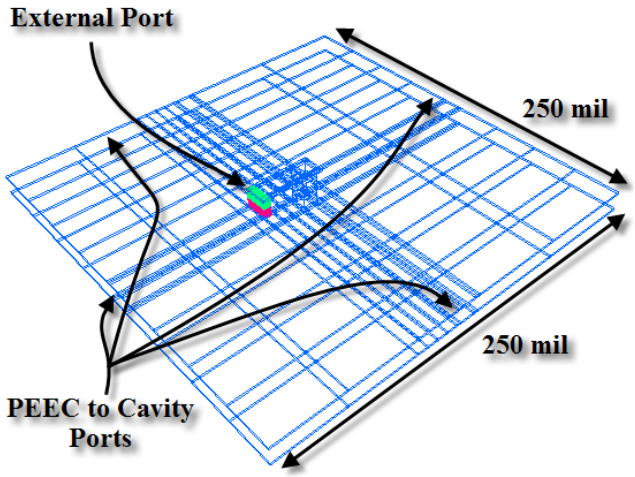

Figure 5.6 PEEC model for a via connecting a trace to the return planes

currents pass freely through the boundary, but the mutual partial potentials and the partial inductances are zero for the interactions between the upper plane and the lower plane. The via metal is between the two planes and allowed to couple to each. Thus, the parasitic inductance and capacitance of the via is still calculated in PEEC.

The cavity model is used to replace the missing couplings. Instead of segmenting the cavity, it is left in one piece, so that the space occupied by the PEEC model is also covered. At present it is believed but not verified that through the connections of

the two models, the cavity model satisfies the coupling that is removed. Experiments to verify whether this is true are still being considered.

The model was simulated for frequencies between 0.1 GHz and 5 GHz. S_{11} was calculated and is shown in Figure 5.7. In this model, the hybrid model almost exactly matches the cavity model. After this success a difficult problem was posed. This problem is considered in the next section.

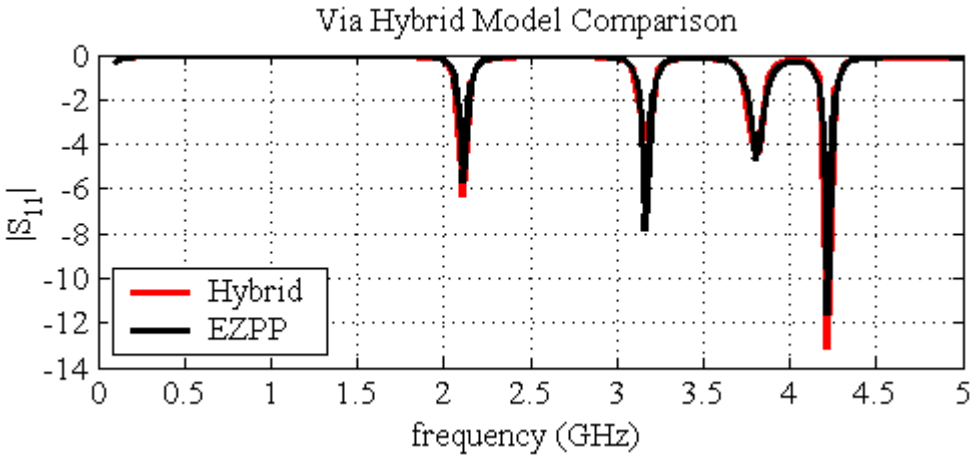

Figure 5.7 The S-parameter results for the hybrid model shown in Figure 5.6

5.3. VIA TRANSITION THROUGH A SHORTED CAVITY

A via passes completely through the two planes of the cavity in this problem. The DC return path is through a shorting pin on the other side of the board. This problem is again attempted with a PEEC model with all of its couplings in similar fashion with the method used on the patch in the first model.

The PEEC part of the model is shown in Figure 5.8. The PEEC portion spans the full width of the board and accounts for the end 200 mil of the length of the board. The shorting via is at the upper portion of the model, and a via connects port 1 to port 2 at the bottom of the figure. The model was simulated from 0.1 GHz to 5 GHz. S_{11} is shown in Figure 5.9. The resonances are all present in the hybrid model but the magnitude is high compared with the results from both CST Microwave Studio and Ansoft HFSS.

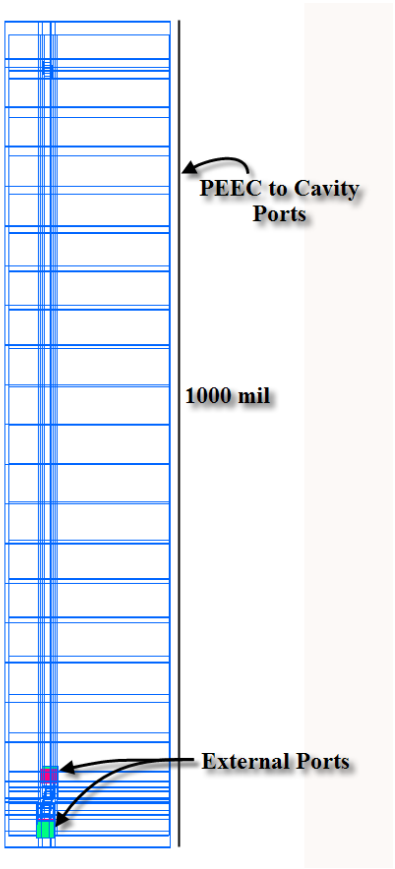

Figure 5.8 The PEEC portion of the hybrid model for a via transitioning through a shorted cavity

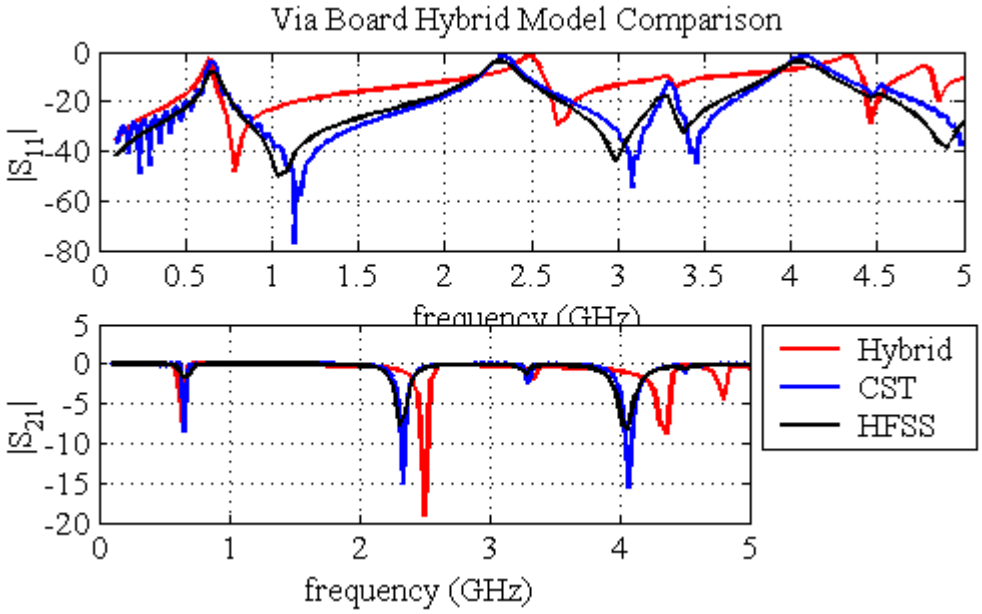

Figure 5.9 The S-parameter results for the hybrid model shown in Figure 5.8

The second PEEC model used for this problem is shown in Figure 5.10. The via in this model is positioned in the same location as the via in Figure 5.8, but the shorting via is handled by a SPICE model connected to the cavity model. Additionally, the PEEC to cavity connections are at the via instead of the edge of the model, and no coupling is allowed between the upper and lower planes in the PEEC model. The coupling terms are nonzero only when the cells are in the same or adjacent region of the model as in the hybrid model of the last section. Two hybrid traces are shown in Figure 5.11 and compared with MWS and HFSS. The first hybrid result in Figure 5.11 uses a very small resistance for the shorting via connection, and the second uses a 0.25 nH inductance. The result of the model using the inductance matches CST and HFSS well.

To be thorough, another hybrid model was generated with the same PEEC geometries, but the hybrid connections were made by a perimeter of 40 ports connecting the PEEC and cavity models. The same frequency range was simulated. The PEEC model was divided into three zones. One zone includes everything below the cavity dielectric. The second zone includes only the via cells. The third zone includes cells above the cavity dielectric. The results for the simulations of this model are shown in Figure 5.12. Hybrid 1 allows coupling only between cells in the same zone in the PEEC model. Hybrid 2 also allows coupling between cells in adjacent zones. The coupling from adjacent zones retains the effects of capacitive coupling from the via to the planes, which is not accounted for in any way in the cavity model. The two hybrid models deviate from one another slightly through the calculation band, but both agree well with the results from HFSS and MWS.

5.4. SUMMARY AND CONCLUSIONS

Two approaches to creating hybrid PEEC and cavity model simulations were tried. The first approach on a trace-fed patch antenna failed to match the results of other simulators. It is unknown why this approach failed when a more complicated and less understood approach succeeded. One possible cause may be a coarse PEEC mesh. The second approach used PEEC models with some of their coupling elements removed. The removed coupling is assumed to be compensated by the cavity model, but the physics of the interaction are not fully understood. Experiments to verify the effects of combining the two methods in this fashion are still being considered.

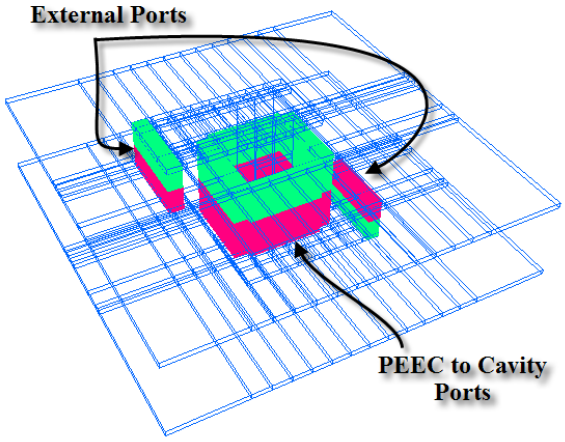

Figure 5.10 The second PEEC model used for the via transitioning through a shorted cavity

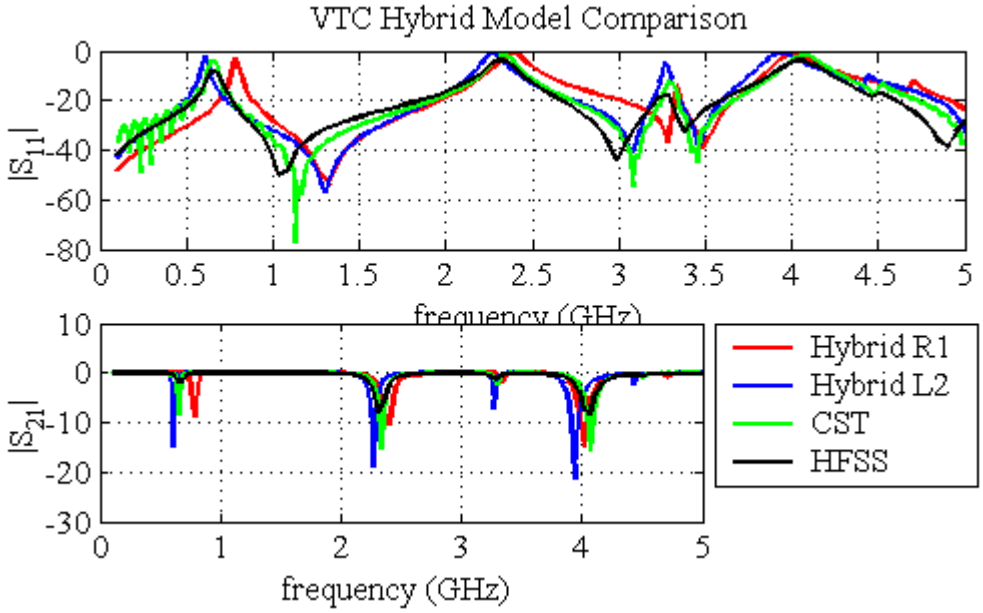

Figure 5.11 The S-parameter results for the hybrid model shown in Figure 5.10

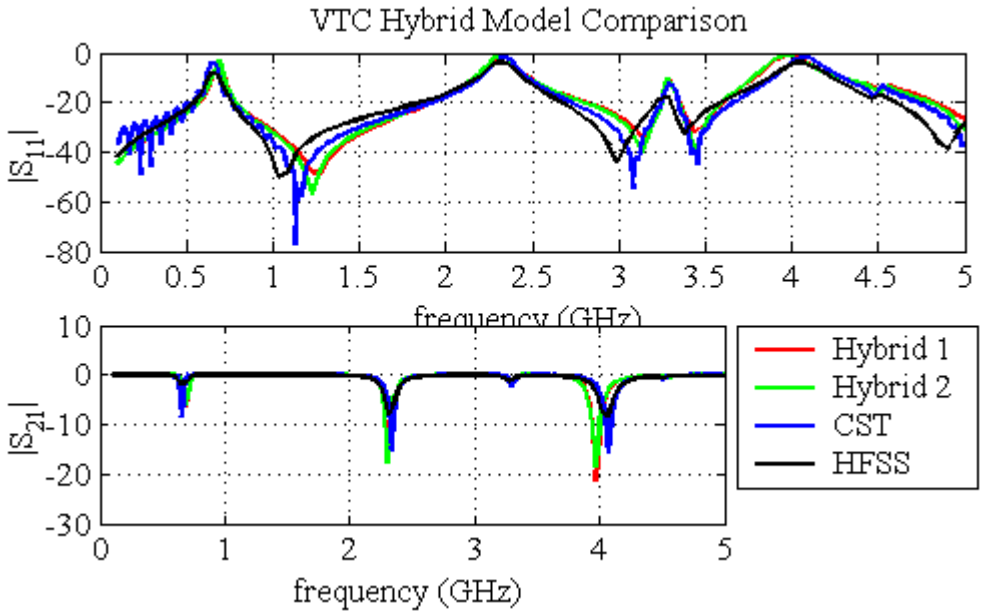

Figure 5.12 The model from Figure 5.10 altered for cavity connections at the edge of the model rather than at the via

6. THREE-DIMENSIONAL INTERCONNECT AND ANTENNA ANALYSIS USING A STATE-VARIABLE SOLUTION FOR PEEC, INCLUDING EXCESS CAPACITANCE

The PEEC method utilizes a two step process. First, the structure is discretized and partial parameters are calculated. Second, the partial parameters are organized into a netlist for a SPICE solution. Alternatively, the partial parameters can be used to formulate a state-variable model of the structure. Previous work has demonstrated power electronic applications of a state-variable formulation. However, those examples did not include a formulation for dielectrics. State-variable formulations without dielectrics and with dielectrics are both presented and tested on a microstrip and a cupped-ground ANSERLIN antenna.

6.1. STATE VARIABLE FORMULATION FOR PEEC

PEEC returns partial inductances and partial capacitances or their equivalent, as well as other circuit quantities. Often these circuit elements are used to construct SPICE models. In this section, a state variable formulation is derived using the partial parameter matrices.

6.1.1. State Variable Formulation without Excess Capacitances. The state variable formulation is straight forward when excess capacitances are excluded. This omits the possibility of dielectrics in the model. One matrix solution possible is

$$\begin{bmatrix} Z & \Gamma \\ -\Gamma^T & j\omega\gamma^T P^{-1}\gamma \end{bmatrix} \begin{bmatrix} I_L \\ V_C \end{bmatrix} = \begin{bmatrix} 0 \\ I_T \end{bmatrix} \tag{6.1}$$

This matrix is in general full. It can be solved by direct methods, and I have solved it with Gaussian elimination and partial pivoting both in serial and parallel codes in a slightly different form presented in an earlier section.

Decomposing the matrix solution into its block matrices yields two coupled matrix equations,

$$ZI_L + \Gamma V_C = 0 \tag{6.2}$$

$$-\Gamma^T I_L + j\omega\gamma^T P^{-1}\gamma V_C = I_T \ . \tag{6.3}$$

Both equations are frequency domain relations, but the time domain version is

$$Ri_L(t) + L\dot{i}_L(t) + \Gamma v_c(t) = 0 \tag{6.4}$$

$$-\Gamma^T i_L(t) + \gamma^T P^{-1}\gamma \dot{v}_C(t) = i_T(t)\ . \tag{6.5}$$

The state variables in the formulation are the inductor currents, i_L, and the capacitor voltages, v_C. Solving for the first order derivatives of the state variables yields

$$\dot{i}_L(t) = -L^{-1}Ri_L(t) + -L^{-1}\Gamma v_C(t) \tag{6.6}$$

$$\dot{v}_C(t) = (\gamma^T P^{-1}\gamma)^{-1}\Gamma^T i_L(t) + (\gamma^T P^{-1}\gamma)^{-1} i_T(t) \tag{6.7}$$

Then, the state variable equation is

$$\begin{bmatrix} \dot{v}_C(t) \\ \dot{i}_L(t) \end{bmatrix} = \begin{bmatrix} 0 & (\gamma^T P^{-1}\gamma)^{-1}\Gamma^T \\ -L^{-1}\Gamma & -L^{-1}R \end{bmatrix} \begin{bmatrix} v_C(t) \\ i_L(t) \end{bmatrix} + \begin{bmatrix} (\gamma^T P^{-1}\gamma)^{-1} \\ 0 \end{bmatrix} i_T(t) \tag{6.8}$$

The output equation is then just the difference in the potential states associated with the port nodes, assuming that the output is the port voltages. The input along this whole development is the terminal or port currents induced.

$$v_{Ports}(t) = \begin{bmatrix} \varepsilon & 0 \end{bmatrix} \begin{bmatrix} v_C(t) \\ i_L(t) \end{bmatrix} + \begin{bmatrix} 0 \end{bmatrix} i_T(t) \tag{6.9}$$

where ε is a connectivity matrix of 1 and -1 entries describing the port connection to the nodes.

6.1.2. State Variable Formulation using Sources and Terminations with Z_o Impedance. This formulation combines the ideas of the last section and with the controlled impedance sources described in Section 3.3.1. Use the port equation

$$v_m(t) - v_n(t) + Z_o\lambda = v_s(t) \tag{6.10}$$

where m marks the positive node, n marks the negative node, λ is the port current into the m node, and v_s is the port voltage. Unlike in the frequency domain, to get a state equation model, it is easier to work the constraint directly into the equations. Solving for λ,

$$\lambda = \frac{1}{Z_o}v_n - \frac{1}{Z_o}v_m + \frac{1}{Z_o}v_s \tag{6.11}$$

A port connectivity matrix, A, is required to include these expressions in the overall matrix solution.

$$A = \begin{bmatrix} 0 & 1 & 0 & -1 & 0 & \cdots \\ 1 & 0 & -1 & 0 & 0 & \cdots \end{bmatrix} \tag{6.12}$$

The A matrix is Q by N, where Q is the number of ports. The 1 entry in each row marks the connection to the positive node, and the -1 entry marks the negative node connection.

Consider λ as a vector of the port currents.

$$\lambda = \frac{1}{Z_o}(-Av_c + v_s) \tag{6.13}$$

Then, the currents can be added into the KCL state equations used in the the previous sections.

$$(\gamma^T P^{-1}\gamma)\dot{v}_c - \Gamma^T i_L - A^T\lambda = i_T \tag{6.14}$$

and

$$\dot{v}_c = (\gamma^T P^{-1}\gamma)^{-1}\left[\Gamma^T i_L - \frac{1}{Z_o}A^T A v_c + \frac{1}{Z_o}A v_s\right] \tag{6.15}$$

Then, the new state equation is

$$\begin{bmatrix} \dot{v}_C(t) \\ \dot{i}_L(t) \end{bmatrix} = \begin{bmatrix} \frac{-1}{Z_o}(\gamma^T P^{-1}\gamma)^{-1}A^T A & (\gamma^T P^{-1}\gamma)^{-1}\Gamma^T \\ -L^{-1}\Gamma & -L^{-1}R \end{bmatrix} \begin{bmatrix} v_C(t) \\ i_L(t) \end{bmatrix} + \begin{bmatrix} \frac{1}{Z_o}(\gamma^T P^{-1}\gamma)^{-1}A^T & (\gamma^T P^{-1}\gamma)^{-1} \\ 0 & 0 \end{bmatrix} \begin{bmatrix} v_s(t) \\ i_T(t) \end{bmatrix} \tag{6.16}$$

6.1.3. State Variable Formulation Including Excess Capacitance. The essential addition in adding excess capacitance into a state variable formulation is recognizing that it can be included as yet another set of state variables. The definition of excess capacitance is given in [28]. Previously, there was a inductive current state and a capacitive node voltage state. The excess capacitance effectively adds a series capacitance between nodes.

Neglecting any incident electric field, the field equation is

$$0 = \vec{E}(r,t) + \frac{\partial \vec{A}(r,t)}{\partial t} + \nabla\Phi(r,t) \tag{6.17}$$

For a conductor, the total electric field would be replaced by a current divided by the conductivity of the conductor. After integration and discretization, the electric field

term is reduced to a potential over the body of the cell of interest. Label that voltage $v_{C^+{}_\alpha}$ to represent the voltage drop in the direction of the current cell α. Ignore mutual inductance terms on cell α for now, and the KVL expression becomes

$$\phi_i - \phi_j = L\dot{i}_{L_\alpha} + v_{C^+{}_\alpha} \tag{6.18}$$

and $v_{C^+{}_\alpha}$ is further governed by equation

$$C^+_\alpha \dot{v}_{C^+{}_\alpha} = i_{L_\alpha} \tag{6.19}$$

where C^+_α is the excess capacitance of α. In Equation 6.18 the ϕ's are the node voltages of nodes i and j to which α connects. The notation ϕ is used to distinguish the node voltage states from the excess capacitance voltage states.

Assume that every cell is a dielectric cell, and introduce v_{C^+} as a new vector of state voltages for the excess capacitances. Equations 6.18 and 6.19 become

$$L\dot{i}_L + I v_{C^+} + \Gamma\phi = 0 \tag{6.20}$$

$$C^+ \dot{v}_{C^+} = i_L \ , \tag{6.21}$$

where I is the identity matrix. Combining these two equations with the KCL expression,

$$-\Gamma^T i_L + \gamma^T P^{-1} \gamma \dot{\phi} = i_T \ , \tag{6.22}$$

a new state matrix is constructed

$$\begin{bmatrix} \dot{i}_L \\ \dot{v}_{C^+} \\ \dot{\phi} \end{bmatrix} = \begin{bmatrix} 0 & -L^{-1} & -L^{-1}\Gamma \\ (C^+)^{-1} & 0 & 0 \\ (\gamma^T P^{-1}\gamma)^{-1}\Gamma^T & 0 & 0 \end{bmatrix} \begin{bmatrix} i_L \\ v_{C^+} \\ \phi \end{bmatrix} + \begin{bmatrix} 0 \\ 0 \\ (\gamma^T P^{-1}\gamma)^{-1} \end{bmatrix} i_T \ . \tag{6.23}$$

At this point there are no losses built into the system, and any models would likely be only marginally stable. Adding resistance into the formulation will introduce the loss to damp the response.

Without resistances the circuit branch for a dielectric cell is an inductance in line with a capacitor, connecting to two potential nodes. The PEEC derivation leaves some ambiguity as to how a lossy dielectric might be represented with a combination of a resistance and a capacitor. It appears that they should be connected in series. However, the entries in the resistance and excess capacitance matrices must be disjoint for that formulation to work. A more detailed development of the integral equation

will show that the excess capacitance and the resistance are in parallel with the inductance in series with the pair.

Expanding the $\vec{A}(\vec{r})$ term in (6.17) yields

$$\vec{E}(r) = -\frac{\partial}{\partial t}\left\{\mu_o \int_{V'} G(r,r')\left(\vec{J}_c(r') + \varepsilon_o(\varepsilon_r - 1)\frac{\partial \vec{E}(r')}{\partial t}\right) dV(r')\right\} - \nabla\Phi(r)\ . \quad (6.24)$$

The electric field term is again v_{C^+}, and the KVL equation is the same as in (6.18). Not all of the current passing through the inductance also passes through the capacitance. Therefore, (6.19) is not valid when resistive losses coincide with dielectrics. Current is contributed by both the resistance and the capacitance. Therefore,

$$C^+\dot{v}_C = i_L - \frac{1}{R}v_C\ , \quad (6.25)$$

which includes some loss to add stability to the system.

In matrix form complications arise, and another connectivity matrix is defined in order to map the inductive currents onto the excess capacitance voltages. Call this matrix T. In addition, leave the R matrix as it was, a diagonal matrix that has nonzero entries only on pure conductor cells. Then, the KVL expression in matrix form becomes

$$L\dot{i}_L + T^T v_{C^+} + \Gamma\phi + Ri_L = 0 \quad (6.26)$$

Introduce a new matrix G to contain any conductance losses in the dielectric cells. Write the new excess capacitance relation

$$C^+\dot{v}_{C^+} = Ti_L - Gv_{C^+} \quad (6.27)$$

where G is diagonal. Finally, the new state matrix expression is

$$\begin{bmatrix} \dot{i}_L \\ \dot{v}_{C^+} \\ \dot{\phi} \end{bmatrix} = \begin{bmatrix} -L^{-1}R & -L^{-1}T^T & -L^{-1}\Gamma \\ (C^+)^{-1}T & -G & 0 \\ \left(\gamma^T P^{-1}\gamma\right)^{-1}\Gamma^T & 0 & 0 \end{bmatrix} \begin{bmatrix} i_L \\ v_{C^+} \\ \phi \end{bmatrix} + \begin{bmatrix} 0 \\ 0 \\ \left(\gamma^T P^{-1}\gamma\right)^{-1} \end{bmatrix} i_T \quad (6.28)$$

6.2. TIME-DOMAIN SIMULATIONS

A microstrip model was constructed to test the time domain state-variable formulation. A trapezoidal integration method was used on the state-variable PEEC

formulation to calculate the time domain waveforms. The comparisons were calculated with an length transmission line in SPICE. The SPICE model used ideal short and open conditions, where as the PEEC model automatically includes via inductance and stub capacitances. To short the model in PEEC, a section of the dielectric was recast as a conductor to form a shorting via through the substrate. Figure 6.1 shows the view of the microstrip model. Figure 6.2 and Figure 6.3 both show responses to a pulse with a 20-ps rise time. Figure 6.4 shows the response to a pulse with a 2-ps rise time.

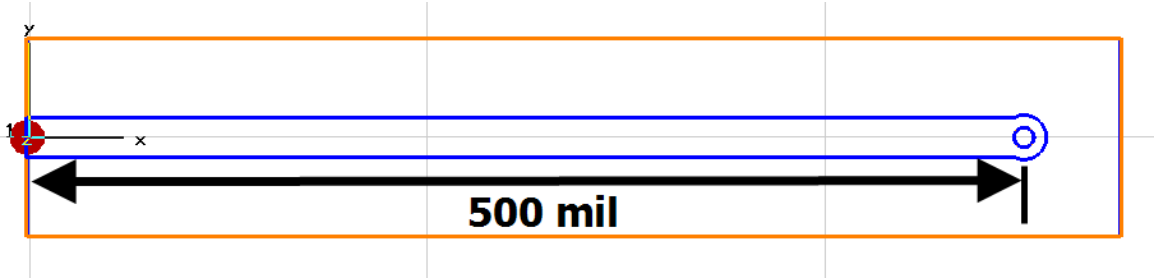

Figure 6.1 A top view of the shorted microstrip structure

For a second experiment a similar trapezoidal integration code was used to simulate a pulse at the feed of the cupped-ground ANSERLIN antenna shown in Figure 6.5. The PEEC simulations are compared with time domain simulations from Microwave Studio in Figure 6.6 and Figure 6.7.

6.3. CONCLUSIONS

A state-variable model with or without dielectrics can be used effectively for simulating transmission lines in the presence of dielectric. However, thick dielectrics like those required for small-scale ANSERLIN antennas are not gridded fine enough to simulate in this manner. Additionally, delays are realizable in the state-variable simulations, but these delays may need filtering to maintain stability.

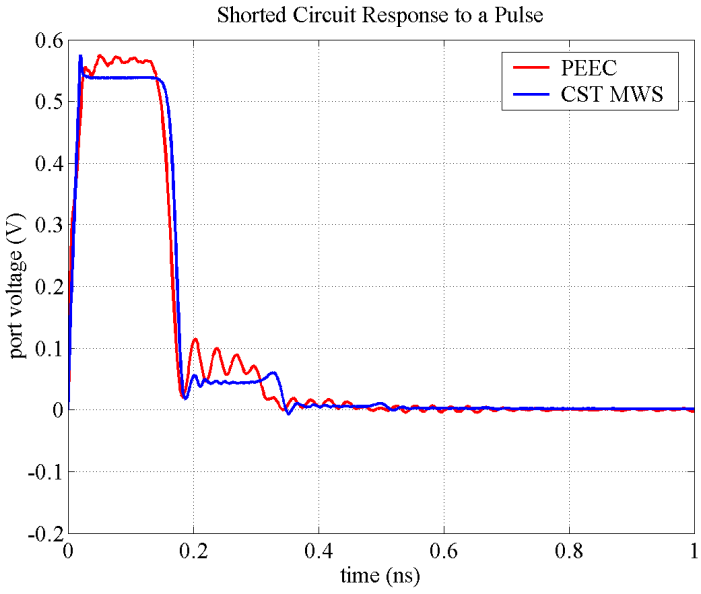

Figure 6.2 Response of a shorted microstrip to a pulse with a 20 ps rise time

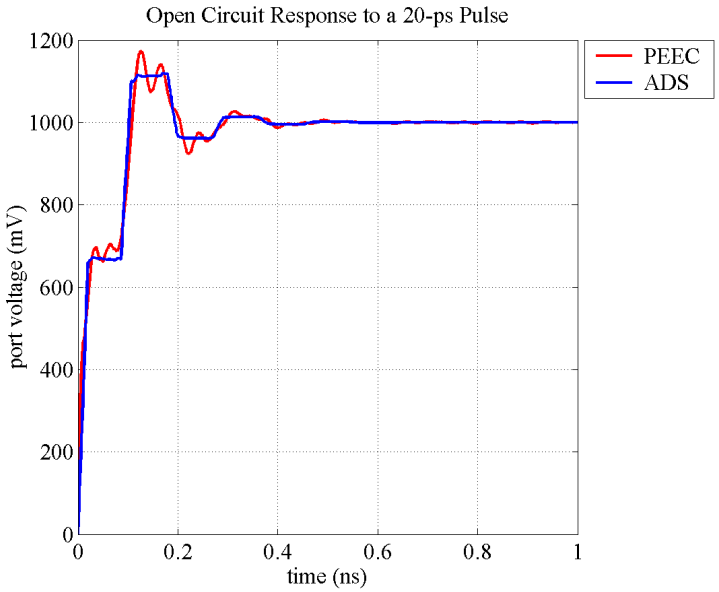

Figure 6.3 Response of an open-ended microstrip to a pulse with a 20 ps rise time

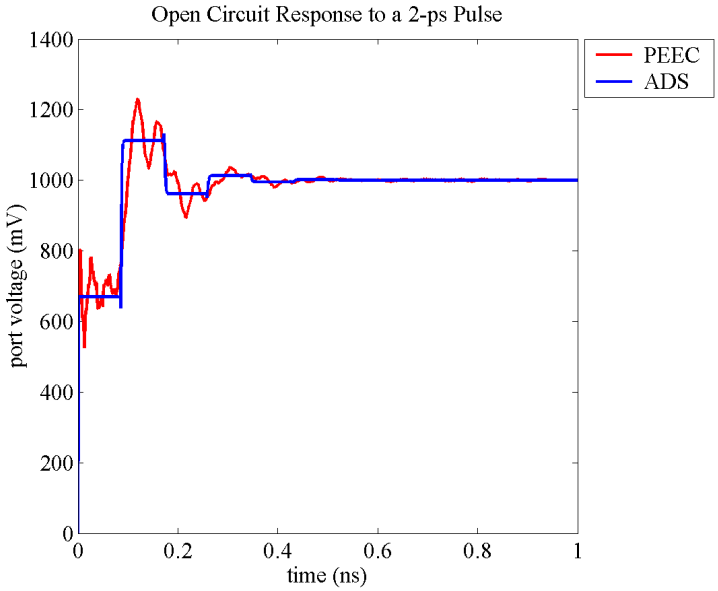

Figure 6.4 Response of an open-ended microstrip to a pulse with a 2 ps rise time

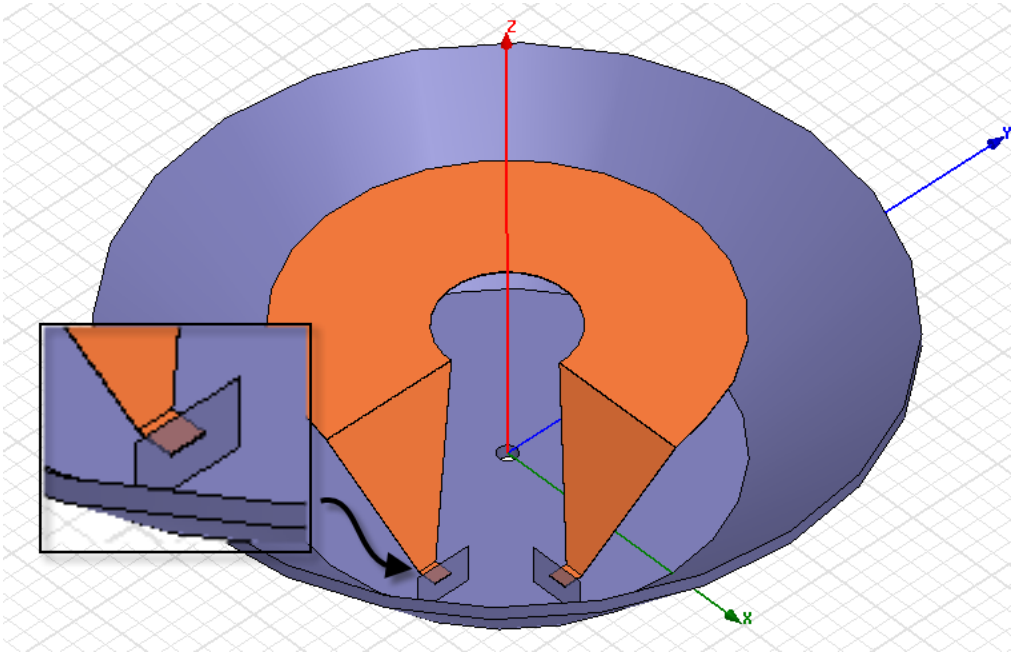

Figure 6.5 A cupped-ground version of the ANSERLIN antenna, shown here without its dielectrics

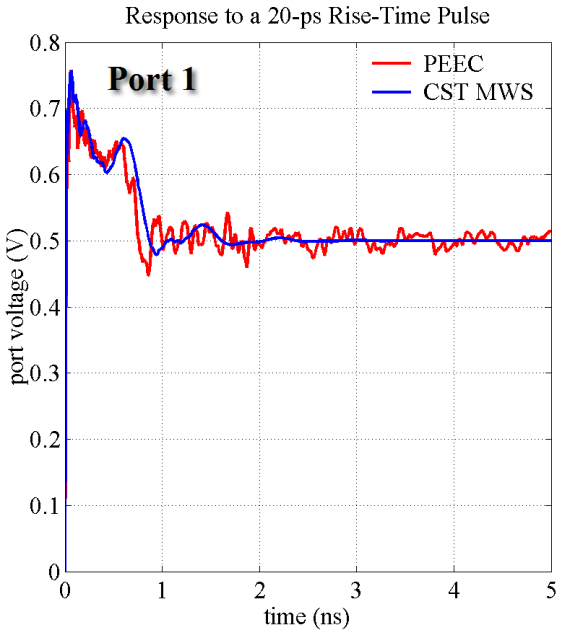

Figure 6.6 TDR (Port 1) result for a cupped-ground ANSERLIN without dielectrics

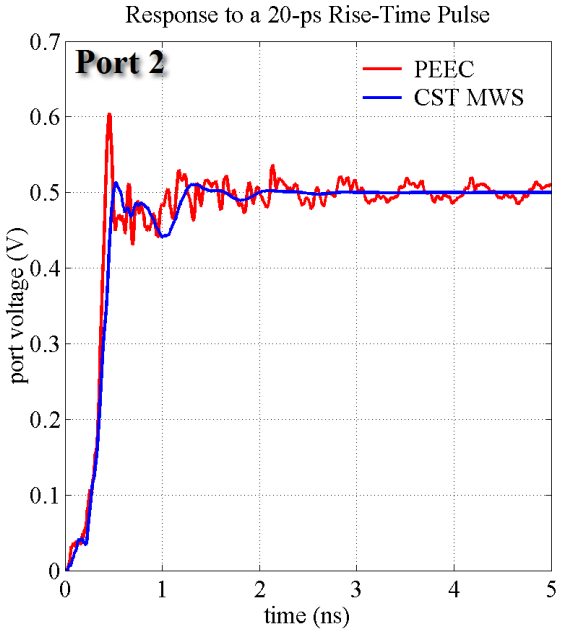

Figure 6.7 TDT (Port 2) result cupped-ground ANSERLIN without dielectrics

7. ADAPTIVE MESHING WITH A LOCAL EQUIDISTANCING TO REDUCE TRUNCATION ERROR IN PEEC FORMULATIONS SCATTERING AND INTERCONNECT PROBLEMS

The number of unknowns available for PEEC models is limited due to the memory and time constraints associated with the full matrices that are produced. For that reason, it is essential to utilize those unknowns available efficiently. Grid generating has numerous approaches that may be applied to generate grids conforming to a physical model. Elliptical and other partial differential equation based gridding methods can provide smooth uniform grids, but preparing forcing functions to control the grid density is difficult [12]. Another method called equidistribution was chosen instead due to the degree of control it allows over mesh spacing. Equidistribution is typically a 1D method by which the variation in the output parameter over length is distributed evenly among the unknowns of the model [30]. The higher dimensional equivalent of this method is best applied in a local, iterative fashion. Field calculations from initial PEEC calculations are used with a local equidistribution approach to divide field or current gradients evenly among the current and charge cells of the PEEC model.

In addition to the grid refining aspects of this section derviations for the field calculations required for the grid refining are given. These field calculations are based on the hexahedral gridding system used elsewhere in this thesis.

7.1. LOCAL EQUIDISTRIBUTION FOR 1D AND 2D GRID REFINEMENT

Equidistribution as a 1D method is a process of balancing a arbitrary monitor function across the divisions of a line. In integral terms the criterion to be met is given by

$$\int_{x_{i-1}}^{x_i} m(u)dx = \int_{x_i}^{x_{i+1}} m(u)dx = c \;\forall\; 2 \leq i \leq N-1 \;, \tag{7.1}$$

where $m(u)$ is the monitor function over the solution $u(x)$. The criterion in (7.1) ensures that $m(u)$ is equally distributed over the grid divisions. For this section the arc length of $u(x)$,

$$m(u) = \sqrt{1 + \|u_x\|^2} \;, \tag{7.2}$$

is chosen for the monitor function. While equidistribution is a 1D approach, there are some 2D approximations to the method that differ from 1D original approach,

which had issues with overlapping grid components. This method may described as a local equidistributional method.

The 1D equidistibution method is exact. Once the monitor function is known over the line, the new grid divisions are found by closed-form expressions. However, the 2D local equidistribution method considers only the adjacent points. Thus, the local method will require more than one pass through the grid to distribute the points. For the 2D method each interior grid point will have eight surrounding grid points, as shown in Figure 7.1. Let $s_{mn,ij}$ represent the weight function for the equidistribution, described by

$$s_{mn,ij} = \sqrt{K\left(\frac{|\vec{r}_{mn} - \vec{r}ij|}{\max|\vec{r}_{mn} - \vec{r}ij|}\right)^2 + \left(\frac{|\vec{E}_{mn} - \vec{E}_{ij}|}{\max|\vec{E}_{mn} - \vec{E}_{ij}|}\right)^2} \tag{7.3}$$

for $m \in \{i-1, i, i+1\}$ and $n \in \{j-1, j, j+1\}$ but not $(m,n) = (i,j)$. K is an adjustment factor typically between 0 and 1 that determines whether the distance or the field dominates the grid density. A balance of the two is sought. K typically depends on the application. The weight function above uses the change in electric field to indicate the truncation error in present grid. The goal of the equidistribution is that the change in the electric field per distance between points be the same uniformly throughout the grid. Thus, the grid unknowns are better utilized where high field gradients exist. The electric field is only chosen as an example; the magnetic field or the current is an equally good choice.

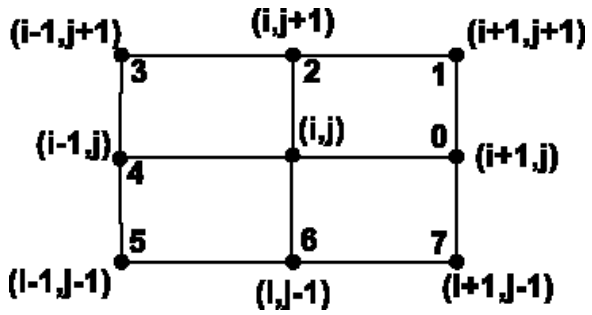

Figure 7.1 Eight neighbor points surrounding an interior grid point

To find the new location for $\vec{r}_{ij}$, renumber the $s_{mn,ij}$ according to the neighbor point locations in Figure 7.1. So, $s_{mn,ij} \rightarrow s_{l,ij}$. Let $S_{ij} = \sum_{l=0}^{7} s_{l,ij}$, and let

$$\lambda_{l,ij} = \frac{s_l}{S_{ij}} \, . \tag{7.4}$$

Assuming that the eight points make a convex polygon, the new location of the center grid point can be described

$$\vec{r}_{ij}^{\,n+1} = \sum_{l=0}^{7} \lambda_{l,ij} \vec{r}_l^{\,n} \, . \tag{7.5}$$

Once the new value is set, the field components associated with the old grid location are no longer valid. Recalculating the fields after each grid change is unfeasible. Instead a 2D Lagrangian interpolation is used to estimate the field using the fields of the neighbor points.

Mesh entanglement can occur after one or more iterations. Mesh entanglement is a state when grid points are positioned such that grid lines cross. Figure 7.2 shows a case of mesh entanglement along with a legal grid movement. Two conditions combine to cause mesh entanglement. First, the bounding polygon formed by the neighbor points will not be convex. Second, the $s_{l,ij}$ value associated with one of the points will be much larger those of the other points. The center point will be drawn to the dominant point so that it lies outside of the bounding polygon. The 2D algorithm seldom recovers after a mesh entanglement occurs. Typically, the shift causes a cascade of further entanglements.

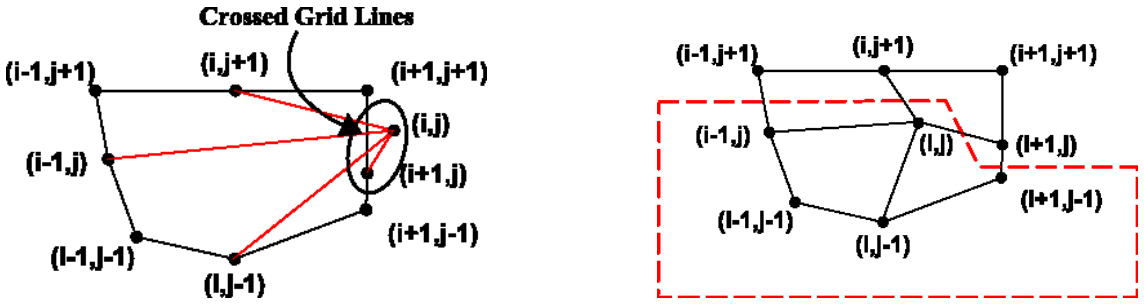

(a) Mesh entanglement

(b) Legitimate grid movement

Figure 7.2 Shifting of a grid point during a step of the local equidistribution

In order to avoid mesh entanglement, a damping effect has been added, reducing the amount of shifting each point can take in each iteration. Also, rather than using the global coordinates the local coordinate system is used in the shifting. Local coordinates make it easier to check for grid errors since in local coordinates, $a_{i,j} < a_{i+1,j}$ for all points. This fact cannot be said for global coordinates where a curving shape has no such ordering in the xy plane. Let q represent either a or b, and let $\hat{q}^{n+1}$ represent the new grid point from my previous formulation, defined by

$$\hat{q}^{n+1} = \sum_k S_k^n q_k^n + \sum_l S_l^{n+1} q_l^{n+1} \ . \tag{7.6}$$

The first term accounts for neighbors that have not moved yet, and the second terms accounts for the neighbors that have moved previously in this iteration. The previously shifted neighbor points are with the red dotted line in Figure 7.2(b). Let the total change in q be defined by subtracting q^n from the previous expression.

$$dq^{n+1} = \hat{q}^{n+1} - q^n = \left[\sum_k S_k^n q_k^n + \sum_l S_l^{n+1} q_l^{n+1} \right] - q^n \ . \tag{7.7}$$

Then, let γ represent the fractional distance that the grid point will actually travel. The new point will be at

$$\begin{aligned} q^{n+1} &= \gamma dq^{n+1} + q^n \\ &= \gamma \left[\sum_k S_k^n q_k^n + \sum_l S_l^{n+1} q_l^{n+1} \right] + (1-\gamma) q^n \ , \end{aligned} \tag{7.8}$$

where $\gamma \in [0, 1]$. A good working choice is $\gamma = 0.1$.

Despite careful preparation of the method, the 2D local equidistribution method still fails in some cases. For example, a PEEC model driven at one port has very large gradients surrounding the port and much lower gradients elsewhere. The cells around the port typically get distorted such that later integrations of the partial parameters are not accurate. This method works well, however, for scattering from plates. An example of a scattering plate is given in Section 7.3. This sort of grid refining may also work well for interference problems with some experimentation.

Iteratively solving a complex PEEC problem is prohibitive in most cases. The reason for solving the PEEC problem prior to refining the grid is to generate fields to act as weighting functions for the refinement. Using these fields poses a few practical problems. The fields are based off a particular excitation of the model ports. For

an antenna, this is typical for operation. However, exciting one port with a pair of coupled microstrip lines leads to high field gradients around the source line and low gradients around the target line, where fine gridding is also needed. Additionally, standing wave patterns cause nonuniform gridding along lines which is frequency specific.

A method for avoiding these issues is defining a weighting function based on the geometry itself. Fields will tend to be more intense around the edges of the conducting bodies. Therefore, the grid points at the edge of objects are treated like source points generating fictitious fields. The fictitious fields may take the form of a Gaussian pulse like

$$P(\vec{r}) = \sum_i e^{|\vec{r}-\vec{r}_i|^2/(2\sigma^2)} \ , \tag{7.9}$$

or offset $1/R$ type expressions like

$$P(\vec{r}) = \frac{1}{R + R_0} \ , \tag{7.10}$$

where R_0 is selected greater than zero and large enough to avoid sharp gradients near other objects. Instead of summing over the grid points of the body, which has mixed results for nonuniform grids, the weighting functions could be integrated over the outer surface of the object.

7.2. SCATTERED FIELD CALCULATIONS

The PEEC method handles impressed, or incident, electric fields by treating them as voltage sources [24]. These impressed fields and other impressed lumped sources combined with the boundary conditions of the conductors and dielectrics of the models lead to scattered currents and potentials. These scattered currents and potentials are the unknowns of the PEEC formulation. This section presents derivations associated with calculating the scattered fields from the unknowns, assuming a nonorthogonal hexahedral cell type.

7.2.1. Common Components of the Scattered Fields. A few quantities occur commonly among the field calculations and are derived here for reference in later sections. Summation notation of the form

$$x^n a_n = \sum_n x_n a_n \tag{7.11}$$

is used to keep the derivations more compact. Summation is implied if a superscript and subscript of the same index coincide in a term.

The gradient of the source and observation point distance, R, is found in most of the following expressions. Let $\vec{R} = \vec{r} - \vec{r}\,'$, and find the gradient of $R = |\vec{R}|$. First, note that the gradient acts on the unprimed coordinates with loss of generality let $\vec{r}\,' = \vec{0}$. Then, $\vec{R} \to \vec{r}$, and

$$\begin{aligned} \nabla r &= \nabla\sqrt{\vec{r}\cdot\vec{r}} \\ &= \hat{\mathbf{x}}^n \nabla_n \sqrt{x^m x_m} \\ &= \hat{\mathbf{x}}^n \left(\frac{1}{2}\right) \left[x^m \nabla_n x_m + x_m \nabla_n x^m\right] / \sqrt{x^m x_m} \ . \end{aligned}$$

Use the metric tensor for cartesian coordinates, $g_{mj} = \delta_{mj}$, to change covariant components to contravariant components. Then,

$$\begin{aligned} \nabla r &= \hat{\mathbf{x}}^n \left(\frac{1}{2}\right) \left[x^m \delta_{mj} \nabla_n x^j + x_m \nabla_n x^m\right] / r \\ &= \hat{\mathbf{x}}^n \left(\frac{1}{2}\right) \left[x^m \delta_{mj} \delta_n^j + x_m \delta_n^m\right] / r \\ &= \hat{\mathbf{x}}^n x_n / r \ , \end{aligned}$$

and the final result is

$$\nabla r = \frac{\vec{r}}{r} \tag{7.12}$$

after summation. This result is invariant under translation, so that

$$\nabla R = \frac{\vec{r} - \vec{r}\,'}{|\vec{r} - \vec{r}\,'|} \ . \tag{7.13}$$

Another useful result is

$$\begin{aligned} \nabla\vec{r} = \hat{\mathbf{x}}^m \nabla_m \hat{\mathbf{x}}_n x^n &= \hat{\mathbf{x}}^m \hat{\mathbf{x}}_n \delta_m{}^n \\ &= \hat{\mathbf{x}}^m \hat{\mathbf{x}}_m \end{aligned} \tag{7.14}$$

with the sum implied in the last result.

The free-space Green's function is defined as

$$G(\vec{r}, \vec{r}\,') = \frac{e^{-jk|\vec{r} - \vec{r}\,'|}}{4\pi|\vec{r} - \vec{r}\,'|} \ . \tag{7.15}$$

Let $R = |\vec{r} - \vec{r}\,'|$ and $G(\vec{r}, \vec{r}\,') \rightarrow G(R)$ to simply the following expressions. Take the gradient of the Green's function as

$$\begin{aligned}
\nabla G(R) &= \frac{e^{-jkR}}{4\pi} \nabla \left(R^{-1}\right) + \frac{1}{4\pi R} \nabla e^{-jkR} \\
&= \frac{e^{-jkR}}{4\pi} \left(-R^{-2} \nabla R\right) + \frac{1}{4\pi R} \left((-jk) e^{-jkR} \nabla R\right) \\
&= -\frac{e^{-jkR}}{4\pi R^2} \left(1 + jkR\right) \nabla R \, ,
\end{aligned}$$

and after simplification and letting $R \rightarrow |\vec{r} - \vec{r}\,'|$, the result is

$$\nabla G(\vec{r}, \vec{r}\,') = -\frac{e^{-jk|\vec{r} - \vec{r}\,'|}}{4\pi |\vec{r} - \vec{r}\,'|^3} \left(1 + jk|\vec{r} - \vec{r}\,'|\right) (\vec{r} - \vec{r}\,') \, . \tag{7.16}$$

The Hessian is a second order tensor. Let $\vec{r}\,' = \vec{0}$ without loss of generality, and start the derivation with

$$\nabla \nabla G(r) = \nabla (\nabla G(r)) \, .$$

The term in parathesis is the gradient given in (7.16). So, the first gradient operator is dispatched immediately. Then,

$$\begin{aligned}
\nabla \nabla G(r) &= -\frac{e^{-jkr}}{4\pi r^3} \left(1 + jkr\right) \nabla \vec{r} - \frac{e^{-jkr}}{4\pi r^3} \vec{r} \nabla \left(1 + jkr\right) \\
&- \frac{e^{-jkr}}{4\pi} \left(1 + jkr\right) \vec{r} \nabla r^{-3} - \frac{1}{4\pi r^3} \left(1 + jkr\right) \vec{r} \nabla e^{-jkr} \\
&= -\frac{e^{-jkr}}{4\pi r^3} \left(1 + jkr\right) \hat{\mathbf{x}}^m \hat{\mathbf{x}}_m - \frac{e^{-jkr}}{4\pi r^4} (jk) \vec{r}\vec{r} \\
&- \frac{e^{-jkr}}{4\pi} \left(1 + jkr\right) \vec{r} \left(-3 r^{-5} \vec{r}\right) - \frac{1}{4\pi r^3} \left(1 + jkr\right) \vec{r} \left((-jk) e^{-jkr} \vec{r}/r\right) \\
&= \frac{e^{-jkr}}{4\pi} \left\{ -r^{-3} \left(1 + jkr\right) \hat{\mathbf{x}}^m \hat{\mathbf{x}}_m - jkr^{-4} \vec{r}\vec{r} \right. \\
&\left. + 3 r^{-5} \left(1 + jkr\right) \vec{r}\vec{r} + jkr^{-4} \left(1 + jkr\right) \vec{r}\vec{r} \right\} \\
&= \frac{e^{-jkr}}{4\pi} \left\{ -r^{-3} \left(1 + jkr\right) \hat{\mathbf{x}}^m \hat{\mathbf{x}}_m + \left[(jk)^2 r^{-3} + 3 r^{-5} \left(1 + jkr\right) \right] \vec{r}\vec{r} \right\} \, .
\end{aligned} \tag{7.17}$$

The Hessian can be represented in matrix form as well. In that form the $\hat{\mathbf{x}}^m \hat{\mathbf{x}}_m$ term is only on the diagonal.

7.2.2. Near-Field Calculations. The near-field calculations all use the solution for the cell currents in order to make the calculations. Calculating the electric and magnetic fields requires operations on the vector magnetic field, which could be done numerically. However, for these operations finite differences are required. The

finite differences with a coarse mesh will be less accurate than a complete expression in terms of the currents. Therefore, all of the following derviations will be in terms of the cell currents. The derivations for the vector magnetic potential, the electric field, and the magnetic field follow.

The vector magnetic potential, $\vec{A}$, is present in all the following field calulations. So, the expression for $\vec{A}$ will be calculated followed by the derivations for some operations on the field. In Section 3.1 the current was discretized with

$$\vec{J}(\vec{r}) = \sum_n I_n \Pi_n(\vec{r}) \left(\frac{\frac{\partial \vec{r}}{\partial a_n}}{4\mathcal{J}_n} \right) . \tag{7.18}$$

This discretization will be used for the rest of the field derivations in Section 7.2.1. The Green's function solution for the vector magnetic potential is given as

$$\vec{A}(\vec{r}) = \int_V G(\vec{r}, \vec{r}\,')\mu_0 \vec{J}(\vec{r}\,')dV(\vec{r}\,') , \tag{7.19}$$

where V contains the full support of $\vec{J}(\vec{r}\,')$. After discretization the expression becomes

$$\vec{A}(\vec{r}) = \sum_n \frac{\mu_0 I_n}{4} \int_{-1}^{1}\int_{-1}^{1}\int_{-1}^{1} G(\vec{r}, \vec{r}\,') \frac{\partial \vec{r}\,'}{\partial a_n} da_n db_n dc_n , \tag{7.20}$$

where the 4 in the denominator in front of the equation is a scaling factor left after cancelling the Jacobian of $dV(\vec{r}\,')$.

The next quantity of interest with respect to $\vec{A}(\vec{r})$ is the curl, which is derived as

$$\begin{aligned} \nabla \times \vec{A}(\vec{r}) &= \sum_n \frac{\mu_0 I_n}{4} \int_{-1}^{1}\int_{-1}^{1}\int_{-1}^{1} \nabla \times \left(G(\vec{r}, \vec{r}\,') \frac{\partial \vec{r}\,'}{\partial a_n} \right) da_n db_n dc_n \\ &= \sum_n \frac{\mu_0 I_n}{4} \int_{-1}^{1}\int_{-1}^{1}\int_{-1}^{1} \nabla G(\vec{r}, \vec{r}\,') \times \frac{\partial \vec{r}\,'}{\partial a_n} da_n db_n dc_n . \end{aligned} \tag{7.21}$$

The divergence is given by

$$\begin{aligned} \nabla \cdot \vec{A}(\vec{r}) &= \sum_n \frac{\mu_0 I_n}{4} \int_{-1}^{1}\int_{-1}^{1}\int_{-1}^{1} \nabla \cdot \left(G(\vec{r}, \vec{r}\,') \frac{\partial \vec{r}\,'}{\partial a_n} \right) da_n db_n dc_n \\ &= \sum_n \frac{\mu_0 I_n}{4} \int_{-1}^{1}\int_{-1}^{1}\int_{-1}^{1} \nabla G(\vec{r}, \vec{r}\,') \cdot \frac{\partial \vec{r}\,'}{\partial a_n} da_n db_n dc_n . \end{aligned} \tag{7.22}$$

The gradient of the divergence is given by

$$\begin{aligned}\nabla(\nabla\cdot\vec{A}(\vec{r})) &= \sum_n \frac{\mu_0 I_n}{4}\int_{-1}^{1}\int_{-1}^{1}\int_{-1}^{1}\nabla\left(\nabla G(\vec{r},\vec{r}\,')\cdot\frac{\partial\vec{r}\,'}{\partial a_n}\right)da_n db_n dc_n \\ &= \sum_n \frac{\mu_0 I_n}{4}\int_{-1}^{1}\int_{-1}^{1}\int_{-1}^{1}\left[\nabla\nabla G(\vec{r},\vec{r}\,')\right]\cdot\frac{\partial\vec{r}\,'}{\partial a_n}da_n db_n dc_n\ .\end{aligned} \tag{7.23}$$

The gradient and Hessian for the Green's function can be inserted in using (7.16) and (7.17), respectively.

The electric field is defined in terms of its potentials as

$$\vec{E}(\vec{r}) = -j\omega\vec{A}(\vec{r}) - \nabla\phi(\vec{r})\ , \tag{7.24}$$

which with the Lorentz gauge,

$$\phi(\vec{r}) = \frac{-1}{j\omega\mu_0\varepsilon_0}(\nabla\cdot\vec{A}(\vec{r}))\ , \tag{7.25}$$

becomes

$$\vec{E}(\vec{r}) = -j\omega\vec{A}(\vec{r}) - j\frac{1}{\omega\mu_0\varepsilon_0}\nabla\left(\nabla\cdot\vec{A}(\vec{r})\right)\ . \tag{7.26}$$

Then, substitute the (7.20) and (7.23) into (7.26) to get

$$\begin{aligned}\vec{E}(\vec{r}) =& -j\omega\sum_n\frac{\mu_0 I_n}{4}\int_{-1}^{1}\int_{-1}^{1}\int_{-1}^{1}G(\vec{r},\vec{r}\,')\frac{\partial\vec{r}\,'}{\partial a_n}da_n db_n dc_n \\ & -j\frac{1}{\omega\mu_0\varepsilon_0}\sum_n\frac{\mu_0 I_n}{4}\int_{-1}^{1}\int_{-1}^{1}\int_{-1}^{1}\left[\nabla\nabla G(\vec{r},\vec{r}\,')\right]\cdot\frac{\partial\vec{r}\,'}{\partial a_n}da_n db_n dc_n \\ =& \sum_n\frac{I_n}{4}\int_{-1}^{1}\int_{-1}^{1}\int_{-1}^{1}\left[-j\omega G(\vec{r},\vec{r}\,')\frac{\partial\vec{r}\,'}{\partial a_n} - \frac{j\omega}{k^2}\left[\nabla\nabla G(\vec{r},\vec{r}\,')\right]\cdot\frac{\partial\vec{r}\,'}{\partial a_n}\right]da_n db_n dc_n\ ,\end{aligned} \tag{7.27}$$

where $k^2 = \omega^2\mu_0\varepsilon_0$ is used to reduce the number of variables in the equation.

The expression for the magnetic field is simply

$$\vec{H}(\vec{r}) = \frac{1}{\mu_0}\left(\nabla\times\vec{A}(\vec{r})\right)\ . \tag{7.28}$$

Thus, the magnetic field is the same as (7.21) with the added $\frac{1}{\mu_0}$ multiplier. So, the final form of the magnetic field is

$$\vec{H}(\vec{r}) = \sum_n \frac{I_n}{4} \int_{-1}^{1}\int_{-1}^{1}\int_{-1}^{1} \nabla G(\vec{r},\vec{r}\,') \times \frac{\partial \vec{r}\,'}{\partial a_n} da_n db_n dc_n \ . \tag{7.29}$$

7.2.3. Far-Field Calculations. The far-field calculations are accomplished using a far-field calculation for the vector magnetic field, which can then be used to directly calculate the far-field approximations for the electric and magnetic fields. The condition for a far-field approximation are $kr \gg 1$. R can be expressed as

$$R = \sqrt{r^2 + r'^2 - 2r\,r'\cos\psi},$$

and then is approximated as

$$R = \begin{cases} r - r'\cos\psi & \text{for phase} \\ r & \text{for magnitude} \end{cases}, \tag{7.30}$$

where

$$\cos\psi = \frac{\vec{r}\cdot\vec{r}\,'}{r\,r'} \ .$$

Then, the far-field approximation to the free-space Green's function is

$$G_{FF}(\vec{r},\vec{r}\,') = \frac{e^{-jk(r-r'\cos\psi)}}{4\pi r} \ . \tag{7.31}$$

Then, substitute (7.31) into (7.20) to get

$$\vec{A}(\vec{r})\Big|_{kr\gg1} \approx \sum_n \frac{\mu_0 I_n}{4} \int_{-1}^{1}\int_{-1}^{1}\int_{-1}^{1} \frac{e^{-jk(r-r'\cos\psi)}}{4\pi r} \frac{\partial \vec{r}\,'}{\partial a_n} da_n db_n dc_n \ . \tag{7.32}$$

The r dependent factor, given by e^{-jkr}/r, can be brought outside the integral and removed from expression for the far-field calculation. So, the final form of the far-field approximation for the vector magnetic potential is

$$\vec{A}(\vec{r})\Big|_{kr\gg1} \approx \sum_n \frac{\mu_0 I_n}{16\pi} \int_{-1}^{1}\int_{-1}^{1}\int_{-1}^{1} e^{jkr'\cos\psi} \frac{\partial \vec{r}\,'}{\partial a_n} da_n db_n dc_n \ . \tag{7.33}$$

The far-field electric field is expressed as

$$\vec{E}(\vec{r})\Big|_{kr\gg 1} \approx -j\omega \left[\vec{A}(\vec{r})\right]_{kr\gg 1} , \tag{7.34}$$

and the far-field magnetic field is

$$\vec{H}(\vec{r})\Big|_{kr\gg 1} \approx \frac{-j\omega}{\eta} \left[\hat{\mathbf{r}} \times \vec{A}(\vec{r})\right]_{kr\gg 1} , \tag{7.35}$$

where η is the intrinsic impedance of the media, which is likely air or vacuum.

7.3. PLANEWAVE REFLECTIONS FROM A CONDUCTING RECTANGLE

A 10 mm by 6 mm conducting plate was illuminated with a plane wave referenced at $z = 0$ with a propagation direction of $\hat{\mathbf{x}}/\sqrt{2} - \hat{\mathbf{z}}/\sqrt{2}$ with $E_x = 1$ V/m. The scattered field from the rectangle was calculated and combined with the incident field to get the total fields. An initial PEEC solution was calculated prior to refining the grid. The solution for the magnetic field on planes above and below the rectangular plate is shown in Figure 7.3. Using the results previously calculated with PEEC, the magnetic field was used to refine the grid. The refinements to the grid are shown in Figure 7.4. A second PEEC calculation using the refined grid produced the fields shown in Figure 7.5. The pattern in Figure 7.5 closely matches the fields calculated by Ansoft HFSS, which are shown in Figure 7.6. The pattern from Figure 7.3 is different from Figure 7.6 due to the lack of cells near the edge of the conductor. It is well known that charge collects on edges and corners more than the center. Thus, it makes sense intuitively that more cells will be needed near the edge, and the grid refining code found the same solution through the local equidistribution algorithm.

The electric field from PEEC and HFSS are shown in Figure 7.7 and Figure 7.8, respectively. Additional, calculations of the magnitudes and phase of the fields along lines above and below the rectangular plate are shown in Figure 7.9 through Figure 7.12.

7.4. SUMMARY AND CONCLUSIONS

A grid refining strategy for PEEC was proposed and implemented on a conducting plate. Field calculations using the PEEC solutions were also shown and used in

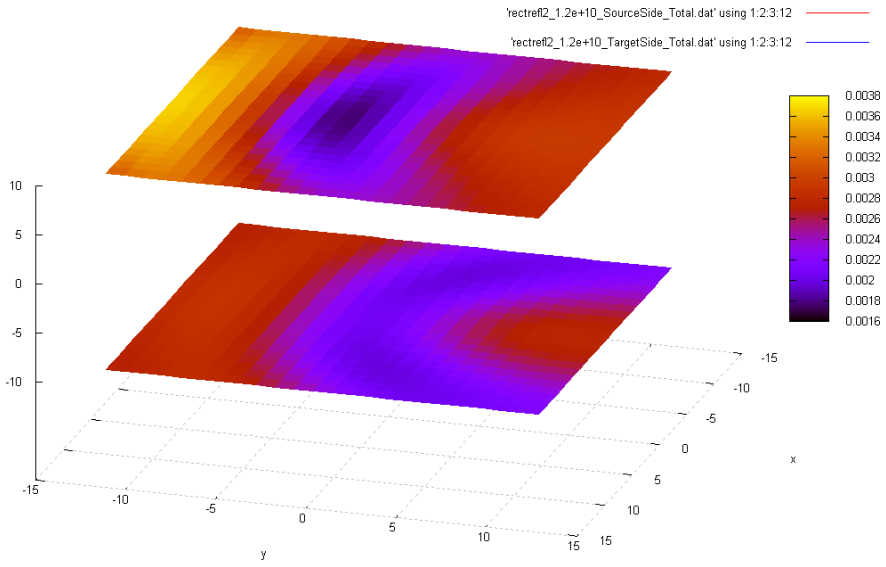

Figure 7.3 The magnetic field calculated 10 mm above and below the rectangular plate before grid refinement

the refining process. The method works well for simple structures like the conducting plate and under incident fields. At the present time the method requires user direction in the form of a few adjustment factors to achieve good grids. In the future, these might be automated and algorithms for checking the shape of cells might be applied to ensure better final grids.

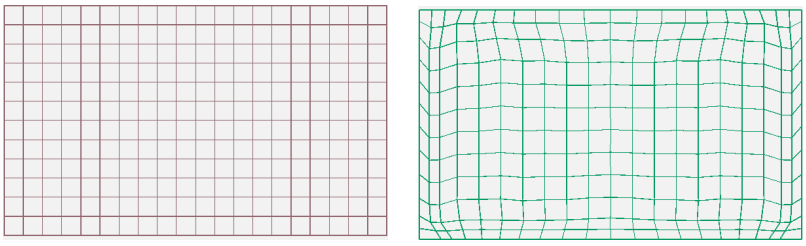

(a) No grid refining (b) After grid refining

Figure 7.4 Reflecting plate grid before and after refining

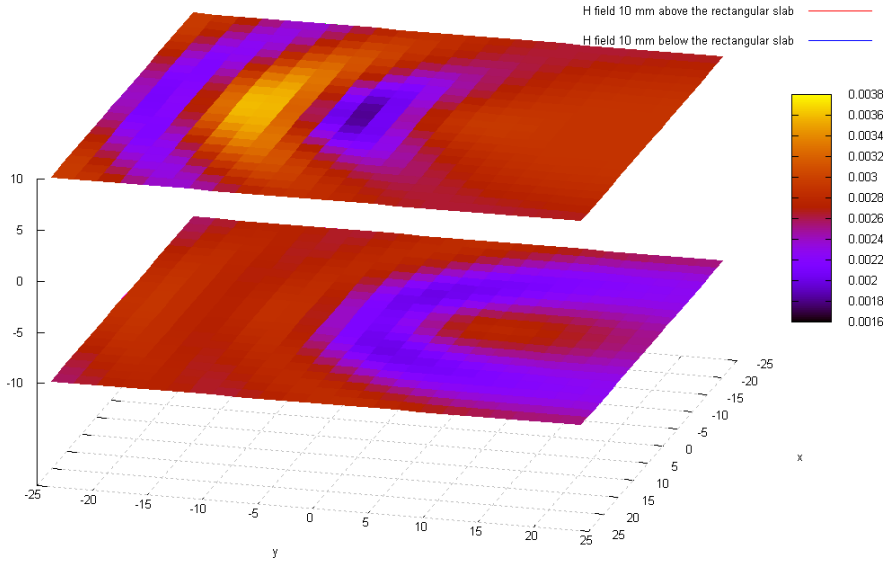

Figure 7.5 The magnetic field calculated 10 mm above and below the rectangular plate after grid refinement based on the magnetic field

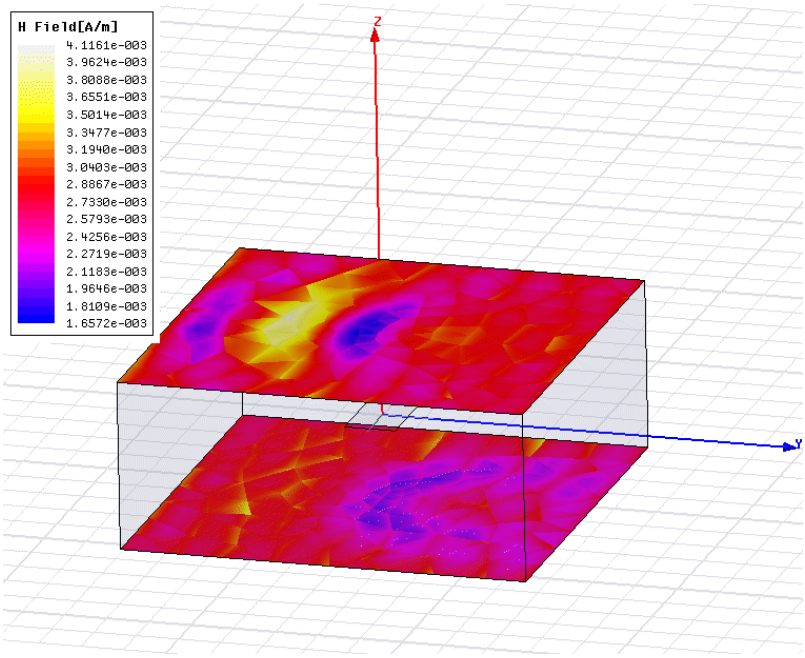

Figure 7.6 The magnetic field calculated 10 mm above and below the rectangular plate using HFSS

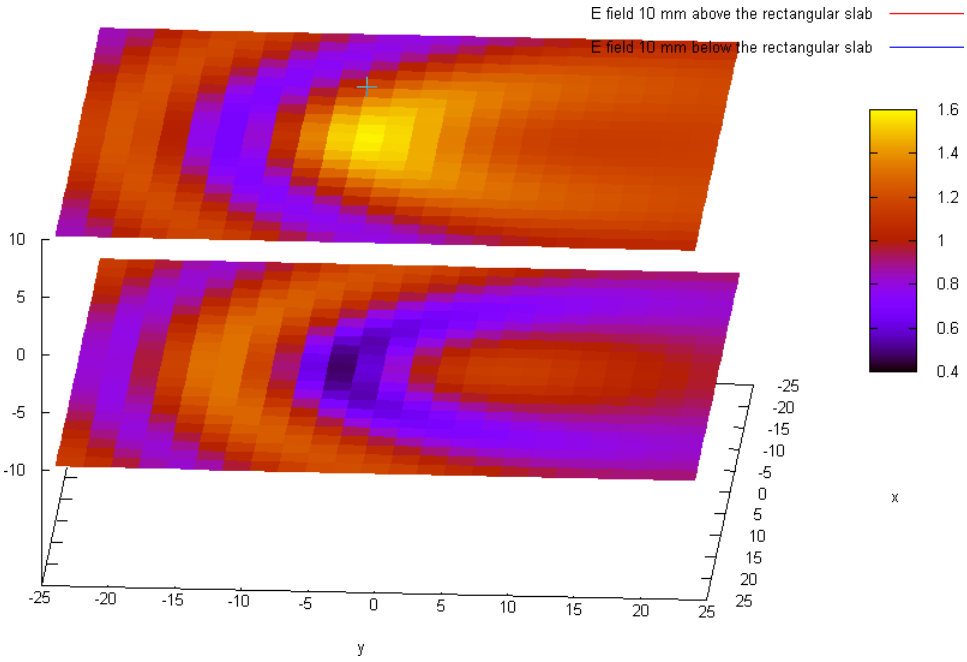

Figure 7.7 The electric field calculated 10 mm above and below the rectangular plate after grid refinement based on the magnetic field

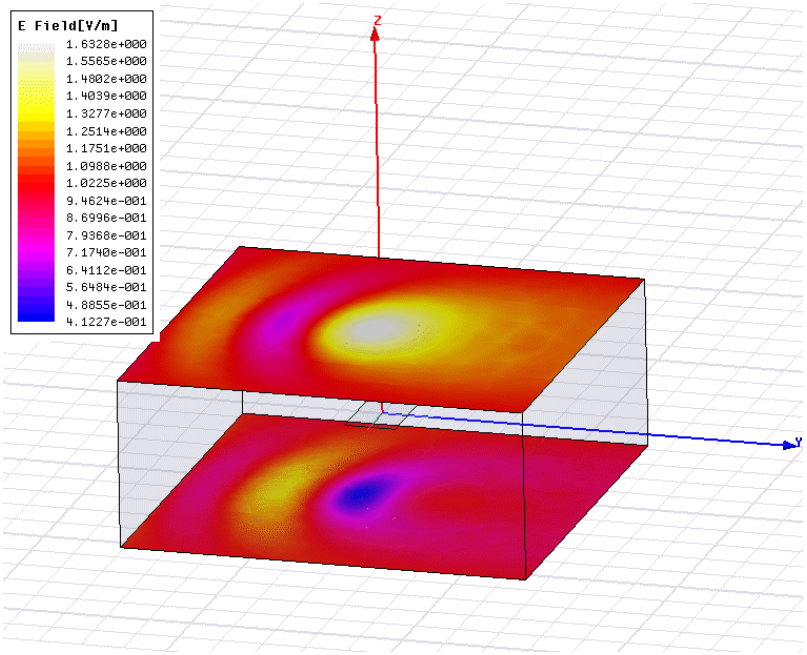

Figure 7.8 The electric field calculated 10 mm above and below the rectangular plate using HFSS

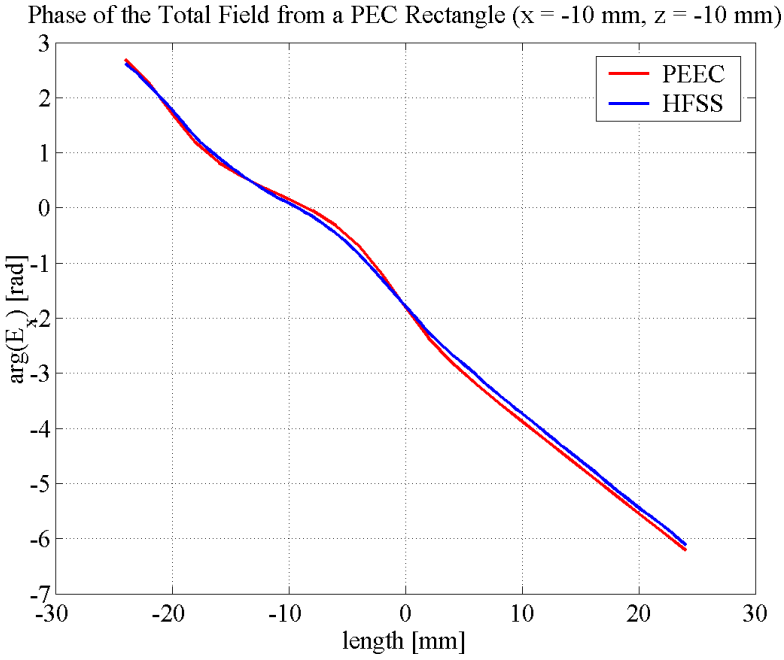

Figure 7.9 The phase of E_x on a y-directed line at x = -10 mm and z = -10 mm

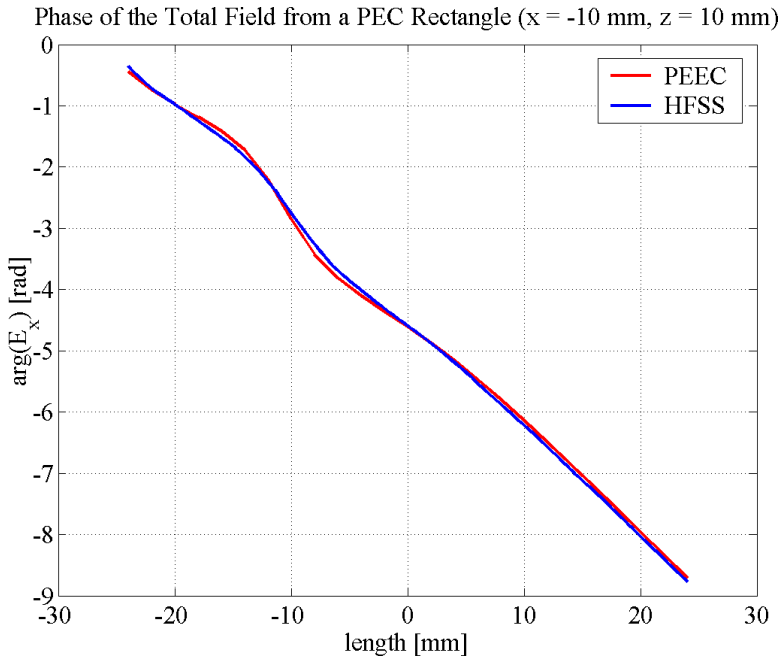

Figure 7.10 The phase of E_x on a y-directed line at x = -10 mm and z = 10 mm

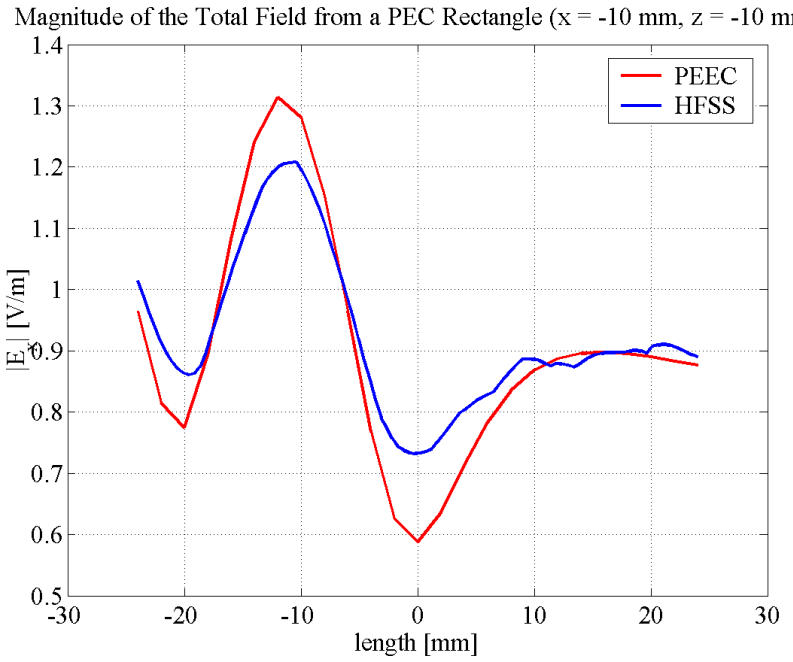

Figure 7.11 $|E_x|$ on a y-directed line at x = -10 mm and z = -10 mm

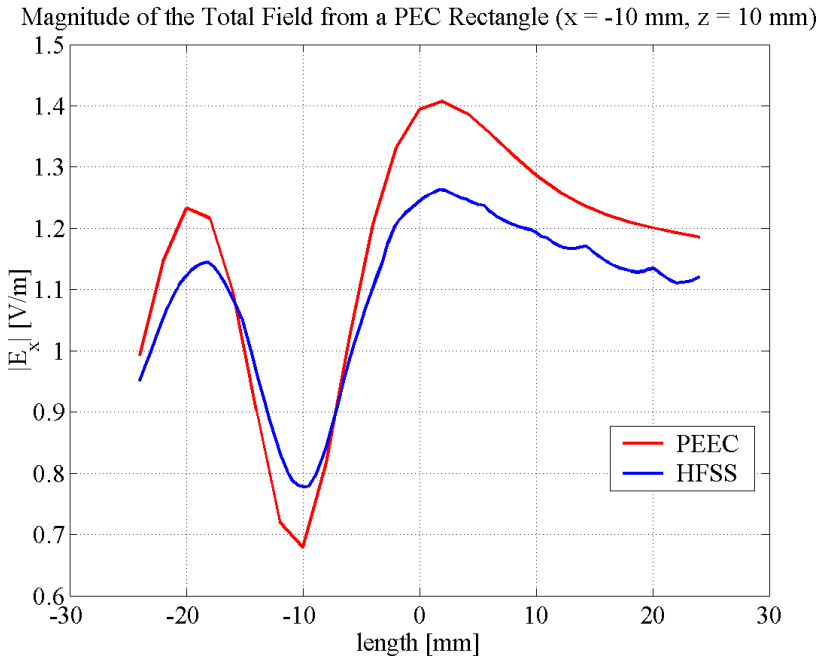

Figure 7.12 $|E_x|$ on a y-directed line at x = -10 mm and z = 10 mm

BIBLIOGRAPHY

[1] G. Antonini and A.E. Ruehli. Fast multipole and multifunction peec methods. *Mobile Computing, IEEE Transactions on*, 2(4):288–298, 2003.

[2] P. Arcioni, M. Bressan, and L. Perregrini. On the evaluation of the double surface integrals arising in the application of the boundary integral method to 3-d problems. *Microwave Theory and Techniques, IEEE Transactions on*, 45(3):436–439, 1997.

[3] Constantine A. Balanis. *Antenna Theory: Analysis and Design*. John Wiley & Sons, Inc., second edition, 1997.

[4] M.A. Cracraft and J.L. Drewniak. Crosstalk analysis for nonparallel transmission lines using peec with a dynamic green's function formulation. In *Electromagnetic Compatibility, 2006. EMC 2006. 2006 IEEE International Symposium on*, volume 1, pages 29–33, 14-18 Aug. 2006.

[5] J.L. Drewniak and P.E. Mayes. Anserlin. a broad-band, low-profile, circularly polarized antenna. *Antennas and Propagation, IEEE Transactions on*, 37(3):281–288, 1989.

[6] J.L. Drewniak and P.E. Mayes. The synthesis of patterns using a series-fed array of annular sector radiating line (anserlin) elements: Low-profile, circularly polarized radiators. *Antennas and Propagation, IEEE Transactions on*, 39(2):184–189, 1991.

[7] J.E. Garrett, A.E. Ruehli, and C.R. Paul. Accuracy and stability improvements of integral equation models using the partial element equivalent circuit (peec) approach. *Antennas and Propagation, IEEE Transactions on*, 46(12):1824–1832, 1998.

[8] H. Heeb and A. Ruehli. Retarded models for pc board interconnects-or how the speed of light affects your spice circuit simulation. In *Computer-Aided Design, 1991. ICCAD-91. Digest of Technical Papers., 1991 IEEE International Conference on*, pages 70–73, 1991.

[9] T. Itoh and R. Mittra. A new method for calculating the capacitance of a circular disk for microwave integrated circuits (short papers). *Microwave Theory and Techniques, IEEE Transactions on*, 21(6):431–432, 1973.

[10] Y. Kami and R. Sato. Crosstalk of finite-length transmission lines in arbitrary directions on the same ground plane. In *Electromagnetic Compatibility, 1992. Symposium Record. IEEE 1992 International Symposium on*, pages 247–250, 1992.

[11] M. Kamon, F. Wang, and J. White. Recent improvements for fast inductance extraction and simulation [packaging]. In *Electrical Performance of Electronic Packaging, 1998. IEEE 7th topical Meeting on*, pages 281–284, 1998.

[12] Patrick M. Knupp and Stanly Steinberg. *The Fundamentals of Grid Generation*. CRC Press, 1993.

[13] S.V. Kochetov and G. Wollenberg. Stable time domain peec solution for pulse interconnection structures. In *Electromagnetic Compatibility, 2005. EMC 2005. 2005 International Symposium on*, volume 3, pages 911–916 Vol. 3, 2005.

[14] Guang-Tsai Lei, R.W. Techentin, and B.K. Gilbert. High-frequency characterization of power/ground-plane structures. *Microwave Theory and Techniques, IEEE Transactions on*, 47(5):562–569, 1999.

[15] Guang-Tsai Lei, R.W. Techentin, P.R. Hayes, D.J. Schwab, and B.K. Gilbert. Wave model solution to the ground/power plane noise problem. *Instrumentation and Measurement, IEEE Transactions on*, 44(2):300–303, 1995.

[16] Y. Lo, D. Solomon, and W. Richards. Theory and experiment on microstrip antennas. *Antennas and Propagation, IEEE Transactions on [legacy, pre - 1988]*, 27(2):137–145, 1979.

[17] S. Luan, F. Xiao, W. Liu, Jun Fan, Y. Kami, J.L. Drewniak, and R.E. DuBroff. Modeling noise coupling from non-parallel pcb trace routing. In *Electromagnetic Compatibility, 2002 IEEE International Symposium on*, volume 1, pages 109–112 vol.1, 2002.

[18] Jingkun Mao, Giulio Antonini, Antonio Orlandi, and James L. Drewniak. Efficient capacitance calculations for peec circuit analysis. In *Proceedings of PIERS*, 2004.

[19] S.E. Melais, T. Weller, and M.J. Wilhelm. A low-profile broadband strip-line balun. In *Antennas and Propagation Society International Symposium, 2005 IEEE*, volume 3B, pages 369–372 vol. 3B, 2005.

[20] J. N. Newman. Distributions of sources and normal dipoles over a quadrilateral panel. *Journal of Engineering Mathematics*, 20(2):113–126, 1986.

[21] David M. Pozar. *Microwave Engineering*. John Wiley & Sons, Inc., 2nd edition, 1998.

[22] P.H. Rao and V.F. Fusco. Polarisation synthesis and beam tilting using a dual port circularly polarised travelling wave antenna array. *Microwaves, Antennas and Propagation, IEE Proceedings* -, 150(5):321–4–, 2003.

[23] P.H. Rao and V.F. Fusco. Ring loading of annular sector radiating line antenna. *Microwaves, Antennas and Propagation, IEE Proceedings* -, 150(5):339–43–, 2003.

[24] A. Ruehli, J. Garrett, and C. Paul. Circuit models for 3d structures with incident fields. In *Electromagnetic Compatibility, 1993. Symposium Record. 1993 IEEE International Symposium on*, pages 28–32, 1993.

[25] A. Ruehli, U. Miekkala, A. Bellen, and H. Heeb. Stable time domain solutions for emc problems using peec circuit models. In *Electromagnetic Compatibility, 1994. Symposium Record. Compatibility in the Loop. IEEE International Symposium on*, pages 371–376, 1994.

[26] A.E. Ruehli, G. Antonini, J. Esch, J. Ekman, A. Mayo, and A. Orlandi. Nonorthogonal peec formulation for time- and frequency-domain em and circuit modeling. *Electromagnetic Compatibility, IEEE Transactions on*, 45(2):167–176, 2003.

[27] A.E. Ruehli, G. Antonini, and A. Orlandi. Extension of the partial element equivalent circuit method to non-rectangular geometries. In *Electromagnetic Compatibility, 1999 IEEE International Symposium on*, volume 2, pages 728–733 vol.2, 1999.

[28] A.E. Ruehli and H. Heeb. Circuit models for three-dimensional geometries including dielectrics. *Microwave Theory and Techniques, IEEE Transactions on*, 40(7):1507–1516, 1992.

[29] A. Weisshaar and V.K. Tripathi. Frequency-dependent transmission characteristics of curved microstrip bends. *Electronics Letters*, 25(17):1138–1139, 1989.

[30] A. Vande Wouwer, Ph. Saucez, and W. E. Schiesser, editors. *Adaptive Method of Lines*. CRC Press, 2001.

[31] Fengchao Xiao, Weikun Liu, and Yoshio Kami. Analysis of crosstalk between finite-length microstrip lines: Fdtd approach and circuit-concept modeling. *Electromagnetic Compatibility, IEEE Transactions on*, 43(4):573–578, 2001.

[32] Minjia Xu and T.H. Hubing. Estimating the power bus impedance of printed circuit boards with embedded capacitance. *Advanced Packaging, IEEE Transactions on [see also Components, Packaging and Manufacturing Technology, Part B: Advanced Packaging, IEEE Transactions on]*, 25(3):424–432, 2002.

[33] Minjia Xu, T.H. Hubing, J. Chen, T.P. Van Doren, J.L. Drewniak, and R.E. DuBroff. Power-bus decoupling with embedded capacitance in printed circuit board design. *Electromagnetic Compatibility, IEEE Transactions on*, 45(1):22–30, Feb. 2003.

[34] Y. Xu and R.G. Bosisio. Calculation of characteristic impedance of curved microstrip lines for mmic and mhmic. *Electronics Letters*, 28(8):775–776, 1992.

[35] Zhen-Yu Zhang, Yong-Xin Guo, L.C. Ong, and M.Y.W. Chia. A new planar marchand balun. In *Microwave Symposium Digest, 2005 IEEE MTT-S International*, pages 4 pp.–, 2005.

VITA

Michael Andrew Cracraft was born 10 July 1978 in Jackson, Missouri. He graduated summa cum laude with his B.S in Electrical Engineering from the University of Missouri–Rolla (UMR) in May 2000. At UMR, Cracraft was a member of the Alpha Iota chapter of Sigma Pi fraternity and was granted membership in both Tau Beta Pi and Eta Kappa Nu. As a graduate student at UMR, he worked in the Electromagnetic Compatibility (EMC) Laboratory of the Electrical and Computer Engineering Department, guided by his advisor Dr. James L. Drewniak and the other EMC faculty. He received the M.S. in Electrical Engineering in May 2002, followed by the Ph.D. in Electrical Engineering in August 2007, both from UMR.